NASA CONTRACTOR REPORT
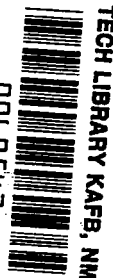
NASA CR-1256

NASA CR-1

NASA CR-1256

PERFORMANCE COMPARISONS OF HIGH MACH NUMBER COMPRESSOR ROTOR BLADING

by J. P. Gostelow, K. W. Krabacher, and L. H. Smith, Jr.

NATIONAL AERONAUTICS AND SPACE ADMINISTRATION • WASHINGTON, D. C. • DECEMBER 1968

NASA CR-1256

PERFORMANCE COMPARISONS OF HIGH MACH NUMBER

COMPRESSOR ROTOR BLADING

By J. P. Gostelow, K. W. Krabacher, and L. H. Smith, Jr.

Distribution of this report is provided in the interest of information exchange. Responsibility for the contents resides in the author or organization that prepared it.

Prepared under Contract No. NAS 3-7617 by
GENERAL ELECTRIC CO.
Lynn, Mass./Cincinnati, Ohio

for Lewis Research Center

NATIONAL AERONAUTICS AND SPACE ADMINISTRATION

FOREWORD

The research described herein, which was conducted by the General Electric Aircraft Engine Technical Division, was performed under NASA Contract NAS3-7617. The work was done under the project management of Mr. James J. Watt, Airbreathing Engines Division, NASA-Lewis Research Center, with Mr. Everett E. Bailey, Fluid System Components Division, NASA-Lewis Research Center, as research consultant.

ABSTRACT

Results of testing of four 1400 foot per second tip speed single
stage compressor rotors are presented. All rotors exceeded design
efficiency and flow at conditions corresponding to design point operation.
Operating range, from peak efficiency to stall, is highest in rotors
designed for a low tip diffusion factor and which have the minimum amount
of supersonic camber.

PERFORMANCE COMPARISONS OF HIGH
MACH NUMBER COMPRESSOR ROTOR BLADING

by

J. P. Gostelow, K. W. Krabacher, and L. H. Smith, Jr.

Aircraft Engine Group

General Electric

SUMMARY

Results of testing of four axial-flow compressor rotors, having a medium aspect ratio and designed for a tip speed of 1400 ft/sec., were evaluated to determine the optimum blade camber line shape. Rotor 1B had a design tip diffusion factor of 0.35 and Rotors 2B, 2E, and 2D were designed for a tip diffusion factor of 0.45. For Rotors 1B and 2B the camber of the supersonic portion of the blade was a minimum consistent with flow choking. Rotor 2D had a double circular arc blade section and Rotor 2E had an intermediate degree of supersonic turning.

All rotors exceeded design efficiency at conditions corresponding to design point operation. Rotor 1B had a considerable range of stall-free operation beyond its design point but the operating range of the Rotors 2, which were designed for higher loading, was much more limited. The effect of camber line shape upon stall margin was considerable, the rotor having least camber in the supersonic portion of the blade had the greatest operating range. When operating with acceptable stall margin for aircraft jet engines, the total-pressure ratio of Rotor 1B was almost as high as those of Rotors 2B and 2E and higher than that of Rotor 2D. At this condition, Rotor 1B had an efficiency of 0.895 whereas Rotors 2B, 2E, and 2D had efficiencies of 0.876, 0.869 and 0.854 respectively.

The design weight flow was exceeded for each of the four rotors as a result of excessive allowance, in the design process, for inlet boundary layer blockage and excessive rotor blade throat area. Radial distributions of flow conditions were in reasonable agreement with the design assumptions.

Two of the rotors were tested with severe radial and circumferential distortions of the inlet flow. Both distortions had a substantial adverse effect on rotor performance.

INTRODUCTION

In the last fifteen years, the direction taken in the development of axial-flow compressors for use in aircraft propulsion engines has been toward increased blade speeds and increased stage loadings. The objective has been to advance in these areas without making a significant sacrifice in efficiency, and at the same time to increase ruggedness, reliability, and resistance to inlet flow distortion. The development of workable titanium alloys has made the use of tip speeds of 1400 feet per second and beyond mechanically practical, and at such speeds blade inlet relative Mach numbers are high enough so that the potential for high losses due to shocks exists. The shock losses may be minimized by minimizing camber in the supersonic or forward portion of the blade. This introduces the possibility of flow separation due to excess surface curvature in the subsonic or rear portion of the blade. It is the objective of the current experimental program to determine the performance of rotors with varying degrees of supersonic camber and to obtain data that will aid in the selection of optimum blade shapes.

In pursuit of these objectives, four different rotors were designed and tested. The design of all four rotors is described in reference 1. One rotor was designed for a tip diffusion factor of 0.35 and three other rotors were more highly loaded, having tip diffusion factors of 0.45.

A new type of blade shape has been employed in which the camber line consists of two circular arcs that are mutually tangent at the point where they join. This point is directly across the flow passage from the leading edge of the adjacent blade that forms the other side of the flow passage. The front arc is identified as the supersonic arc, and the rear arc is identified as the subsonic arc. The term, camber ratio, refers to the ratio of the camber of the supersonic arc to the total camber. The forward and rearward sections of the suction and pressure surfaces were also composed of circular arcs. Blade elements developed in this way are called multiple-circular-arc elements. In this test series the camber ratio at the tip is varied between the minimum that is consistent with choke-free operation and that corresponding to a double circular arc blade section. Performance comparisons for the four rotors that comprise this test series are given in this report and test measurements for the four individual rotors are given in references 2 through 5.

SYMBOLS

The following symbols are used in this report:

A   flow area, in^2

a   distance along chord line to position where maximum perpendicular displacement between camber line and chord line occurs, in

c blade chord length, in

D diffusion factor, $D = 1 - \dfrac{V_2'}{V_1'} + \dfrac{r_2 V_{\theta 2} - r_1 V_{\theta 1}}{2 \bar{r} \sigma V_1'}$

i incidence angle, difference between air angle and camber line angle at leading edge in cascade projection, deg

M Mach number

P total or stagnation pressure, psia

P_{max} average total pressure in undistorted region, psia

P_{min} average total pressure in distorted region, psia

r radius, in

$\bar{r}$ mean radius, average of streamline leading-edge and trailing-edge radii, in

T total or stagnation temperature, °R

V air velocity, ft/sec

w weight flow, lb/sec

Z displacement along compressor axis, in

β air angle, angle whose tangent is the ratio of tangential to axial velocity, deg

δ ratio: $\dfrac{\text{total pressure}}{\text{standard pressure}}, \dfrac{\text{psia}}{14.696\ \text{psia}}$

δ° deviation angle, difference between air angle and camber line angle at trailing edge in cascade projection, deg

θ ratio: $\dfrac{\text{total temperature}}{\text{standard temperature}}, \dfrac{°R}{518.688°R}$

η efficiency

$\vec{i}_\kappa$ unit vector in direction of intersection of axisymmetric stream surface and blade mean surface

κ angle between cylindrical projection of $\vec{i}_\kappa$ and axial direction, deg

σ solidity, ratio of chord to spacing

φ camber angle, difference between angles, in cascade projection, of tangents to camber line at extremes of camber line arc, deg

ψ stream function; $\psi_h = 0$, $\psi_c = 1$

$\bar{\omega}$ total-pressure-loss coefficient

Subscripts:

ad	adiabatic
an	annulus value
avg	arithmetic average at any plane
in	inlet average conditions
j	immersion number
ss	supersonic or front portion of blade element
stall	at the point of stall inception
t	tip at rotor leading edge plane
thr	location in passage between adjacent blades where area bounded by adjacent blades and adjacent axisymmetric stream surfaces is minimum
z	with respect to axial displacement
θ	with·respect to meridional displacement
1	leading edge
2	trailing edge

0.05, 0.86, 0.95, 1.51, 1.57, 2.0 instrumentation plane designations (fig. 3)

Superscripts:

*	critical·flow condition
'	relative to rotor

DESCRIPTION OF TEST ROTORS

Four rotors have been designed and tested in this investigation. The design of all four rotors is given in reference 1 and test results from all four rotors are presented in references 2, 3, 4, and 5. All four rotors

were designed for a corrected weight flow per unit frontal area of 29.66 lbs/sec per square foot. With the selected rotor tip diameter of 36.5 inches and the hub-tip radius ratio of 0.50, the design corrected weight flow is 215.49 lbs/sec. A rotor tip solidity of 1.3, zero inlet swirl, a rotor tip speed of 1400 ft/sec, and a tip axial velocity ratio of 0.91 were selected. A tip diffusion factor of 0.35 was chosen for Rotor 1B, and a value of 0.45 was chosen for Rotors 2B, 2E, and 2D. Based on the above design parameters the change in angular momentum across the rotor at the rotor tip was calculated. This change in angular momentum, with a suitable rotor total-pressure-loss coefficient, derived from the NASA method of references 6 and 7, resulted in a design rotor total-pressure ratio of 1.60 for Rotor 1B, and 1.76 for Rotors 2B, 2E and 2D. The design total-pressure ratio was held constant radially in all four rotors. Because use of the loss correlation resulted in radially varying losses, a radial variation of the change in angular momentum was used in the design vector diagram calculations.

Double-circular-arc blade sections were used in the cascade projection* along the radial height of the blade between the hub and a point approximately 60 percent of the span away from the hub. Multiple-circular-arc sections were used in the remaining portion of the blade. The tip blade elements of Rotors 1B and 2B were selected to have the minimum amount of camber in the supersonic portion of the blade that was consistent with flow choking limitations. In the case of Rotor 2D the blade had a double-circular-arc section along the entire blade span. Rotor 2E had a blade shape which was intermediate between the two extremes. Blade element design data in the cascade projection are given for the four rotors in tables 1 through 4. In figure 1 a close-up of the tip elements of one blade from each of the four rotors is given. The different camber line shapes of each blade can be clearly seen in this photograph.

In order to assess the quality of the blading after manufacture, the blading was inspected by means of contour layouts at several cylindrical sections. The average blade profiles derived in this way were then compared with design intent. In all cases it was judged that the blading was adequate to achieve design intent.

The average running tip clearance, at 100% speed, was in the range between 0.037 inch and 0.043 inch for all four rotors.

Performance tests were made in General Electric's House Compressor Facility, at Lynn, Massachusetts. A diagram of the test arrangement is

---

*As described in reference 1, the cascade projection is obtained by viewing the intersection of a blade and an axisymmetric stream surface in the radial direction. The justification for the use of this projection is given in reference 8.

given in figure 2 and the facility is described in reference 2. In the meridional view of figure 3, some instrumentation locations are given and the hub and casing contours are indicated. As explained in reference 1, a common casing was used for all four rotors. The difference in hub contour between Rotor 1 and Rotors 2 resulted in different radii for all of the instrumentation except the inlet pitot-static and casing boundary layer rakes. The circumferential layout of instrumentation is shown in figure 4.

The detailed instrumentation and general procedure which were used in the testing of each rotor have been described in the appropriate performance reports (refs. 2, 3, 4, and 5).

Table 1: Rotor 1B Design Data For Blade Element Immersions At Leading And Trailing Edges

j	r_1	β_1'	i	κ_1'
1	17.310	63.458	3.748	59.61
2	15.622	60.806	4.796	56.01
3	13.916	58.406	5.846	52.56
4	12.182	55.659	5.949	49.71
5	10.257	53.393	6.783	47.11

j	r_2	β_2'	δ°	κ_2'
1	17.137	57.896	3.476	54.47
2	15.595	56.077	3.397	50.68
3	14.034	47.497	3.707	43.79
4	12.456	37.542	5.392	32.15
5	10.895	22.770	8.480	14.29

j	$\dfrac{a}{c_t}$	σ	D	$\dfrac{V_{z2}}{V_{z1}}$
1	0.696	1.369	0.388	0.846
2	0.616	1.508	0.432	0.812
3	0.500	1.684	0.475	0.826
4	0.500	1.906	0.510	0.864
	0.500	2.217	0.481	1.015

Table 2: Rotor 2B Design Data For Blade Element Immersions At Leading And Trailing Edges

j	r_1	β_1'	i	κ_1'
1	17.392	62.625	3.985	58.64
2	15.759	60.159	4.829	55.33
3	14.180	57.957	5.707	52.25
4	12.456	55.725	6.015	49.71
5	10.494	56.874	6.274	50.60

j	r_2	β_2'	$\delta°$	κ_2'
1	17.201	54.224	5.864	48.36
2	15.768	49.376	5.086	44.29
3	14.354	41.761	5.591	36.17
4	12.921	30.561	7.111	23.45
5	11.516	17.164	11.384	5.78

j	$\dfrac{a}{c_t}$	σ	D	$\dfrac{V_{z2}}{V_{z1}}$
1	0.685	1.363	0.471	0.833
2	0.593	1.494	0.513	0.811
3	0.500	1.650	0.552	0.830
4	0.500	1.849	0.554	0.914
5	0.500	2.136	0.448	1.259

Table 3: Rotor 2E Design Data For Blade Element Immersions At Leading And Trailing Edges

j	r_1	β_1'	i	κ_1'
1	17.392	62.625	3.725	58.90
2	15.759	60.159	4.699	55.46
3	14.180	57.957	5.707	52.25
4	12.456	55.725	6.015	49.71
5	10.494	56.874	6.274	50.60

j	r_2	β_2'	$\delta°$	κ_2'
1	17.201	54.224	4.784	49.44
2	15.768	49.376	4.646	44.73
3	14.354	41.761	5.591	36.17
4	12.921	30.561	7.111	23.45
5	11.516	17.164	11.384	5.78

j	$\dfrac{a}{c_t}$	σ	D	$\dfrac{V_{z2}}{V_{z1}}$
1	0.621	1.363	0.471	0.833
2	0.562	1.494	0.513	0.811
3	0.500	1.650	0.552	0.830
4	0.500	1.849	0.554	0.914
5	0.500	2.136	0.448	1.259

Table 4: **Rotor 2D Design Data For Blade Element Immersions At Leading And Trailing Edges**

j	r_1	β_1'	i	κ_1'
1	17.392	62.625	3.845	58.78
2	15.759	60.159	4.769	55.39
3	14.180	57.957	5.707	52.25
4	12.456	55.725	6.015	49.71
5	10.494	56.874	6.274	50.60

j	r_2	β_2'	δ°	κ_2'
1	17.201	54.224	4.044	50.18
2	15.768	49.376	4.346	45.03
3	14.354	41.761	5.591	36.17
4	12.921	30.561	7.111	23.45
5	11.516	17.164	11.384	5.78

j	$\dfrac{a}{c_t}$	σ	D	$\dfrac{V_{z2}}{V_{z1}}$
1	0.500	1.363	0.471	0.833
2	0.500	1.494	0.513	0.811
3	0.500	1.650	0.552	0.830
4	0.500	1.849	0.554	0.914
5	0.500	2.136	0.448	1.259

COMPARISONS OF OVERALL PERFORMANCE

The performance maps obtained from testing each of the four rotors with an undistorted inlet flow are presented in figures 5 (a) through 5 (d). In this portion of the report the overall performance of each rotor is discussed both in relation to its design point and with respect to the performances of the other rotors. Certain conclusions are drawn with regard to the effects of blade loading and tip camber line shape. Finally the performance with distorted inlet flow is discussed.

Comparisons of Performance with Design Intent

Weight Flow Comparisons. As can be seen in figures 5 (a) through 5 (d), all of the rotors exceeded the design flow at design speed. The percentages by which this occurred are given in table 5.

Table 5: Percentages by Which Achieved Weight Flow Exceeded Design Weight Flow at Design Speed

	At design pressure ratio	At maximum flow
Rotor 1B	2.1	3.0
2B	3.7	4.0
2E	4.6	5.2
2D	4.7	5.0

Since these rotors operate transonically, passage areas can be expected to play a large role in the establishment of the weight flow. Therefore, table 6 has been prepared to provide an assessment of the various allowances that affect passage throat area.

Table 6: Throat Area Allowances, Expressed as Percent of Design Capture Area

Rotor	Design				Test, at design pressure ratio			
	1B	2B	2E	2D	1B	2B	2E	2D
Allowance for inlet annulus-wall boundary layers	2.0	2.0	2.0	2.0	1.1	1.1	1.1	1.1
Allowance for part-span shroud	2.0	2.0	2.0	2.0	1.4	1.2	1.2	1.2
Allowance for normal-shock relative-total pressure loss	1.2	1.6	1.6	1.6	1.2	1.6	1.6	1.6
Allowance for all other effects	3.9	7.7	9.0	9.9	3.3	5.7	6.1	6.9
Total area allowance	9.1	13.3	14.6	15.5	7.0	9.6	10.0	10.8

Part of the flow excess shown in table 5 for each rotor can be directly related to the annulus-wall boundary layer blockage assumption. An effec-tive-area coefficient of 0.98 was used as a design value at rotor inlet. Total-pressure measurements taken with the boundary layer rake during run-ning of Rotor 1B at design speed have indicated that the casing boundary layer displacement thickness was 0.06 inch. If it is assumed that the hub boundary layer displacement thickness is 0.03 inch, which is plausible, the inlet annulus-wall boundary layers actually only accounted for an area re-duction of 1.1%. This has been indicated in the first row of table 6. Also, 2% area allowance had been made for the part-span shrouds; however, measure-ments of shroud thickness after fabrication indicated that somewhat less area than that was actually blocked, as indicated in the second row of table 6.

The derivation of allowances for normal-shock loss and for all other effects is illustrated for Rotor 1B in figure 6. The area allowance for the relative total-pressure loss due to a normal shock at the upstream Mach num-ber was not affected by the slight differences between design and test Mach numbers; thus the design and test parts, in the third row of table 6, are identical. The design allowance for all other effects was not specified as such in the design process but resulted from the design specifications of incidence, deviation, thickness and camber ratio. The resulting area allow-ance for all other effects is identified in figure 6. Allowances given on the design side of the table are consistent with the difference between de-sign values and the theoretical throat area curve, in figure 6, averaged over the annulus.

The values of "total area allowance" on the test side of table 6 differ from those on the design side by the flow differences at design pressure ratio given in table 5*. The numbers in the "allowance for all other effects" row on the test side of table 6 are those needed to obtain the totals in the final row. As explained in Appendix C of reference 1, the physical phenomena that require this allowance are:

1. build-up of blade boundary layer,

2. build-up of annulus wall boundary layers from the leading edge to the blade throat,

3. shock losses in excess of those associated with one normal shock at the inlet relative Mach number, and

4. lack of uniform flow in the free stream at the blade throat.

---

*It is permissible here to relate percentage flow changes with percentage area changes in the rotating frame of reference because no inlet swirl was present and, therefore, the radial distributions of relative total pressure and relative total temperature were the same for both design and test.

From the data which have been presented it appears that the excess weight flow obtained in the testing of each rotor was related to the total throat passage area allowance for that rotor. It is likely that too much throat area was provided for each of these rotors. In any subsequent design it would be advisable to specify throat area as a design parameter and to shape the blade elements accordingly.

Operating Range Comparisons. As discussed in the test reports, the stall line for each rotor was obtained by observation of the discharge valve setting at the stall point and extrapolation of the pressure ratio and weight flow characteristics to the stall setting.

From the Rotor 1B performance map (fig. 5(a)), it is evident that, at 100% speed, the rotor could be throttled considerably beyond the region of the design point before the onset of rotating stall. The Rotors 2 however, (figs. 5(b), 5(c), and 5(d)), do not possess such a wide range of stall-free operation as Rotor 1B; this can also be seen in figure 7 which is a composite plot for the design speed performance of each rotor. The stall lines of Rotors 2B, 2E, and 2D are too close to their design point for most aircraft applications. As a result of this disparity between the operation of Rotor 1 and of the Rotors 2, it is not adequate to mutually compare the performance levels on the basis of design point operation. It is therefore desirable to introduce a quantitative criterion for stall margin for use in any comparative appraisal of the rotors. One simple and useful stall margin parameter which has been frequently used is the percentage by which the weight flow divided by pressure ratio, at any operating point, exceeds that quantity at the stall point. The formulation of this is as follows:

$$\% \text{ stall margin} = 100 \left[\frac{\left(\dfrac{w}{P_{1.57}/P_{0.05}}\right)}{\left(\dfrac{w}{P_{1.57}/P_{0.05}}\right)_{stall}} - 1 \right] \qquad (1)$$

at constant speed. Table 7 gives the stall margin, along a constant-speed line that passes through the design pressure ratio and weight flow, for each of the four rotors:

Table 7: Stall Margin Obtained for Operation at the Design Point

Rotor	1B	2B	2E	2D
% stall margin	21.5	11.0	6.8	5.1

This table clearly shows that stall margin is lost when higher design loadings are used, at least for the range of variables and design types used in this investigation. In going from Rotor 1B, which has a design total-pressure ratio of 1.6, to the comparable rotor having a design total-pressure ratio of 1.76 (Rotor 2B), the available stall margin for operation at their respective design points falls by 10.5%. Furthermore, when the Rotors 2 are mutually

compared, it is evident that the use of blading having large amounts of supersonic camber entails a further drop in stall margin; this drop is such that in the case of a blade composed entirely of double-circular-arc blade elements (Rotor 2D), the stall margin has fallen by 5.9% from that of Rotor 2B.

No limitation on normal rotor operation was observed for any of the rotors at low back pressures down to the point of wide-open throttle valve setting.

Efficiency Comparisons. Although it is most meaningful to mutually compare the performances of the different rotors at the same stall margin, this will be deferred until later in this section, and the quality of agreement of rotor performance with design intent will be discussed first. Accordingly, the method of relating rotor performance to the design point will now be defined, and the design assumptions will be examined.

The most accurate method of assessing how well a rotor achieves its design objectives would be to directly relate the design intent to the performance of the rotor when operating at the design point. In general, however, the 100%-speed line will not pass exactly through the design point. A significant way of comparing test conditions with design point conditions is to pass a line of constant throttle setting through the design point (fig. 7) and to relate to design intent the performance at the junction of the constant throttle line with the speed line.

When assessed in this manner, Rotor 1B has an efficiency of 0.895 which is 0.037 higher than the design value of 0.858. Rotors 2B and 2E attained equal efficiencies of 0.884 for conditions corresponding to the design point for the Rotors 2. The Rotors 2 were all designed for an efficiency of 0.837; Rotors 2B and 2E therefore possess a 0.047 advantage over the design values. The efficiency of Rotor 2D, at 0.864, is only 0.027 better than design. Although the efficiency of each of these rotors, for conditions corresponding to the design point, is considerably higher than the design value, it should be remembered that the Rotors 2 have insufficient stall margin at these conditions.

The overall rotor adiabatic efficiencies obtained from fixed instrumentation readings at design speed, for all four rotors, are plotted, as a function of percent stall margin, in figure 8. The curves which are presented were faired by attaching equal importance to all valid fixed instrumentation readings. This plot illustrates the large difference between Rotor 1B and the Rotors 2 at design speed. Rotor 1B could obviously be throttled a considerable amount beyond the peak efficiency point before the occurrence of stall. In fact, its peak efficiency occurs at a stall margin of 18%. The peak efficiency of each of the Rotors 2 occurs in the region between five and eight percent stall margin. It is evident that, for values of stall margin above about 12%, Rotor 2B has a slight advantage of between one-half and one efficiency point over Rotor 2E, which likewise has a one to two point advantage over Rotor 2D.

Design Speed Performance Summary. It is useful at this stage in the report to summarize the results which are obtained when the performance of each rotor is compared in the two different ways described in the two preceding sections. The major performance results for each rotor are presented in table 8 below:

Table 8: Design Speed Performance Summary

Rotor	Tip camber ratio	Design values		
		$\dfrac{P_{1.57}}{P_{0.05}}$	$\dfrac{w\sqrt{\theta}}{\delta}$	η_{ad}
1B	0	1.60	215.49	0.858
2B	0	1.76	215.49	0.837
2E	0.35	1.76	215.49	0.837
2D	0.65	1.76	215.49	0.837

Rotor	Tip camber ratio	Performance on constant throttle line through design point				Performance at operating point (15% stall margin)		
		$\dfrac{P_{1.57}}{P_{0.05}}$	$\dfrac{w\sqrt{\theta}}{\delta}$	η_{ad}	% stall margin	$\dfrac{P_{1.57}}{P_{0.05}}$	$\dfrac{w\sqrt{\theta}}{\delta}$	η_{ad}
1B	0	1.638	219.2	0.895	20.3	1.688	216.0	0.895
2B	0	1.836	220.6	0.884	9.1	1.763	223.5	0.876
2E	0.35	1.845	221.5	0.884	4.6	1.711	225.9	0.869
2D	0.65	1.858	221.0	0.864	1.5	1.677	226.0	0.854

The first group of data above gives design values of pressure ratio, weight flow and efficiency for each rotor. Following these are the measured values of these parameters obtained at the intersection of the 100% speed line with a line of constant throttle setting through the design point. The stall margin, based on the definition of equation (1), for operation of each rotor at this point, is also listed. The final group of data presents the levels of pressure ratio, weight flow and efficiency that the four rotors obtained during operation with 15% stall margin. Since these values represent the highest levels of total-pressure ratio and efficiency for operation of Rotors 2B, 2E, and 2D with an amount of stall margin that is judged to be acceptable for aircraft engine operation, these are the values that were quoted in the test reports for the Rotors 2 (refs. 3, 4, and 5).

Evaluation of Influence of Design Loading Level
and Blade Tip Camber Ratio

Effect of Design Loading Level. The efficiency penalty which is associated with designing rotors of the general type considered here for higher loadings (rotor tip diffusion factor of 0.45 compared with 0.35) is not severe if the rotors are evaluated at conditions corresponding to design point operation. The efficiency of Rotor 1B at design speed on a constant throttle line through its design point is 0.011 higher than the value for Rotor 2B corresponding to its design point. However, if the rotors are compared on the basis of 15% stall margin, the efficiency penalty associated with the extra loading rises to 0.019. Furthermore, the rotor which was designed for the higher tip loading (Rotor 2B) emerges with only a small loading advantage, having a total-pressure ratio of 1.763 as compared with the value 1.688 that was achieved by Rotor 1B. The other two rotors that were designed for the higher tip loading do not even have this advantage; in fact, Rotor 2D does not support as high a total-pressure ratio as Rotor 1B.

Another meaningful way to assess the loading achievements of the rotors is to compare the stall lines on the total-pressure ratio versus weight flow performance maps. This is of interest because in many compressor applications the operating line depends primarily on these variables, being largely independent of the speed. On this basis the loading attained by Rotor 1B is essentially equal to that attained by Rotor 2B, as can be seen by comparing the stall lines in figure 9.

As a result of these tests it therefore seems that only a small efficiency penalty, for operation at conditions corresponding to the design point, is associated with designing for a tip diffusion factor of 0.45 rather than for the more conservative value of 0.35. However, a much more severe penalty in stall margin is associated with such an increase in design loading. Accordingly, the most important consequence of designing rotors to be more highly loaded is that their range of stall-free operation may be sufficiently limited as to minimize any benefit which might be expected in the form of improved total-pressure ratio capability.

Effect of Tip Camber Ratio. Rotors 2B, 2E and 2D will now be mutually compared to ascertain the effect of tip camber ratio.

The stall lines shown in figure 9 clearly indicate the advantage of small supersonic camber (Rotors 1B and 2B) from the point of view of pressure ratio potential.

In figure 10 the efficiency of each of the three Rotors 2 is assessed on the basis of a 15% stall margin at design speed. Rotor 2B, which has the minimum supersonic camber consistent with flow choking limitations, is seen to have a 0.022 efficiency advantage over Rotor 2D, which has a double-circular-arc tip section.

The other curve presented in figure 10 uses the peak values of efficiency at design speed. By comparing these peak efficiencies Rotor 2B emerges with a 0.010 efficiency advantage over Rotor 2D.

The values of efficiency plotted in figure 10, both for operation with 15% stall margin and also at peak efficiency conditions, were not obtained directly from actual fixed instrumentation readings but are, rather, faired values. The validity of this fairing can be examined by referring to figure 8.

As a result of the above comparison it is clear that when the performance of the Rotors 2 is reviewed at conditions corresponding to design pressure ratio and weight flow, the rotor having the minimum amount of supersonic camber has a substantial advantage in available stall margin. The same rotor also has an appreciable efficiency advantage if all three rotors are operated at the same level of stall margin.

Performance at Other Speeds. To provide a reference for comparing, on a consistent basis, the data which were recorded at rotational speeds other than design, a constant throttle line has been drawn for each of the four rotors through that point on the 100% corrected-speed line which gave 15% stall margin (figs. 5 (a) through 5 (d)). Efficiencies obtained along these reference lines are plotted as a function of percent corrected speed in figure 11 (a). The symbols indicate faired values of efficiency and do not correspond to any particular fixed instrumentation readings.

In general, the highest efficiencies are to be seen at 70% corrected speed. The level of efficiency recorded at 50% speed is generally slightly lower; this is probably a result of the higher rotor blade incidences at the lowest speed. At rotational speeds higher than 70% the efficiency usually falls off quite steeply, presumably as a result of the progressive strengthening of shocks and the increase of their associated losses.

It is of value to compare the performance of Rotors 1B and 2B on the basis described above and to assess the effects of design tip loading at off-design speeds. Rotor 1B, which was designed for the lower tip diffusion factor, has a lower efficiency than Rotor 2B at speeds below 90% (figure 11(a)). At design speed and higher speeds Rotor 1B has a definite efficiency advantage. This apparently is a consequence of the fact that at high Mach number, deflection of the flow is accompanied by high losses, so the advantage is with Rotor 1B because of its lower camber. At the lower speeds, however, the increased work input of Rotor 2B for a given relative velocity leads to its higher efficiencies.

When the Rotors 2 are mutually compared, Rotor 2D is seen to perform best in the range of rotational speeds below 85 percent of design speed for which the inlet relative Mach numbers are less than about 1.2 at the blade tip. At the higher speeds, where strong shock waves are encountered, the large amount of supersonic turning implicit in the double-circular-arc

blade tip section causes the efficiency to fall rapidly. The performances of Rotors 2E and 2B are rather similar. Although Rotor 2B has a slightly higher efficiency than Rotor 2E at design speed, this does not represent a consistent trend. In general, at 15% stall margin, there is little difference between the efficiencies of Rotors 2E and 2B at any speed.

Figure 11 (b) gives the faired values of peak efficiency for each rotor at the various speeds. The efficiency trends obtained by presenting peak values are not greatly different from those which were obtained by presenting values along a constant throttle line having 15% stall margin at design speed.

As an example of off-design performance the composite plot in figure 12 gives the 70% speed lines of each rotor. The smaller camber of Rotor 1B causes it to produce less pressure rise than the others at any given flow, but, as pointed out previously, its stall line is essentially identical with those of the other rotors. The operating range of all rotors (1 and 2) at 70% speed is nearly identical.

Performance with Stall Present. Throttling of all four rotors, during running with a uniform inlet flow, was limited by rotating stall at all five rotational speeds. As described in the test reports (refs. 2, 3, 4 and 5) the rotors were stalled twice at each speed.

For the first stall at each speed, the three hot-wire anemometers were immersed to three different radial positions (usually the 10%, 50% and 70% immersions) in order to obtain stall data along the blade span. Data obtained in this way were used to provide information concerning the radial extent of the stall cells. Stall occurred abruptly along the blade span and evidence of regular and periodic rotating stall cells was recorded at each of the three immersions, although at the 70% immersion the stall signal was usually weaker.

For the second stall at each speed, the three hot-wire anemometers were all located at the 10% immersion. Sufficient information was obtained from the output traces for the speed and number of the rotating stall cells to be deduced. Independent checks of these quantities were obtained from rotor strain gauge information, as described in reference 2. These data are summarized in table 9. The numbers and propagation speeds of the stall cells were averaged for the four rotors and the results are presented in figures 13(a) and 13(b). Although considerable scatter is present, the fairing of a straight line through the points in each case seems justifiable. The number of stall cells (which, for any one rotor speed at any instant in time, must be an integral number) is seen to fall as speed increases. Operation with only one stall cell is therefore most likely at the higher rotational speeds whereas, at the lower speeds, operation with two or three stall cells is more likely. Although no large variations in propagation speed are apparent, in general the ratio of propagational

speed to rotor speed decreases with increasing rotor speed.

Table 9. - Tabulation of Stall Data for All Rotors

Rotor	Rotor speed, percent design	Number of stall cells	Stall cell speed Rotor speed	Radial extent of stall cell
1B	50	2	.60	Full span
	70	2	.62	Full span
	90	3	.62	Full span
	100	2	.62	Full span
	110	1	.58	Full span
2E	50	3	.68	Full span
	70	2	.64	Full span
	90	1	.61	Full span
	100	1	.66	Uncertain
	110	1	.61	Uncertain
2D	50	2	.68	Full span
	70	3	.69	Full span
	90	1	.59	Full span
	100	1	.61	Full span
	110	1	.61	Full span
2B	50	3	.64	Full span
	70	2	.63	Full span
	90	1	.62	Full span
	100	2	.62	Full span
	110	1	.61	Uncertain

When stress conditions permitted, the second stall at each speed was sustained for sufficient time for a fixed-instrumentation (green) reading to be recorded. These overall performance measurements, recorded while the rotor was operating with stall present, appear as solid symbols in figure 5. The flow was quite unsteady for these readings, and their accuracy is open to question; however, a significant drop in performance was indicated.

During the testing of Rotor 2B, an effort was made to measure the extent of the hysteresis loop which is often present when stall is encountered. With all the hot wires located at the 10% immersion, the throttle valve was opened very slowly until stall was cleared. This is in contrast to the usual procedure, which had been to clear stall by opening the throttle valve abruptly. During this period certain pressures were

sensed and were processed by an analog computer which calculated the instantaneous values of corrected weight flow and total-pressure ratio. These parameters were supplied to an X-Y plotter which produced traces that have been duplicated in figure 14. As a result of time lag difficulties and the previously-mentioned unsteadiness in the airflow, these plots should only be regarded as qualitative illustrations and numerical scales have not been supplied. It is, however, quite clear that a sizeable hysteresis loop is present at the 90%, 100% and 110% corrected speeds. The discontinuities in the traces are a result of changes in the number of stall cells, as was determined by oscilloscope readout from the strain gauges and hot wires. The number of stall cells tabulated corresponded, in all cases, to the mode of stalled operation which was encountered first. Traces were also taken at the 50% and 70% corrected speeds but the flow unsteadiness, which compounded the usual difficulties of measuring accurate weight flows at these speeds, prevented the recording of reliable results.

Performance with Distorted Inlet Flow. Rotors 1B and 2B were each tested with both radial and circumferential flow distortions. The distortion screens were, in all cases, located at plane 0.1, as shown in figure 3. The radial distortion screen covered the outer 40% of the annulus area and the circumferential distortion screen covered a 90° arc. Both screens employed 0.016" diameter wires spaced at 0.050" and were supported on a 3/4" mesh screen having wires of 0.092" diameter.

Analysis of data from testing of both rotors, and with each type of distortion present, indicate that, for the solidity of the support screen and at the appropriate Mach number for 100% corrected speed operation, it is likely that the support screen was choked. This conjecture is supported by the strong tòtal pressure variations which appear in boundary layer rake data and as perturbations on inlet total pressure measurements, as discussed in references 2 and 5. Thus it was decided to use average values of P_{max} and P_{min} in determining the distortion parameter.

Computation of the distortion parameter, $\frac{P_{max} - P_{min}}{P_{max}}$, resulted in a value of about 0.20 at design speed when average pressures in the distorted and undistorted regions of the rotor inlet were used. This value was somewhat higher than the intended value of 0.15.

Performance maps obtained from testing of Rotors 1B and 2B with radial distortion present are given in figures 15(a) and 15(b), respectively. The corresponding circumferential distortion maps are given in figures 16(a) and 16(b). A procedural change was made for the Rotor 2B distortion testing. Speed lines were obtained at 70%, 90% and 100% corrected speeds for the Rotor 2B testing since it was felt that these speeds would give better coverage of the performance map than the 50%, 70% and 100% speeds which had been used in the testing of Rotor 1B. Apart from this difference, the performance of the two rotors can be mutually compared. The distortion performance can also be compared with the performance obtained from

the testing of each rotor with a uniform inlet flow. The undistorted inlet performance is represented by dashed lines.

When the radial distortion performance of Rotors 1B and 2B is related to the performance of those rotors with an undistorted inlet flow (figures 15(a) and 15(b)), at low rotational speeds, no corrected flow or total-pressure ratio has been lost. In the case of Rotor 1B it does appear that a few efficiency points were lost at these low speeds. For both rotors the stall line is much lower on the map than the stall line obtained from testing with a uniform inlet flow.

At the higher speeds, in addition to efficiency and stall margin, both weight flow and pressure ratio were lost. The amounts by which the results of the distortion testing fell short of the undistorted-inlet performance are tabulated below:

Table 10. - Performance Losses due to 20% Radial Distortion at Design Speed

Rotor	1B	2B
% decrease in max. weight flow	2.5	2.7
Decrease in percent stall margin *	19.4	12.9
Decrease in peak efficiency	0.078	0.068

It is apparent that, at design speed, Rotors 1B and 2B lose about the same amounts of flow and efficiency when radial distortion is imposed. Rotor 1B loses more stall margin than Rotor 2B but, as we have seen, it did have a substantial stall margin advantage above peak efficiency operation during running with a uniform inlet flow.

Some typical total-temperature and total-pressure profiles obtained during running with radial distortion are shown in figures 17(a) and 17(b). It is seen that whereas for Rotor 1B the radial differences in total pressure have been smoothed out, in the case of Rotor 2B a sizeable proportion of the distortion does carry through to the rotor discharge. The 50% span data may be influenced by the wake from the part span shroud.

The circumferential distortion data for operation of Rotors 1B and 2B at low speed (figs. 16(a) and 16(b)) show very little total pressure or weight flow deficit. Little stall margin was lost during running at low speeds with circumferential distortion.

---

* For definition of decrease in stall margin, equation 1 was used. The numerator was taken at the radial distortion stall point and the denominator was taken at stall with an undistorted inlet flow.

At the higher rotational speeds, however, the picture is not as simple. With circumferential distortion at design speed no distinct stall point was noted. Instead, sporadic bursts of rotating stall were encountered which became progressively longer as the throttle valve was closed. This is indicated as a region of intermittent stall on the performance map. Throttling was terminated when a fully developed rotating stall was present. Another unusual feature is that the pressure ratio-weight flow characteristics are of a different shape from those obtained during uniform inlet testing. The difference is such that the characteristic does not show a vertical portion. It is therefore not relevant to quote a value for the decrease in maximum flow. However, it is evident that for both Rotors 1B and 2B the stall margin, weight flow and efficiency are considerably reduced from the values obtained from uniform inlet testing.

The circumferential distortion for Rotor 1B does carry through the rotor, as evidenced by rotor exit total pressure plots (fig. 18(a)). However, the equivalent plots for Rotor 2B (fig. 18(b)) show much larger variations of rotor exit total pressure. In this case the distortion has been amplified on passing through the rotor, especially in the vicinity of the hub.

The main qualitative differences, for both Rotor 1B and for Rotor 2B, between the performance maps obtained with radial distortion and those obtained with circumferential distortion, are in the shape of the design-speed line and in the shape of the stall line. The design-speed speed line for operation with radial distortion is flow limited whereas with circumferential distortion the flow limit is not reached and the characteristic has less curvature. The amount of stall margin lost, at design speed, is about the same with radial and circumferential distortions; at lower speeds much more stall margin is lost with radial distortion than with circumferential distortion. The efficiency was appreciably reduced with both forms of inlet distortion.

DISCUSSION OF BLADE ELEMENT RESULTS

This portion of the report is devoted to a discussion of the blade element data. The effect of the various parameters on element efficiency is indicated and the different rotors are mutually compared on an element basis. The losses for each element are correlated with loading, and radial distributions of flow conditions are presented and discussed.

Loading and Camber Ratio Effects
on Element Efficiency at Design Speed

As pointed out in the Overall Performance section of this report, Rotor 1B was able to operate at its design point (i.e., at design pressure ratio and weight flow) with considerably more stall margin than any of the Rotors 2 possessed during operation at their design point. Rotor 1B was

designed for a total-pressure-ratio of 1.60 whereas the equivalent value for the Rotors 2 was 1.76. For all rotors the peak efficiency at design speed occurred reasonably near a constant-throttle line through the design point but for the Rotors 2, the peak efficiency occurred too close to the stall line to be useable in most applications.

In order to explain some of the differences in the effects of loading on the overall and stalling performances of the different rotors, it is necessary to investigate the effect of loading on the performance of each radial element.

At design speed, the different radial elements of each rotor did not, in general, load up at the same rate as the throttle valve was closed. This is evidenced by figure 19, a fairly typical example of the manner in which one of the rotors (Rotor 2B) attained an increasing level of loading. The plot gives spanwise variations of blade-element total-pressure-ratio for the rotor. As is usually the case when a rotor is throttled at design speed, the tip element of Rotor 2B acquired loading much more rapidly than the hub element. It may also be seen from such a plot that at no particular flow condition is the design intent of radially constant total-pressure-ratio achieved.

Figure 20 shows how the efficiencies of the different elements of the four rotors vary as the rotors are throttled at design speed. Element total-pressure ratio has been used as abscissa rather than incidence angle because it provides a better display of the data.

Figure 20(a) gives the results for the tip element. Rotor 1B is seen to have superior performance. Wide differences are recorded between the three Rotors 2. These differences are such that, at low levels of element total-pressure ratio, Rotors 2E and 2D give substantially higher tip-element efficiency than Rotor 2B. As the total-pressure ratio over the element is raised, the tip-element efficiencies of these three rotors become more equal. It is probable that the smaller throat area at the tip of Rotor 2B, when compared with the throat area at its mean diameter (ref. 1, fig. 7 (a)), is responsible for the poorer performance of its tip element with low back pressures.

The characteristics at the 30% immersion are shown in figure 20(b). The element efficiencies of Rotors 2D and 2E reach a peak, whereas the Rotor 2B element efficiencies continue to climb within the measurement range. Otherwise the general shape of the curves is not very different for all three of the Rotors 2. Similar comments apply to the results obtained at the 50% immersion (fig. 20(c)), although it should be noted that for some flow conditions the wake of the part-span shroud impinged upon this element.

The data at the 70% immersion also seem to resemble each other, although the slopes of the characteristics are less steep than at other immersions. Once more the Rotor 2B curve is still climbing within the

range of the measurements. At each of the 50%, 70% and 90% immersions the blade shapes are identical for the Rotors 2.

At the immersion nearest to the hub all characteristics climb steeply (fig. 20(e)), Rotor 2D gaining most in element efficiency as the rotor is throttled. None of the hub characteristics reaches a peak. This behavior is in line with the low levels of loss coefficient which were seen in the blade element data at this immersion (references 2 through 5). The poor performance of Rotor 2D at the lowest back pressure is probably caused by the same phenomenon that hurt Rotor 2B at the tip at low back pressure: with a radially uneven distribution of throat area (ref. 1, fig. 7(a)) choking losses are high where the throat area is small.

Figure 21 presents values of blade element efficiency obtained from testing the Rotors 2, plotted as a function of the appropriate camber ratio for each element. Since the blades all have the same value of camber ratio at the radii corresponding to the 50%, 70% and 90% immersions, only the two immersions nearest to the casing are examined. In order to display efficiency differences an unusually large scale has been used; the inherent accuracy of the data should therefore be recalled when drawing conclusions from this figure. Data are given in figure 21 which correspond to both peak efficiency conditions and to a 15% stall margin.

An important point is that, unlike the overall performance results which were given as a function of tip camber ratio (fig. 10), the values plotted in figure 21 actually correspond to the fixed instrumentation reading nearest to peak efficiency or 15% stall margin. Figure 10 was based on the faired curve of figure 8 and the values given in figure 10 therefore applied exactly to conditions at peak efficiency or 15% stall margin. As it was not meaningful to plot element efficiencies against stall margin the element efficiencies were read directly from fixed instrumentation values which were computed for the nearest green reading.

Although the scatter, caused by the distribution of fixed instrumentation readings along the speed line, partially explains why the element efficiencies of Rotor 2E are higher than those of Rotor 2B, at least a part of this effect is genuine. The overall efficiency of Rotor 2B is slightly higher than that of Rotor 2E because the element efficiencies recorded at the third, fourth and fifth immersions are higher for Rotor 2B than for Rotor 2E. The reason for such behavior is not clear, since all geometrical variations between the different Rotors 2 occur at radial locations corresponding to the first and second immersions.

Blade Element Efficiencies at Other Speeds

In figure 22 the element efficiencies of Rotors 2B, 2E and 2D, at each immersion, are presented as a function of rotational speed. The readings nearest to the peak efficiency, at each speed, are connected by solid lines. The data nearest to the constant throttle line having 15% stall margin at design speed are indicated by dashed lines.

Except in isolated instances, the trends of the peak element efficiency curves are similar to those of the constant-throttle-line curves. The small differences which do occur are not thought to be significant. Regrettably, the trends which were present in the plots of overall efficiency versus percent design speed (fig. 11) are not seen to be present with as much consistency in the element efficiency data. Rotor 2B, however, does reveal some of the expected characteristics of a rotor having a low camber ratio. At the lower rotational speeds, its efficiency over the outer portion of the rotor is lower than that of the other two rotors (figs. 22(a) and 22(b)). At the higher rotational speeds the element performance associated with Rotor 2B is similar to that obtained with the other two rotors, but still slightly poorer than that of Rotor 2E. It is, in fact, the three inner immersions of Rotor 2B that are responsible for its slight advantage over Rotor 2E in overall performance. This is inexplicable since the inboard sections of all three rotors are identical, within manufacturing accuracy.

As the rotational speed is increased, the element efficiency near the tip of each rotor falls off more rapidly than does the overall efficiency. On the other hand, the efficiency near the hub falls off more slowly when compared with the overall efficiency. Two factors which are thought to contribute to this tendency are the substantial shock losses present at the high tip speeds and the suspected centrifuging of low energy boundary layer air towards the tip.

For the 10% immersion results, presented in figure 22(a), the efficiencies of both Rotors 2B and 2D reach a peak at 70% design speed. That of Rotor 2E is highest at 50% design speed. This type of behavior is also present at the 30% immersion (fig. 22(b)) although it was not seen in the overall performance. It is not clear why the rotor having the intermediate camber ratio should have superior performance at 50% speed; it would normally be expected that the blade having a double-circular-arc section should have the better efficiency at low speed. Of course, the accuracy of the data is reduced at the lower speeds.

From the results obtained at the 70% and 90% immersions, evidence of unusual performance at the 100% and 110% speeds is present. At the 70% immersion the efficiency falls off rapidly between design speed and 110% corrected speed. It is interesting that this low element efficiency, at 110% corrected speed, should coincide with the low values of deviation angle which also occur at these conditions. The 90% immersion has a high element efficiency at 110% speed. This may be a result of the losses being centrifuged outwards from the hub.

Correlation Between Loss Parameter and Diffusion Factor

The use of a diffusion factor, as first postulated by Lieblein (ref. 9), and the subsequent correlation of either total-pressure-loss coefficient or total-pressure-loss parameter, as a function of this

diffusion factor, has led to better control of compressor blade loading than was previously available. Therefore, it is worthwhile to examine the performances of the present rotors using plots of these variables. Such plots are useful in assessing the element performances of the rotors in the light of previous experience and also in revealing the radial distributions of flow conditions.

Blade element data of acceptable quality were available from the testing of all four rotors. The accuracy of the velocities which were used is reflected in the checks of integrated weight flow which were performed for each traverse reading. The data are presented in the form of total-pressure-loss parameter as a function of diffusion factor (fig. 23(a)-23(e)). Total-pressure-loss parameter is preferred over total-pressure-loss coefficient because it includes the effects of solidity and discharge flow angle in such a way as to be more relevant to the aerodynamics of the blade row. The total-pressure-loss parameter is more closely related to the rotor blade drag coefficient than is the total-pressure-loss coefficient.

Because it is founded on a simplified flow model, the use of a diffusion factor is only intended for correlation of data in the region of 'design' or 'nominal' flow conditions. Accordingly, readings taken with a wide open throttle valve setting and readings very close to stall were not used in the correlation. There still exist, however, several different methods of correlation in which data could be categorized as 'nominal' or equivalent to 'design' conditions.

The use of the element data giving 'minimum loss' for that element, at each rotational speed, has been fruitful in the past, especially for low-speed cascade data. Such a basis was rejected for the plots under consideration, since at the tip immersion the minimum value of loss parameter obtained in the testing of the subject rotors occurred at the most open throttle valve setting, giving blade element loadings obviously lower than design.

The use of data based on a 15% stall margin was considered to be inappropriate for a loss parameter-diffusion factor correlation since this is not a conventional way of comparing element data and does not relate directly to the aerodynamic blade losses. ‖Use of a constant throttle line through the design point was prohibited because Rotor 2D had only 5.1% stall margin when operating at such a point; consequently, no blade 'element data were recorded under these conditions.

It was finally decided to correlate data on the basis of the peak efficiency point at all speeds. Since no readings were taken at design speed at exactly the point of peak efficiency, the three readings nearest to peak efficiency on the overall performance map were used. A similar procedure was used at other rotational speeds.

24

The plots of total-pressure-loss parameter versus diffusion factor are presented in figure 23. In addition to the blade element data, the NASA curves of reference 7 are indicated. The NASA curves came from double-circular-arc data and are not necessarily applicable to multiple circular arcs. These NASA curves are identical at the 30%, 50%, 70% and 90% immersions. Two different background curves are given at the 10% immersion. The upper of the two curves represents the average of all rotor tip data which were used in the NASA correlation. The lower curve represents the lower limit of the same data. It is clear from the NASA data that all compressors investigated have high losses in the rotor tip region and, although it seems that factors other than blade element diffusion are affecting the tip loss, the specific origin of these additional losses is not always certain. Conceivably, high losses could result from interaction of shocks with the casing boundary layer. However, examination of the data forming the tip element band of the NASA correlation suggests that the problem is not dependent upon the presence of shocks. It is more likely that the principle cause of high tip losses is a combination of tip clearance effects and secondary flows, augmented by movement of low energy air radially outwards over the aft portion of the rotor blades. The design conditions for Rotor 1B and the Rotors 2 are also included in each element plot. As explained in reference 1, the minimum level of the total-pressure-loss parameter band, with additive shock losses, was used to guide the design selection of the tip losses.

Figure 23(a) presents element data recorded at the 10% immersion. Virtually all of the data fall within the NASA band and most of these are in the region of the band having losses lower than the average for all rotors. The spread of the data is not great and the tip element data thus confirm the tip element band of the NASA correlation. In general, although the design-speed data reveal slightly higher loss levels than the design intent, these occur with a higher diffusion factor than design. The tip element performance at design speed is therefore equivalent to design intent.

At the 30% immersion (fig. 23(b)), it is seen that in general the NASA correlation curve gives a better representation of the average level of the data than do the design points, which contained an allowance for shock losses. Once more, the spread of the data is not great for most of the readings. An exception to this occurs for the 110% speed readings from the Rotor 2 tests. These are consistently above the level of the other data. This is another manifestation of the sudden decrease in efficiency which occurred for the Rotors 2 at overspeed conditions (fig. 11) and is possibly a result of excess throat area. At this immersion the level of loss at design speed is lower than the design level. However, the level of diffusion is approximately the same as design.

The data presented in figure 23(c) have the same pattern as those in figure 23(b). Although the discharge flow angle traverses indicated that the part-span shroud wake impinged upon the cobra probe at the 50% immersion, no indication of unusually high losses is present in the fixed instrumentation data presented here. Once more the data form a relatively

tight band around the empirically-derived NASA curve with the exception of the data obtained from the Rotors 2 at 110% speed.

The data presented at the 70% and 90% immersions have important differences from those nearer to the rotor tip. Almost all data give much lower losses than the NASA curve, with the exception of the 110% speed data for the Rotors 2 which, at the 70% immersion, reveal an even higher loss than the NASA curve.

The design speed losses for both of these immersions are considerably lower than the design values whereas the diffusion factors at design speed are not greatly different from the design intent. This superior performance may be a result of centrifuging of the blade boundary layers radially outward from the hub. For both the 70% and 90% immersion some negative values of total-pressure-loss parameter were measured at 50% and 70% speed. Small measurement errors and scatter in the corrected values are believed to be responsible for this anomaly.

The loss data have demonstrated that rotors designed for the high transonic Mach number range do not have substantially higher losses than subsonic and low transonic rotors when properly shaped blade elements are employed.

Radial Distributions of Flow Conditions

In order to determine the accuracy of the design assumptions, graphs of measured Mach number and axial velocity have been plotted in figures 24, 25, 26 and 27. This has been performed for Rotors 1B and 2B. The reading nearest to a constant throttle line passing through the design point of each of these rotors has been used.

At the inlet and discharge of both rotors, radial distributions of design conditions have also been given. A continuous traverse was taken in plane 1.51 for both rotors and distributions reduced from this traverse are also included. Axial velocities and Mach numbers, reduced from cobra traverse data, in addition to data reduced from a continuous cobra traverse, may therefore be compared with design intent. The readings used for traverses are identified on the appropriate performance maps (figs. 5(a) and 5(b)).

In figure 24 radial distributions of inlet and discharge relative Mach number are compared with the corresponding design curves for Rotor 1B. The agreement between the measured inlet Mach number and the design curve is excellent. Close agreement is also obtained between the element data and the reduced continuous traverse at rotor discharge. Those values are slightly lower than the design Mach number at the hub, but this is probably a result of the fact that design distributions of total pressure are faired to the wall instead of representing the hub and casing boundary layers. The wake of the part-span shroud is also recorded by the continuous traverse.

The radial distributions of axial velocity for Rotor 1B are presented in figure 25. The measured inlet axial velocity is slightly higher than the design curve, reflecting the higher weight flow which was recorded in the overall performance data. At rotor discharge, the measured values of axial velocity were generally lower than the design distribution, particularly in the hub region.

The measured inlet relative Mach numbers for Rotor 2B (fig. 26) also compare well with design intent. The agreement between test data and design intent at rotor discharge is also reasonable, although once more the effects of hub and casing boundary layers and the part-span shroud are evident in the reduction of the continuous traverse data.

Figure 27 shows that the inlet axial velocities measured during the Rotor 2B test are again higher than the design values. This is consistent with the higher weight flow. The shape of the axial velocity distribution matches the design shape nicely, however. The Rotors 2 were designed for a high level of discharge axial velocity at the hub. Although there are signs of this trend in the free-stream flow, the hub boundary layer again prevents much of this axial velocity increase from being attained.

In order to mutually compare the radial distributions of blade incidence angle, these are presented for all four rotors in figure 28. The values presented were obtained from the blade element reduction procedure, in conjunction with the known blade edge angles for each rotor. For all rotors, the data were recorded at the intersection of the design speed line with a constant throttle line through their respective design points. These data are superposed on the appropriate design curves.

The differences between the element data and design intent reflect the differences between the measured and design weight flows. Small differences between the Rotor 2 incidences may be related to the different tip throat areas of the three rotors.

Deviation angles are plotted in figure 29. These again resulted from the blade element data reduction and the known blade edge angles. The readings from which these deviation angle data were obtained were the readings which were used for the incidence angle data in figure 28.

The deviation angles of Rotor 1B are higher than design intent for all radial positions. This is an unexpected finding since the overall performance map (fig. 5(a)) indicates that the design total-pressure ratio was exceeded at design flow. These results imply that the actual axial velocities at rotor discharge were less than design. This is substantiated by the axial velocity measurements. These, and the weight flow checks at the rotor exit traverse plane (table 6 of ref. 2), suggest that the design effective-area coefficient value of 0.95 was too low.

The Rotors 2 have differences in deviation angle which do not appear to form a consistent pattern. In general, however, they agree better with

design intent than those of Rotor 1B. For Rotor 2D, the reading which was used was close to the stall point. It is possible that the overturning present at the tip section is a result of a separation region giving higher effective camber at the rear of the blade.

SUMMARY OF RESULTS

The significant conclusions drawn from the testing of the four rotors are as follows:

1. For operation at design speed with a 15% stall margin, Rotor 1B had an efficiency of 0.895 whereas the efficiency of the more heavily loaded Rotor 2B was 0.876. Measured total-pressure-loss coefficients were lower than their design values for all rotors and at all immersions except the tip, where good agreement with design was obtained.

2. Rotor 1B had a considerable stall-free operating range beyond its design pressure ratio and weight flow. The Rotors 2 all were poorer in this respect. At a 15% stall margin, the operating total-pressure ratio for Rotor 1B was almost as good as that for Rotors 2B and 2E and better than that of Rotor 2D. Decreases in the tip ratio of supersonic to total camber over the range tested generally resulted in the achievement of higher stall lines.

3. During the operation of the three Rotors 2 at a design-speed stall margin of 15%, the rotor having a double-circular-arc tip section had an overall efficiency of 0.854, the rotor with an intermediate camber ratio had an efficiency of 0.869 and the rotor with least supersonic camber had an efficiency of 0.876. Thus, decreases in tip ratio of supersonic to total camber over the range tested resulted in the achievement of higher overall efficiencies.

4. The design rules used led to all rotors exceeding design weight flow. Part of this flow excess can be related to the wall boundary layer blockage assumption and part may be attributed to an excessive allowance for throat area. Incidence angles lower than design were obtained. At design flow all rotors tended to produce a total-pressure ratio greater than design. Blade element measurements suggest that this was a result of the design annulus effective-area coefficient being too low rather than the design deviation angle being too high.

5. The shapes of the radial distributions of axial velocity were accurately predicted at the rotor inlet by the design procedure employed. The agreement at rotor discharge was reasonable, although wall boundary layers and the part-span shroud wake made direct comparisons difficult.

6. Both radial and circumferential distortions had a substantial influence on rotor performance. At design speed the stall margin, weight flow and rotor efficiency were considerably reduced below the values obtained from uniform inlet testing.

REFERENCES

1. Seyler, D. R., and Smith, L. H., Jr.: Single Stage Experimental Evaluation of High Mach Number Compressor Rotor Blading, Part 1 - Design of Rotor Blading, NASA CR-54581, April 1, 1967.

2. Seyler, D. R., and Gostelow, J. P.: Single Stage Experimental Evaluation of High Mach Number Compressor Rotor Blading, Part 2 - Performance of Rotor 1B, NASA CR-54582, September 22, 1967.

3. Gostelow, J. P., and Krabacher, K. W.: Single Stage Experimental Evaluation of High Mach Number Compressor Rotor Blading, Part 3 - Performance of Rotor 2E, NASA CR-54583, September 29, 1967.

4. Krabacher, K. W., and Gostelow, J. P.: Single Stage Experimental Evaluation of High Mach Number Compressor Rotor Blading, Part 4 - Performance of Rotor 2D, NASA CR-54584, October 6, 1967.

5. Gostelow, J. P., and Krabacher, K. W.: Single Stage Experimental Evaluation of High Mach Number Compressor Rotor Blading, Part 5 - Performance of Rotor 2B, NASA CR-54585, October 13, 1967.

6. Miller, Genevieve R., Lewis, George W., Jr., and Hartmann, Melvin, J.: Shock Losses in Transonic Compressor Blade Rows, Journal of Engineering for Power, Trans. ASME, Series A, Vol. 83, July 1961, pp. 235.

7. Robbins, William H., Jackson, Robert J., and Lieblein, Seymour: Blade-Element Flow in Annular Cascades, Aerodynamic Design of Axial-Flow Compressors, NASA SP-36, Chapt. VII, 1965, pp. 227-254.

8. Smith, L. H., Jr., and Yeh, Hsuan: Sweep and Dihedral Effects in Axial-Flow Turbomachinery, Journal of Basic Engineering, Trans. ASME, Series D., Vol. 85, 1963, pp. 401-416.

9. Lieblein, Seymour, Schwenk, Francis C., and Broderick, Robert L.: Diffusion Factor for Estimating Losses and Limiting Blade Loadings in Axial-Flow Compressor Blade Elements, NACA RME53D01, 1953.

Flow direction

1B

2B

2E

2D
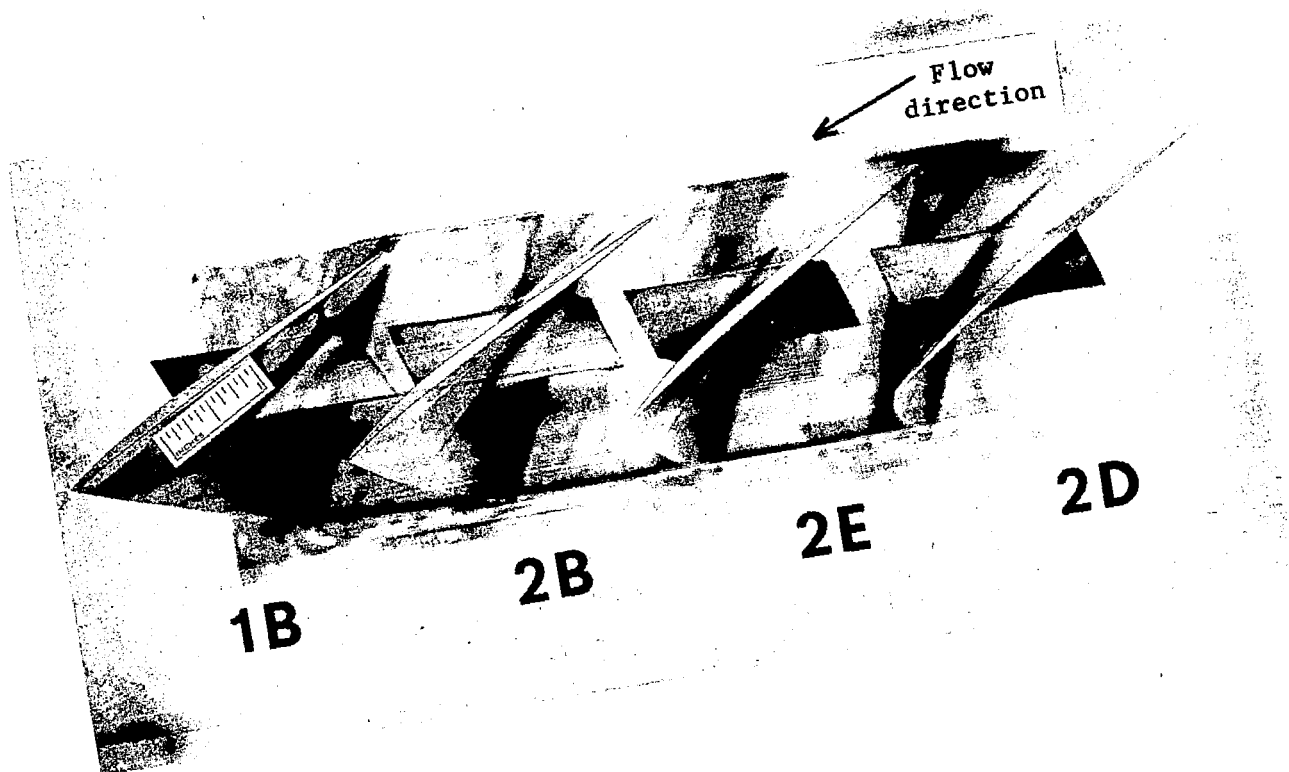
Figure 1. - Close-up view of the tip section of all four rotors.
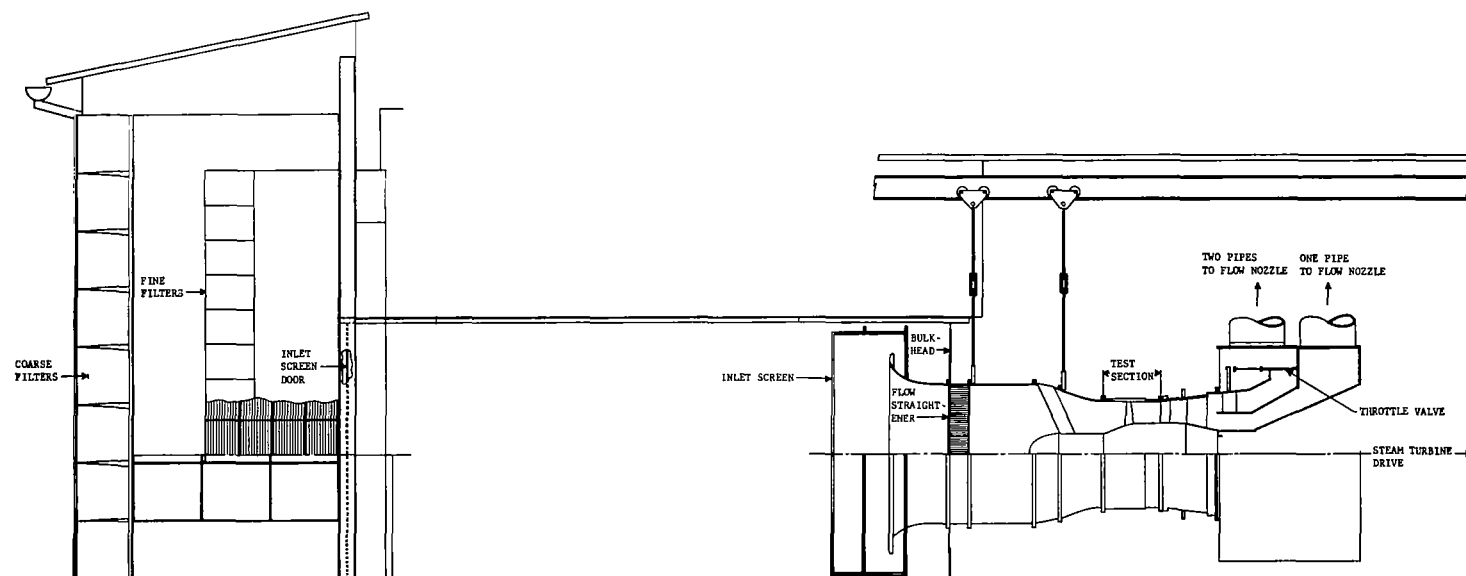
Figure 2. - House Compressor Test Facility.

Z=-27000
Z=-23000
Z=-19000
Z=-15000
Z=-12000
Z=-8000
Z=0
Z=.511
Z=.852
Z=1.193
Z=1.533
Z=1.874
Z=2.214
Z=2.555
Z=3.066
Z=.187
Z=.365
Z=4.380
Z=6.000
Z=8.874
Z=-5.840
Z=-1.825
Z=-1.095
Z=-2.920
Z=11800

CASING CONTOUR FOR ROTORS 1&2
Z=14452 OGV STACK
OGV
ROTOR

HUB CONTOUR / CASING / AXIAL

ROTOR-1 RAD	ROTOR-2 RAD	CONTOUR RAD	LOCATION Z	CAFD STA DESIGNATION
7.053	7.053	22.835	-27000	
7.100	7.100	21.405	-23000	
7.100	7.100	19.990	-19000	
7.100	7.100	18.878	-15000	
7.100	7.100	18.484	-12000	3
7.100	7.100	18.412	-10000	4
7.238	7.210	18.394	-5840	7
8.088	7.810	18.379	-2920	84
8.477	8.220	18.351	-1825	9
8.737	8.550	18.323	-1095	95
8.944	8.845	18.291	511	96
9.125	9.125	18.250	0	10
9.305	9.423	18.190	511	1017
			852	
			1192	
9.660	10.039	18.010	1533	105
			1874	
			2214	
9.996	10.584	17.871	2555	1083
10.141	10.784	17.845	3066	15
10.273	10.944	17.838	1450	51
10.377	11.065	17.836	4380	52
10.438	11.165	17.836	6000	54
10.439	11.169	17.836	8874	157
10.439	10.970	17.836	11800	16

PLANE 086

BOUNDARY LAYER RAKE	
	RAD
	ROTOR 1 & ROTOR 2
A	18.330
B	18.231
C	18.132
D	18.033
E	17.934
F	17.836
G	17.737
H	17.638
J	17.539
K	17.440
L	17.243
M	17.045
N	16.848
O	16.551
P	16.255

INLET PITOT-STATIC RAKES ARE AT PLANE 0.05 (Z=-44)

CAFD IS IDENTIFYING NAME FOR AXISYMMETRIC DESIGN CALCULATION PROCEDURE

ROTOR STACK
PLANE 01 DISTORTION SCREENS

PLANE 086
4 DISTORTION Pt RAKES - EQ SP

PLANE 095
COBRA PROBE TRAVERSE ANGLE Pt & Tt 5 CIRCUMFERENTIAL STATICS (ID & OD) EQ SP WEDGE TRAVERSE FOR STATIC PRESSURE

PLANE 151
COBRA PROBE TRAVERSE ANGLE Pt & Tt HOT WIRE ANEMOMETER TRAVERSE 5 CIRCUMFERENTIAL STATICS (ID & OD) EQ SP WEDGE TRAVERSE FOR STATIC PRESSURE GEARED TO YAW WITH COBRA PROBE

PLANE 157
4 Pt RAKES & 4 Tt RAKES 5 CIRCUMFERENTIAL STATICS (ID & OD)

HUB CONTOUR FOR ROTOR 2
HUB CONTOUR FOR ROTOR 1

VIEW A-A
VIEW B-B

Figure 3. – Meridional view showing location of instrumentation.
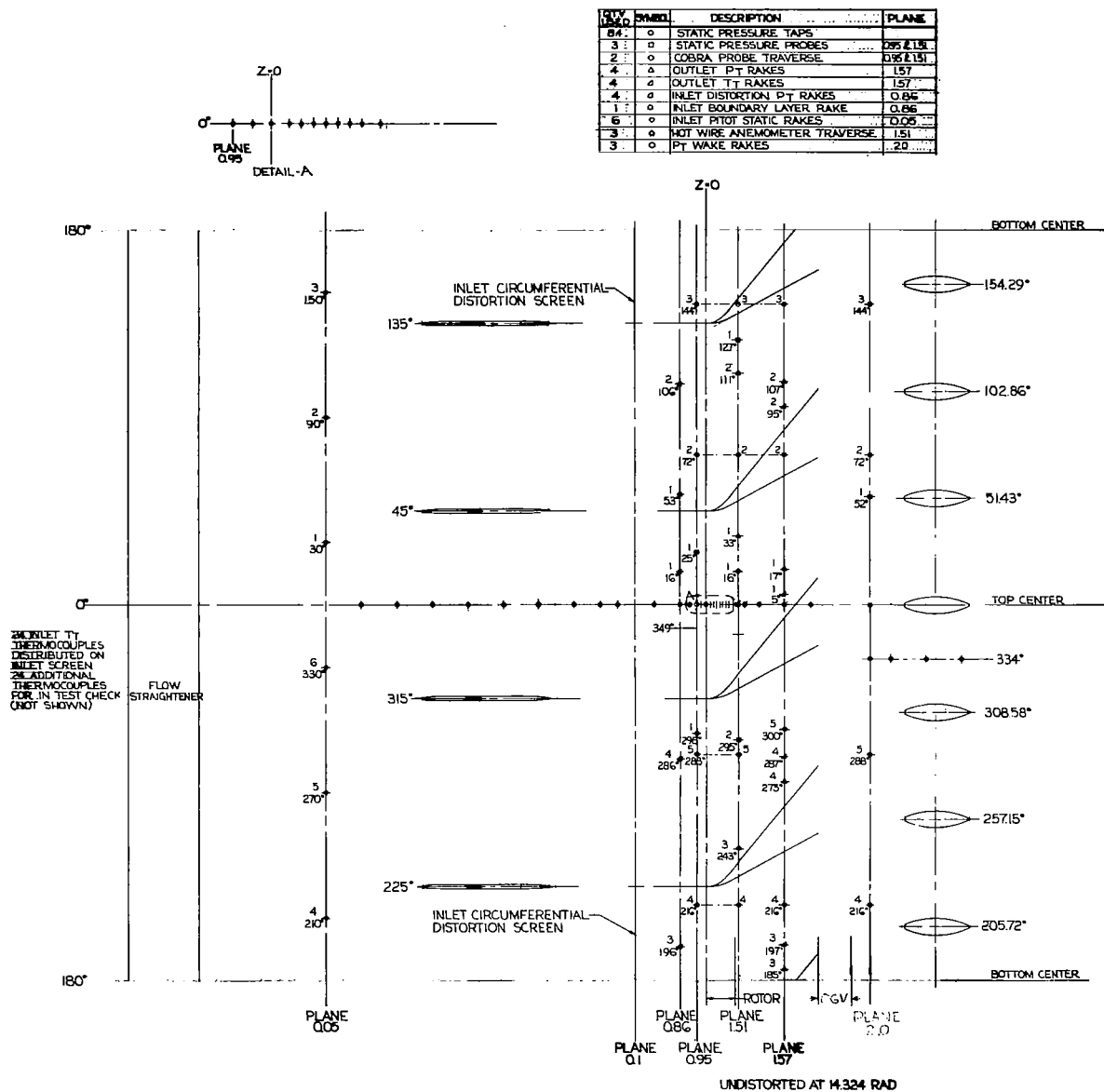
Figure 4. – Development showing circumferential location of instrumentation.

Corrected weight flow per unit annulus area, $\dfrac{w\sqrt{\theta}}{\delta A_{an}}$,lb/sec-sq ft
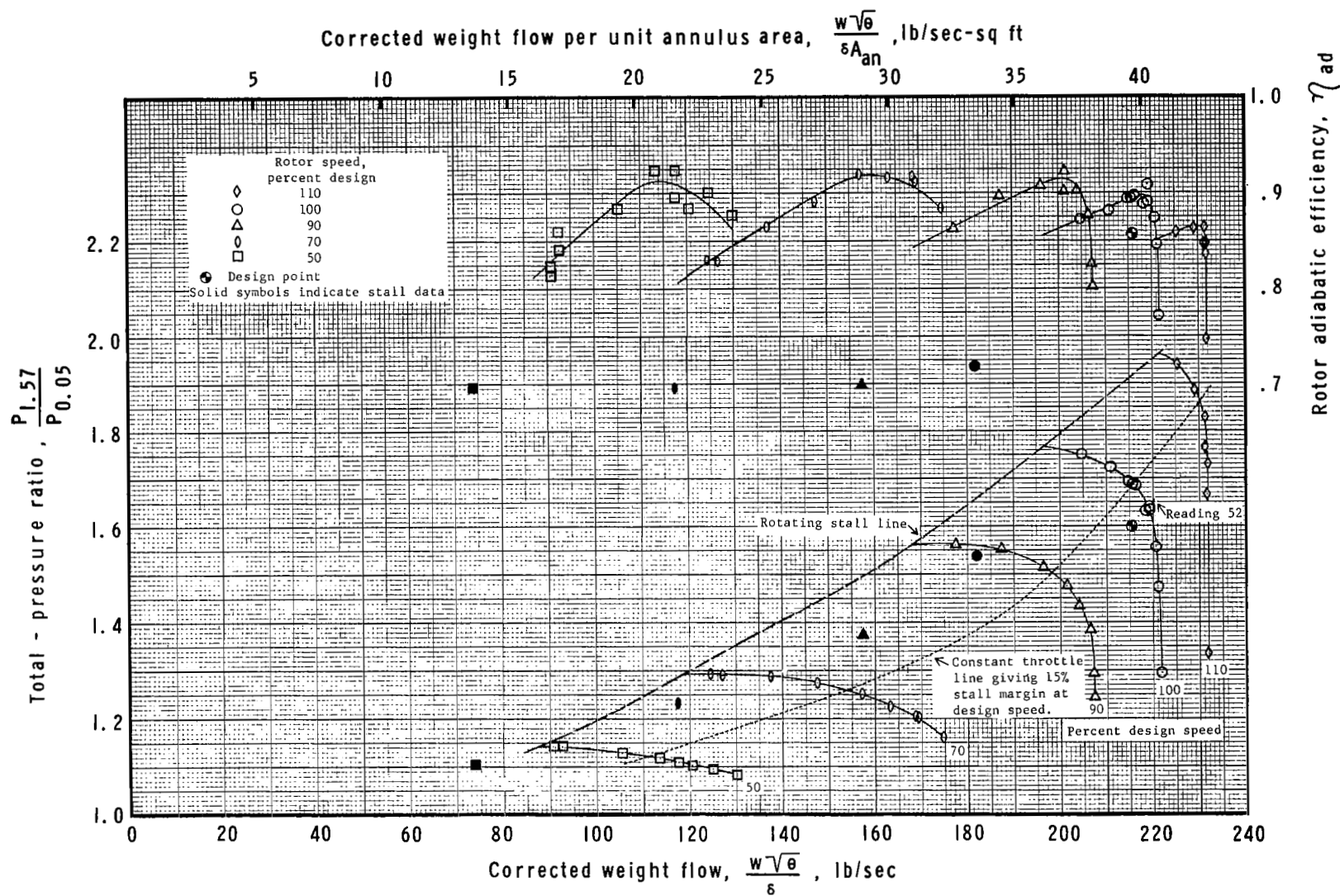
Figure 5(a). – Rotor 1B performance map obtained with uniform inlet flow.
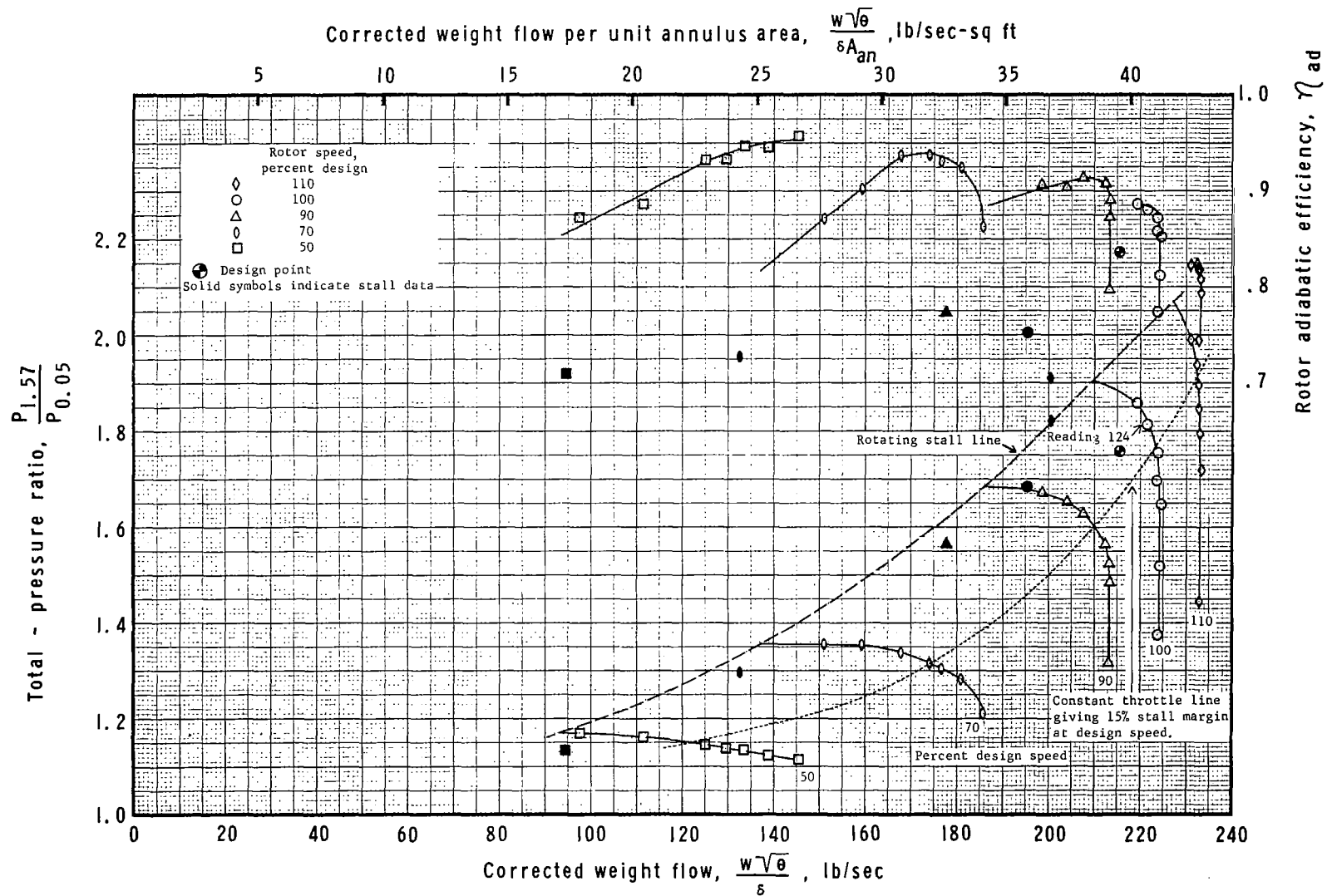
Figure 5(b). – Rotor 2B performance map obtained with uniform inlet flow.
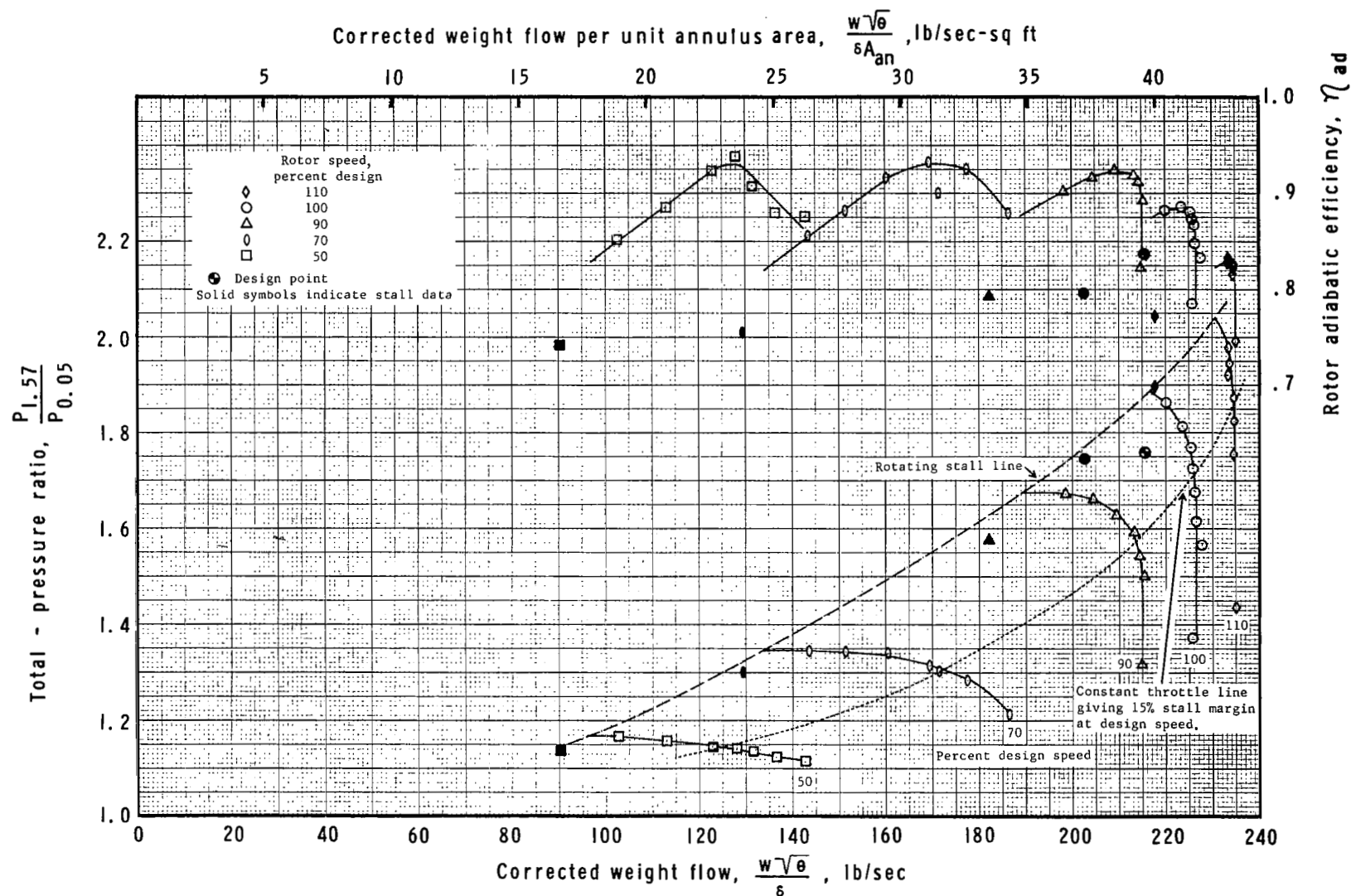
Figure 5(c). - Rotor 2E performance map obtained with uniform inlet flow.
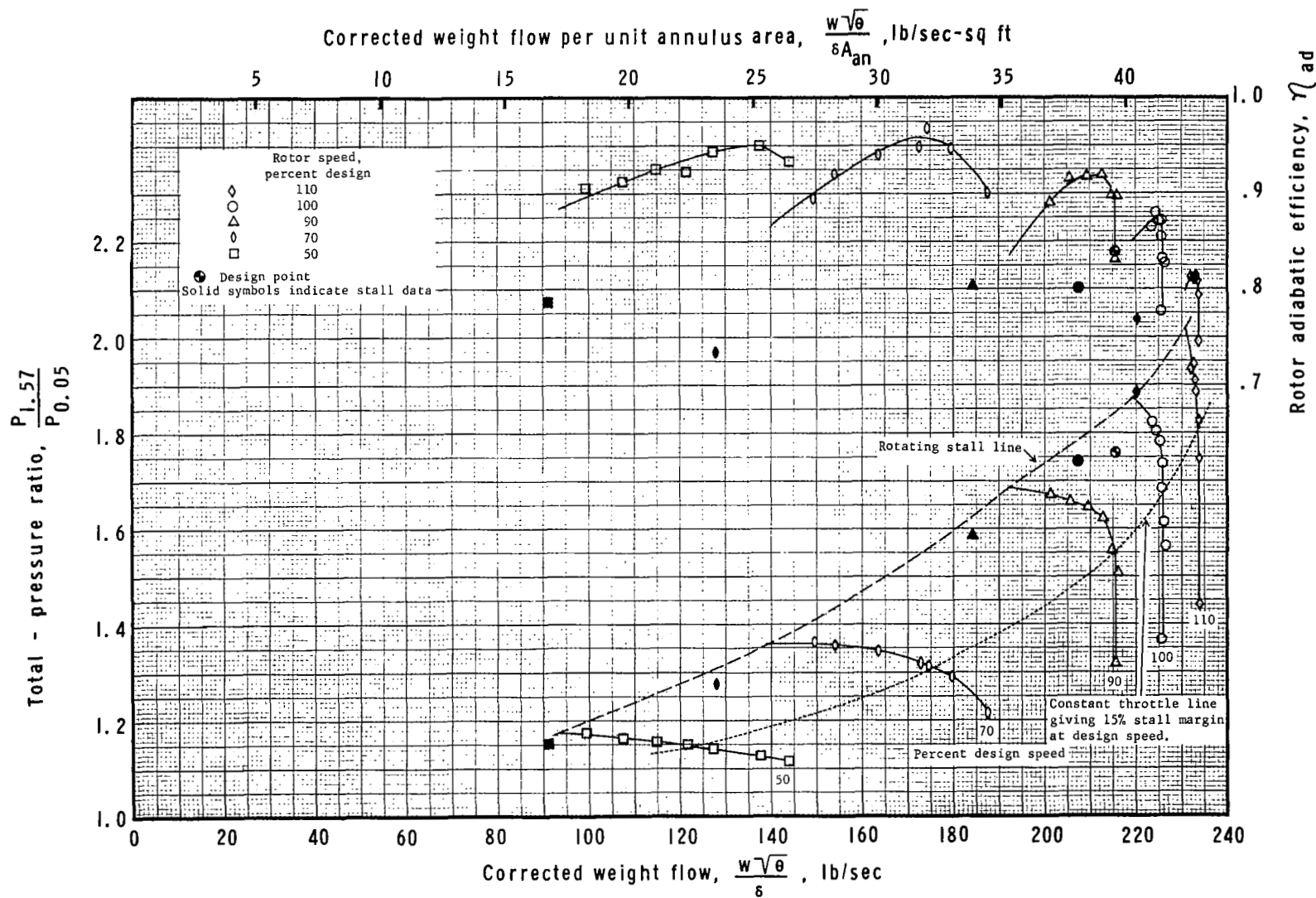
Figure 5(d). – Rotor 2D performance map obtained with uniform inlet flow.
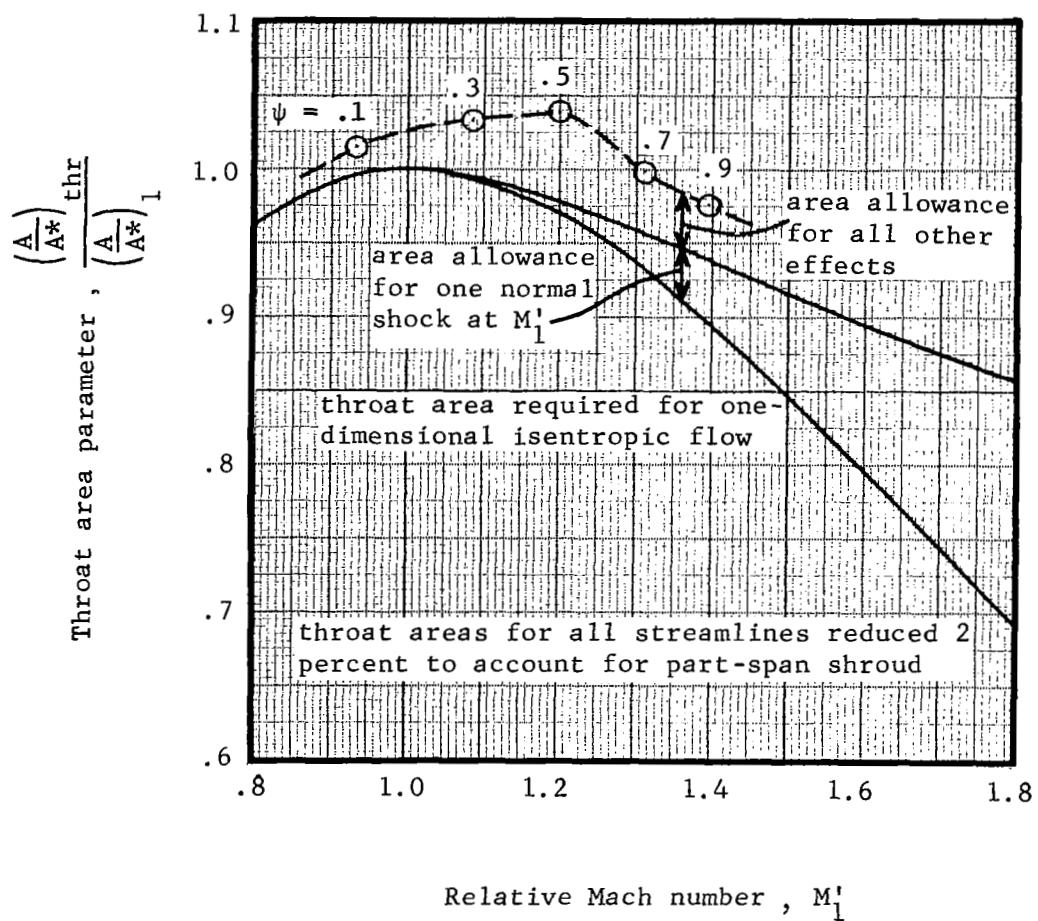
Figure 6. - Throat area allowances for Rotor 1B.
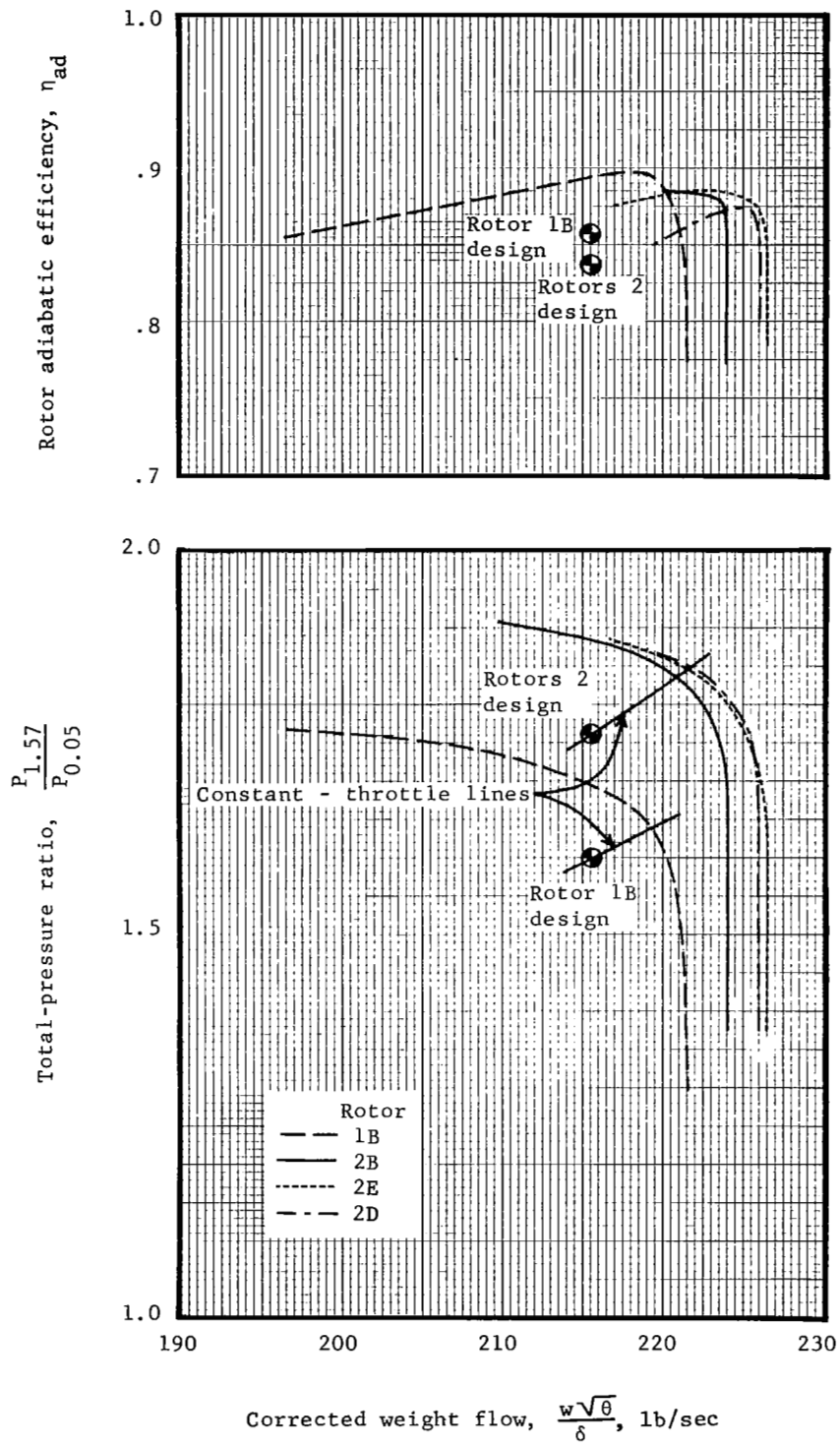
Figure 7. - Composite plot giving design speed performance of each rotor.
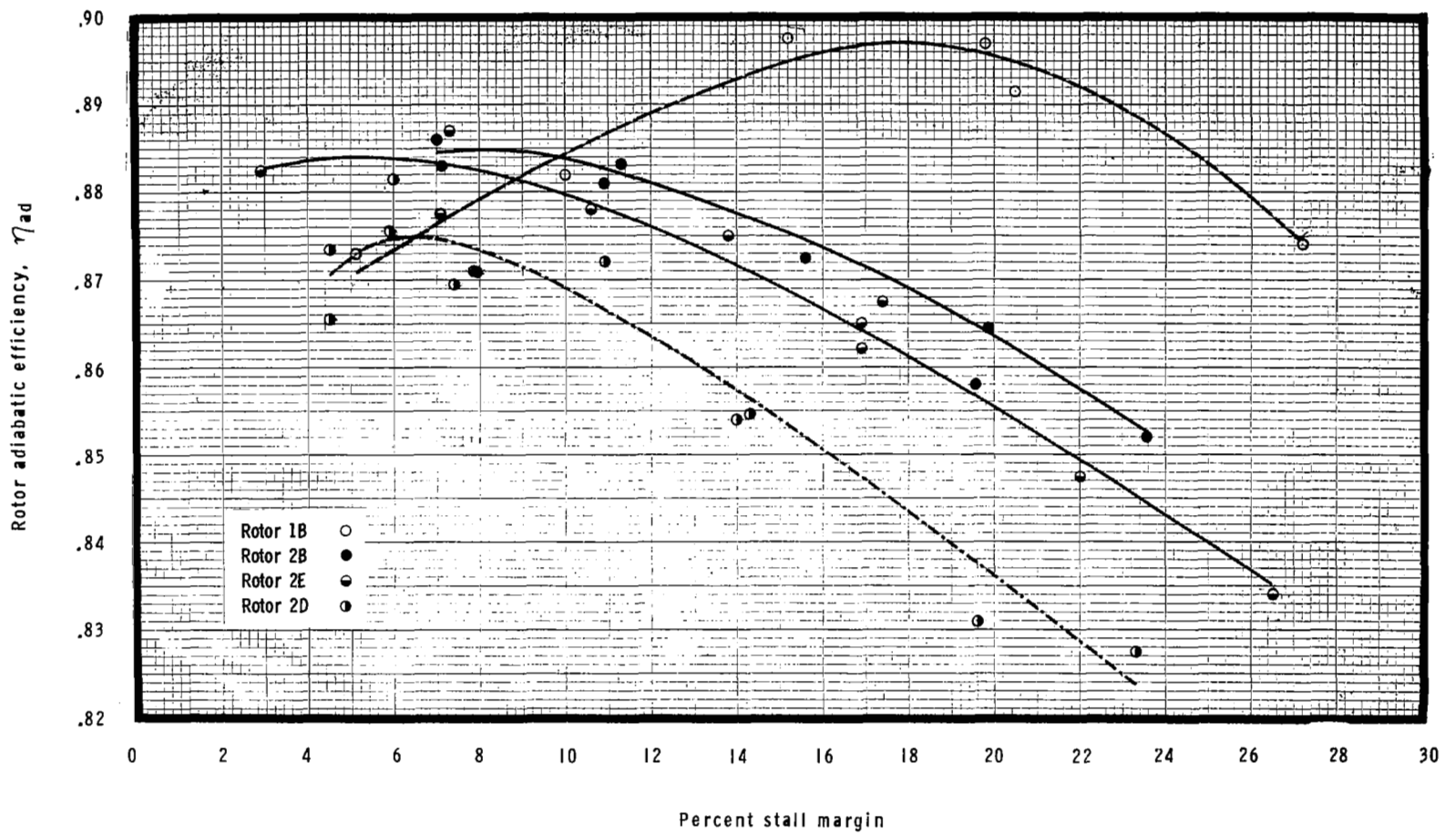
Figure 8. - Overall rotor efficiencies for different stall margins at design speed.
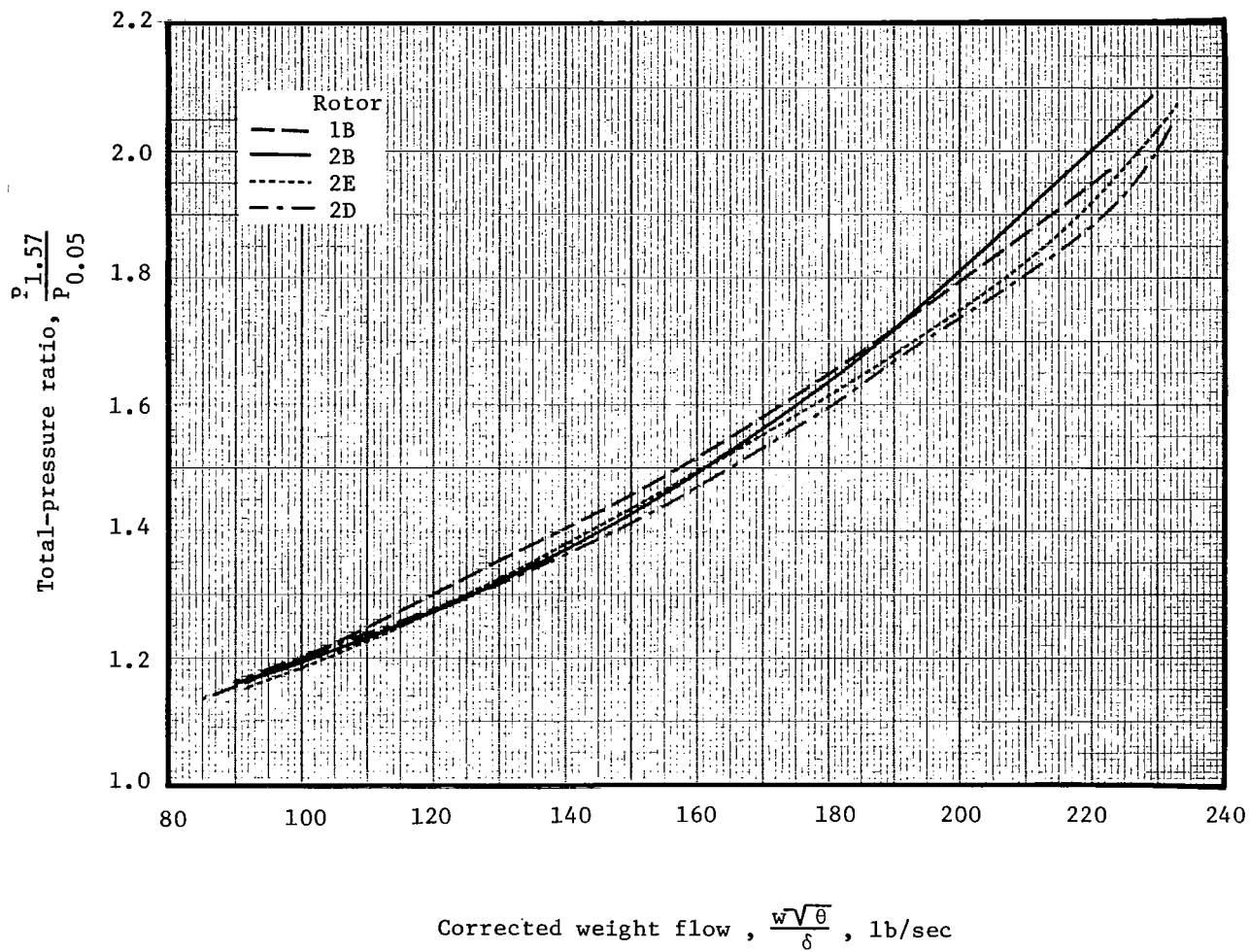
Figure 9. – Composite plot showing stall lines of different rotors.
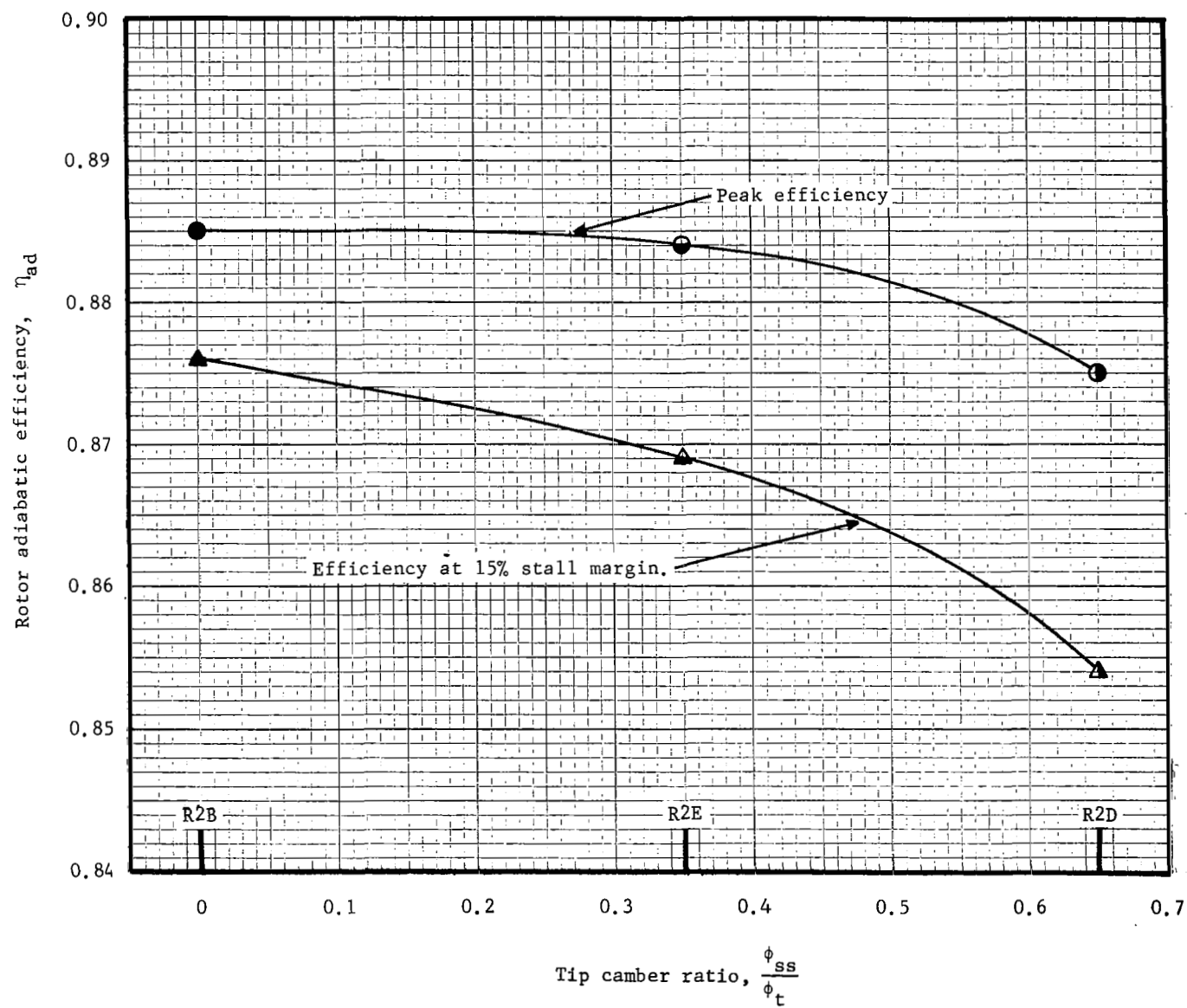
Figure 10. - Overall rotor efficiency as a function of tip camber ratio.
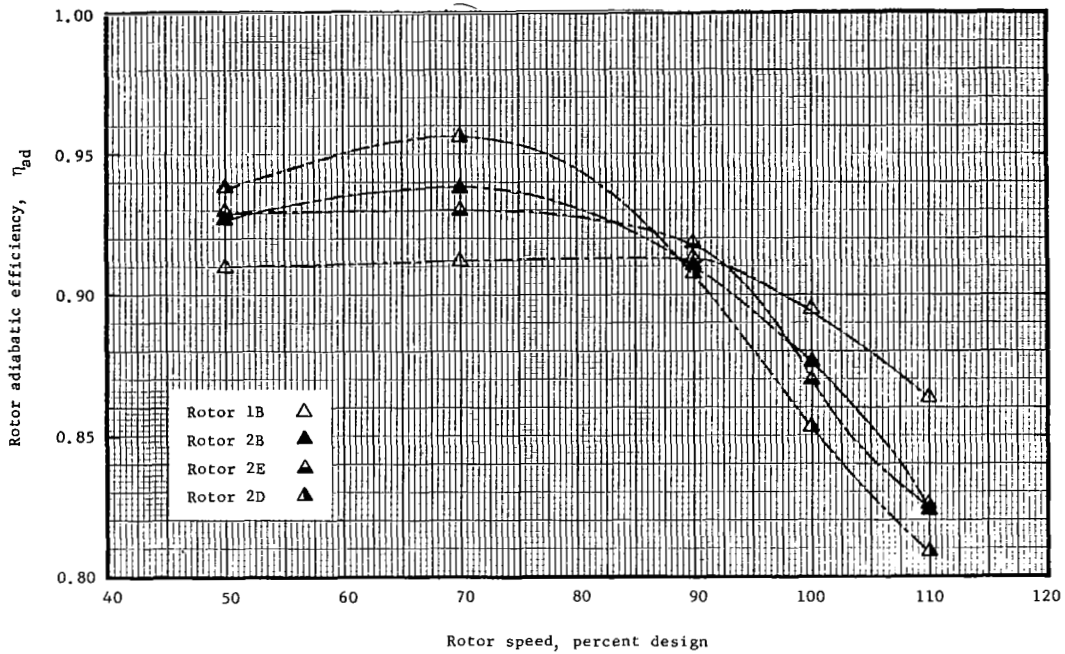
Figure 11(a). - Efficiencies at different rotational speeds along constant-throttle lines having 15 percent stall margin at design speed.
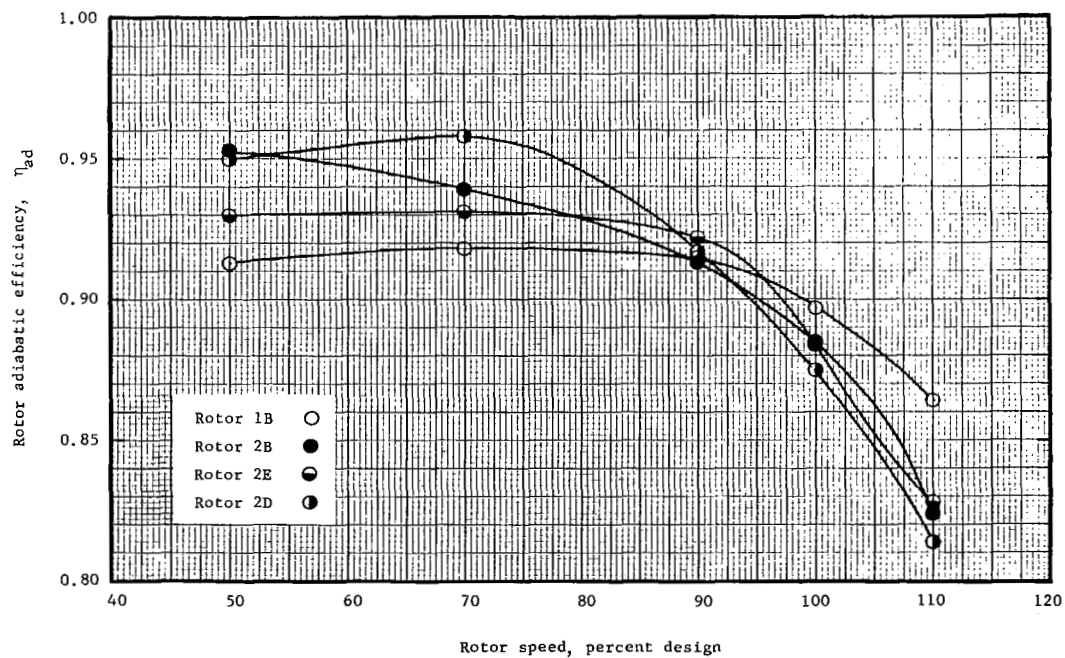
Figure 11(b). - Peak efficiencies at different rotational speeds.

43
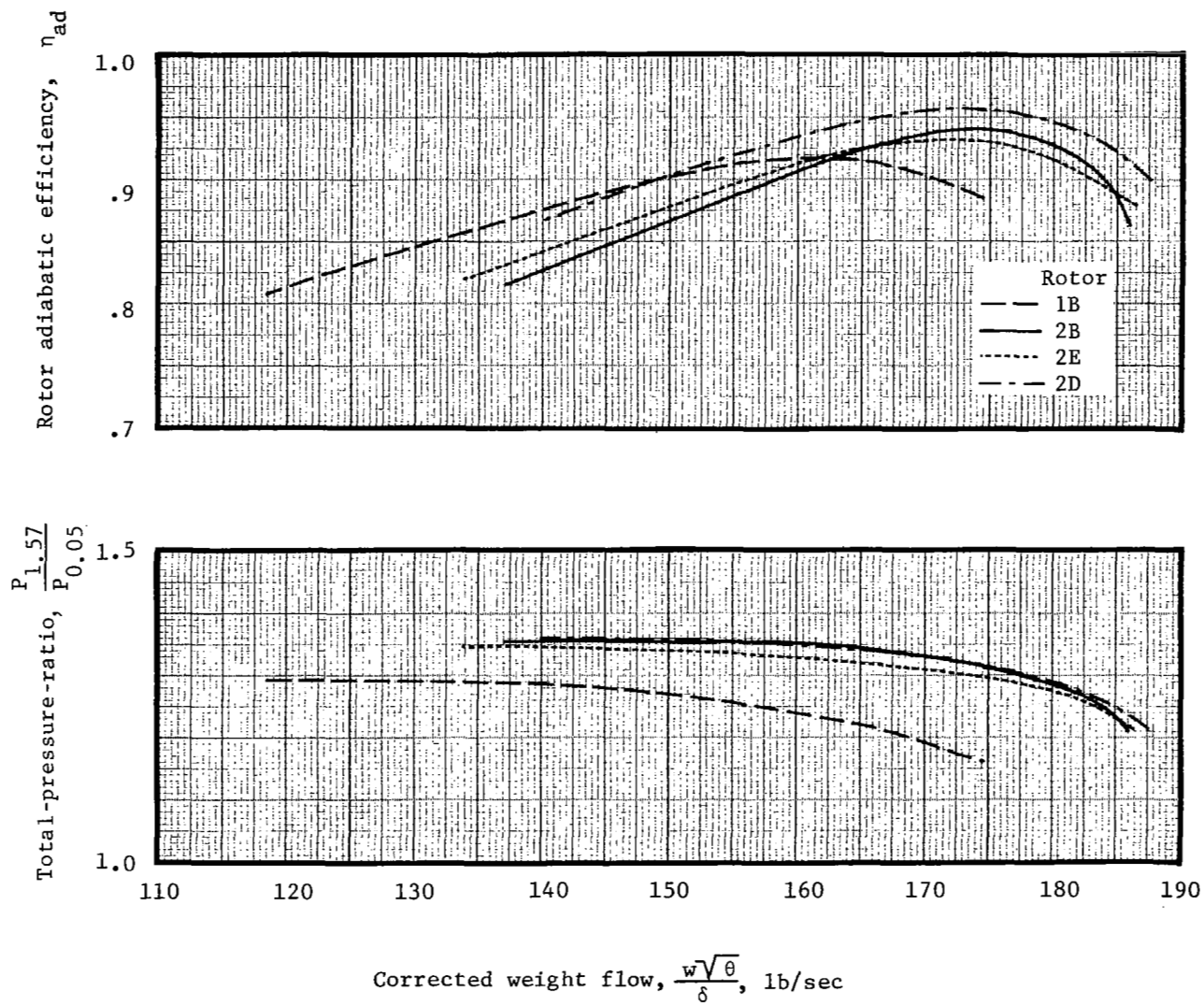
Figure 12. – Composite plot giving performance of each rotor at 70 percent speed.

The graph has a top panel with y-axis labeled "Rotor adiabatic efficiency, η_{ad}" ranging from .7 to 1.0, and a bottom panel with y-axis labeled "Total-pressure-ratio, $\dfrac{P_{1.57}}{P_{0.05}}$" ranging from 1.0 to 1.5. The x-axis is labeled "Corrected weight flow, $\dfrac{w\sqrt{\theta}}{\delta}$, lb/sec" ranging from 110 to 190.

Legend:

Rotor	
———	1B
———	2B
········	2E
—·—·—	2D

44
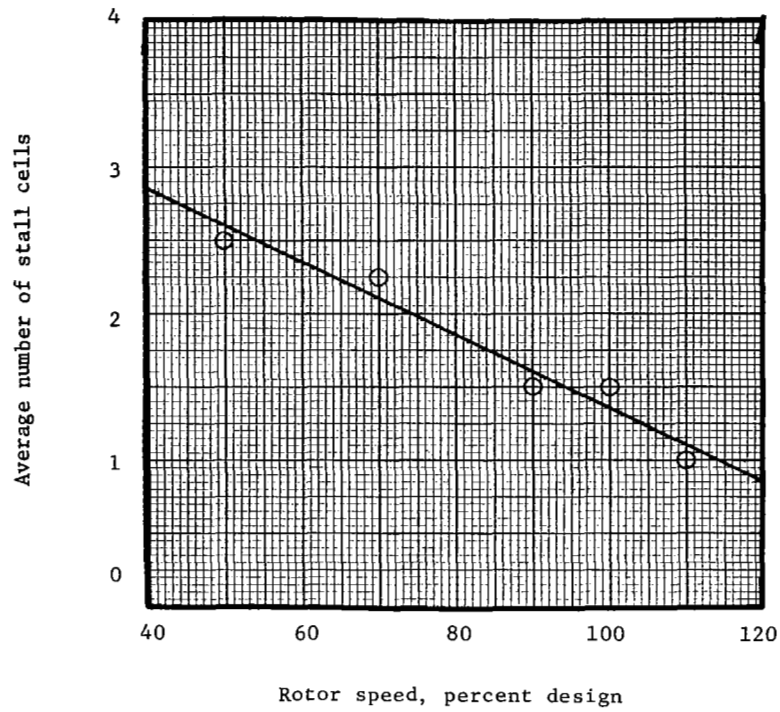
Figure 13(a). - Average number of stall cells at each rotational speed.
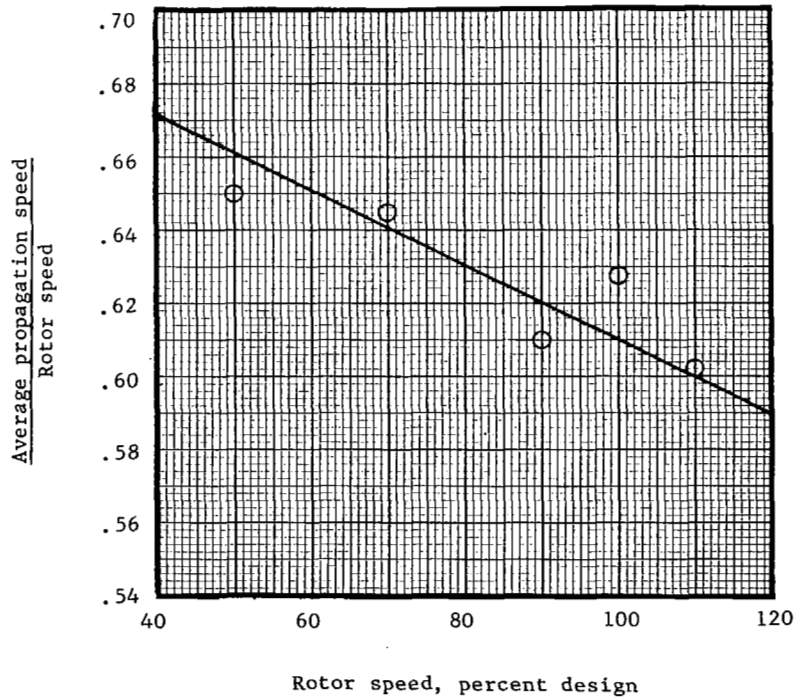
Figure 13(b). - Average propagation speed of stall cells at each rotational speed.
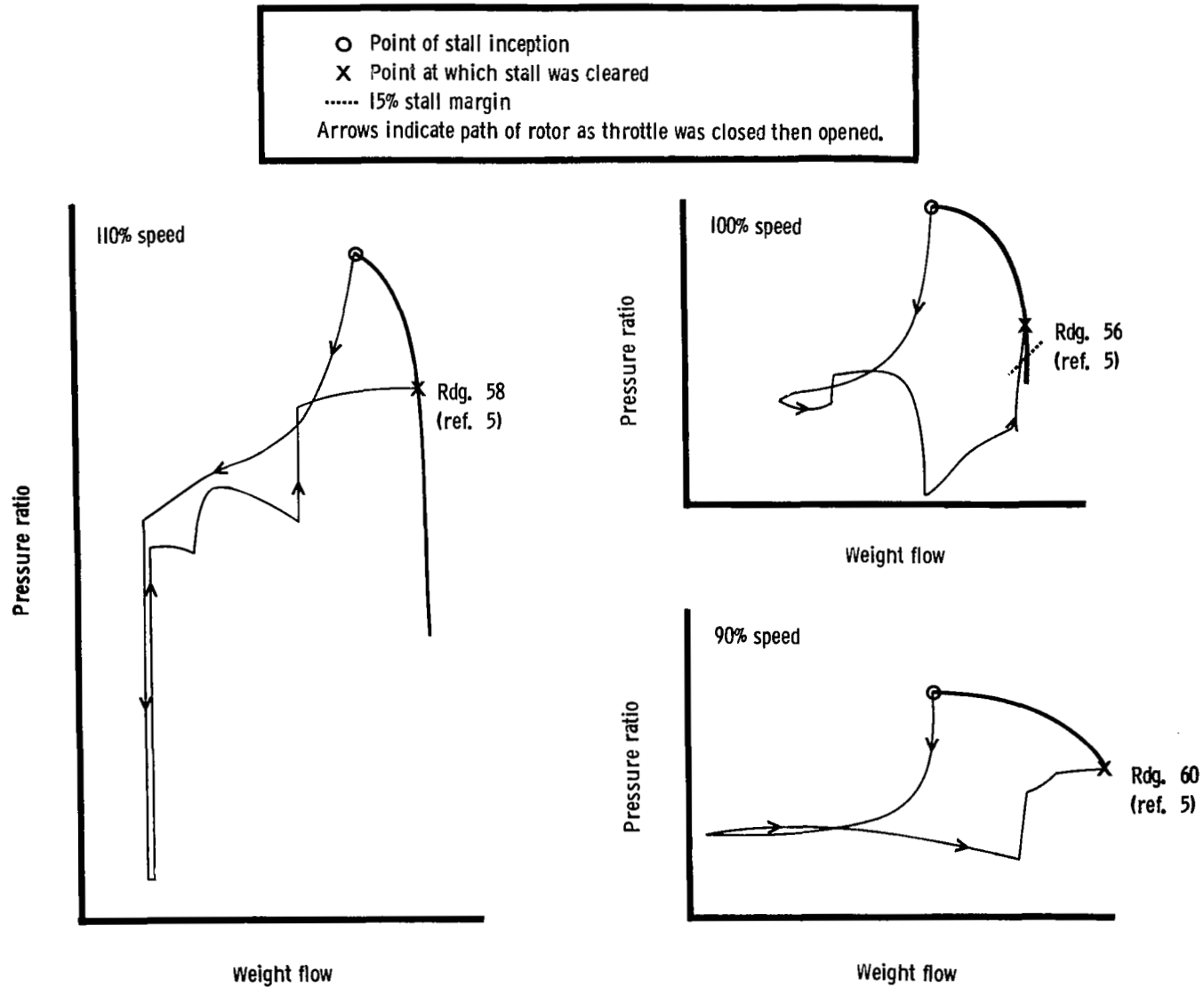
Figure 14. - Qualitative plots showing extent of hysteresis loops obtained when Rotor 2B was slowly withdrawn from stall at 90%, 100% and 110% corrected speeds.

Corrected weight flow per unit annulus area, $\frac{w\sqrt{\theta}}{\delta A_{an}}$, lb/sec-sq ft
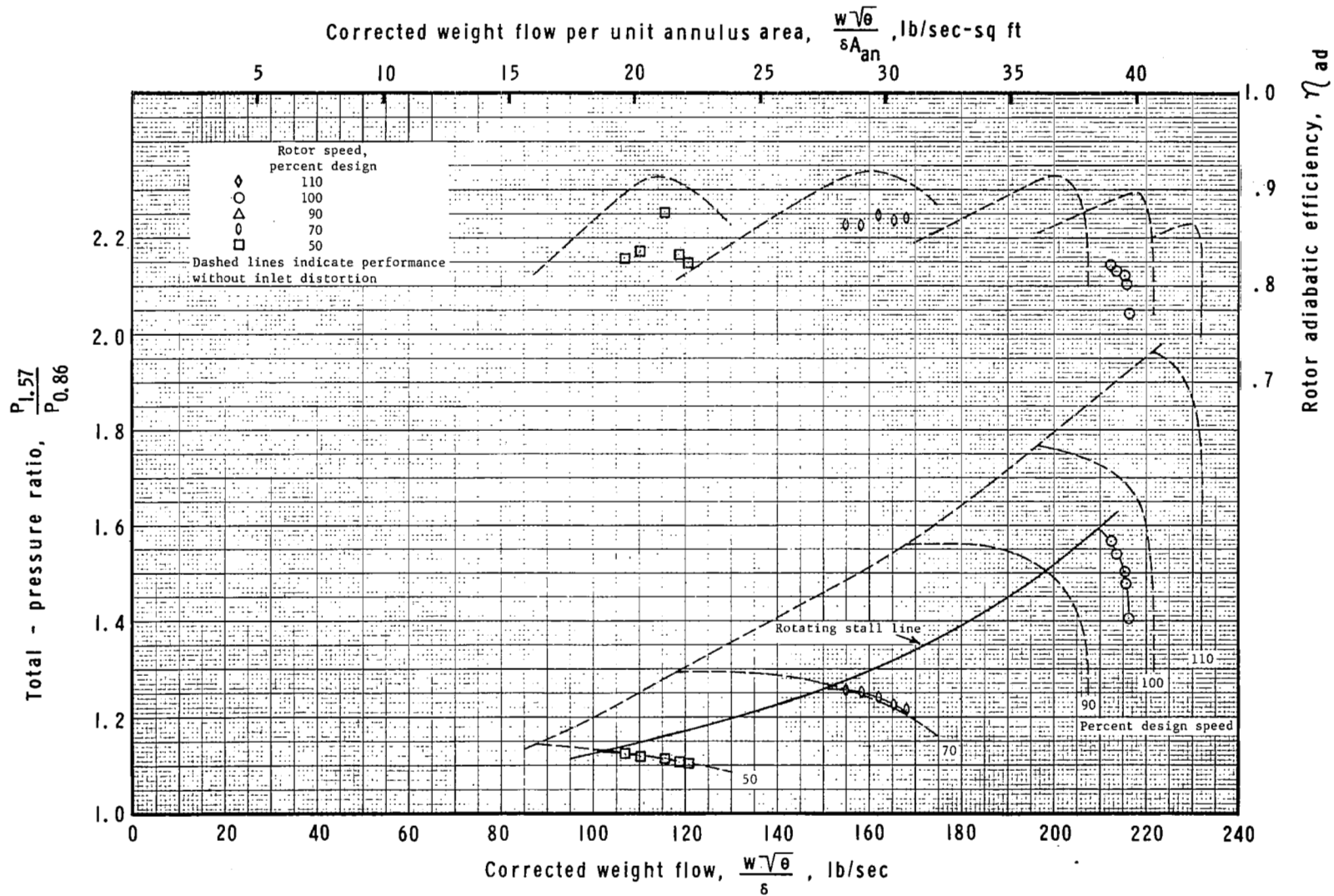
Figure 15(a). – Rotor 1B performance map with radial distortion.

Corrected weight flow per unit annulus area, $\dfrac{w\sqrt{\theta}}{\delta A_{an}}$, lb/sec-sq ft
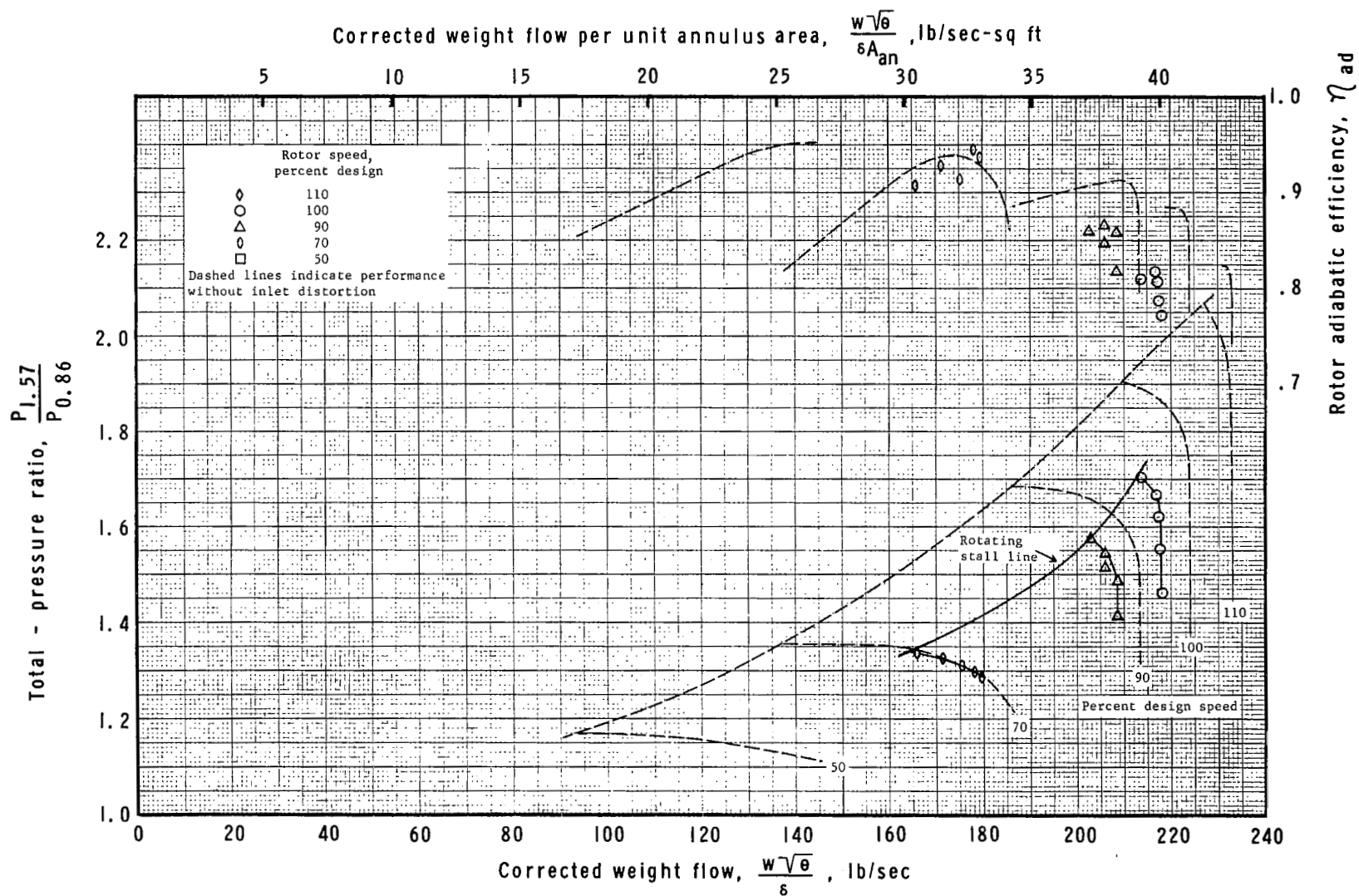
Figure 15(b). – Rotor 2B performance map with radial distortion.
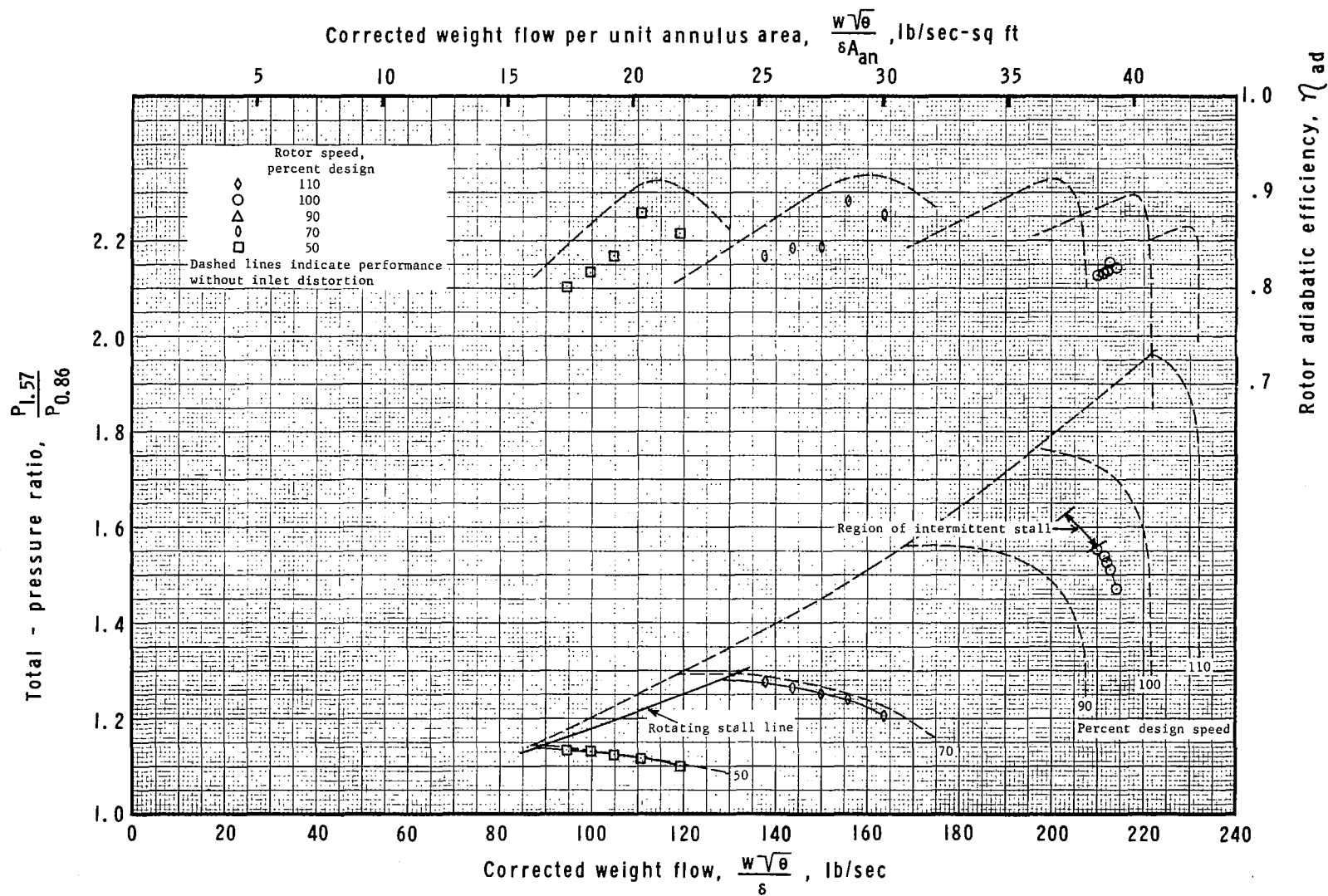
Figure 16(a). - Rotor 1B performance map with circumferential distortion.

Corrected weight flow per unit annulus area, $\dfrac{w\sqrt{\theta}}{\delta A_{an}}$,lb/sec-sq ft

Rotor adiabatic efficiency, η_{ad}

Total - pressure ratio, $\dfrac{P_{1.57}}{P_{0.86}}$
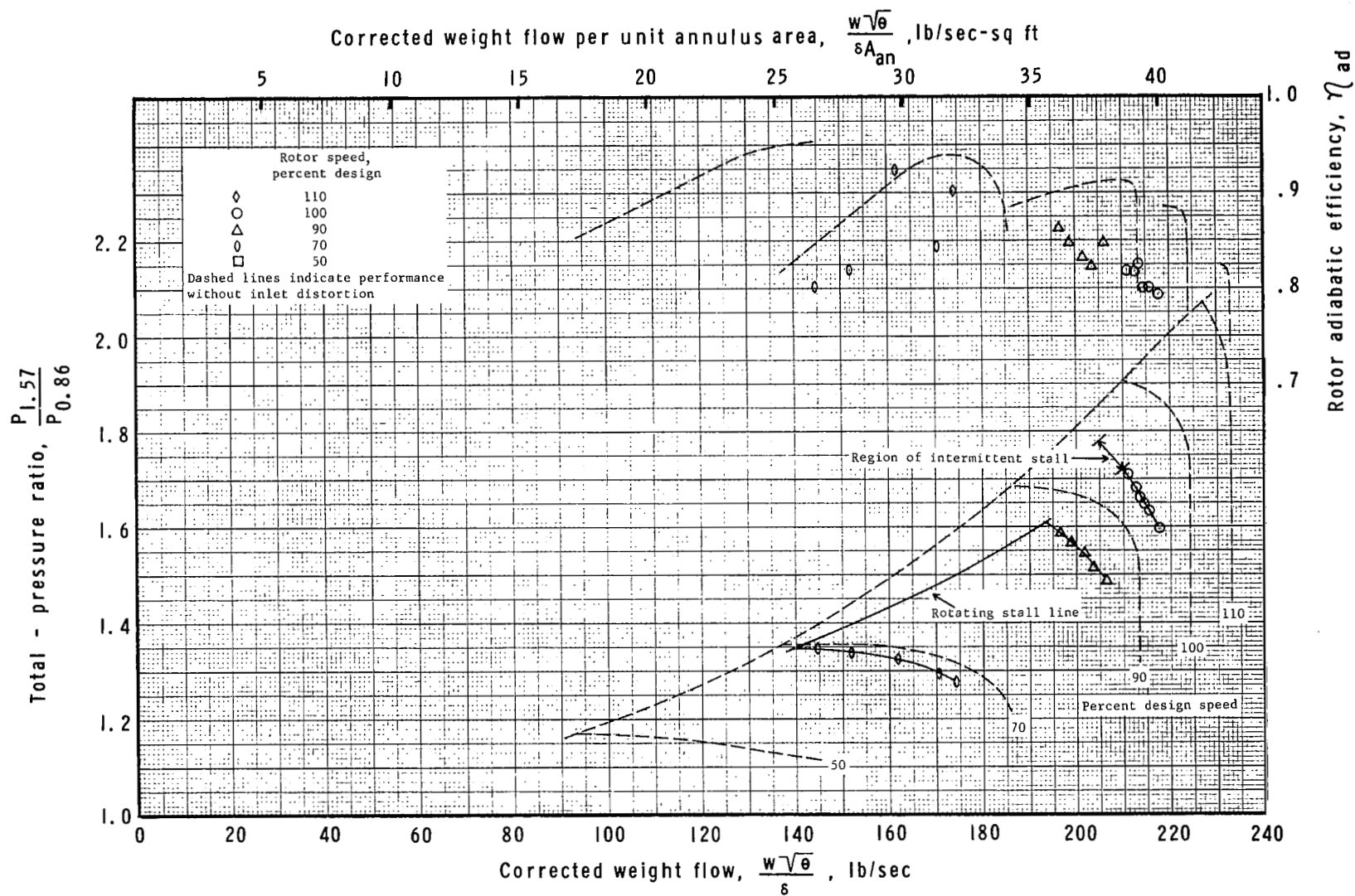
Figure 16(b). - Rotor 2B performance map with circumferential distortion.

Corrected weight flow, $\dfrac{w\sqrt{\theta}}{\delta}$, lb/sec
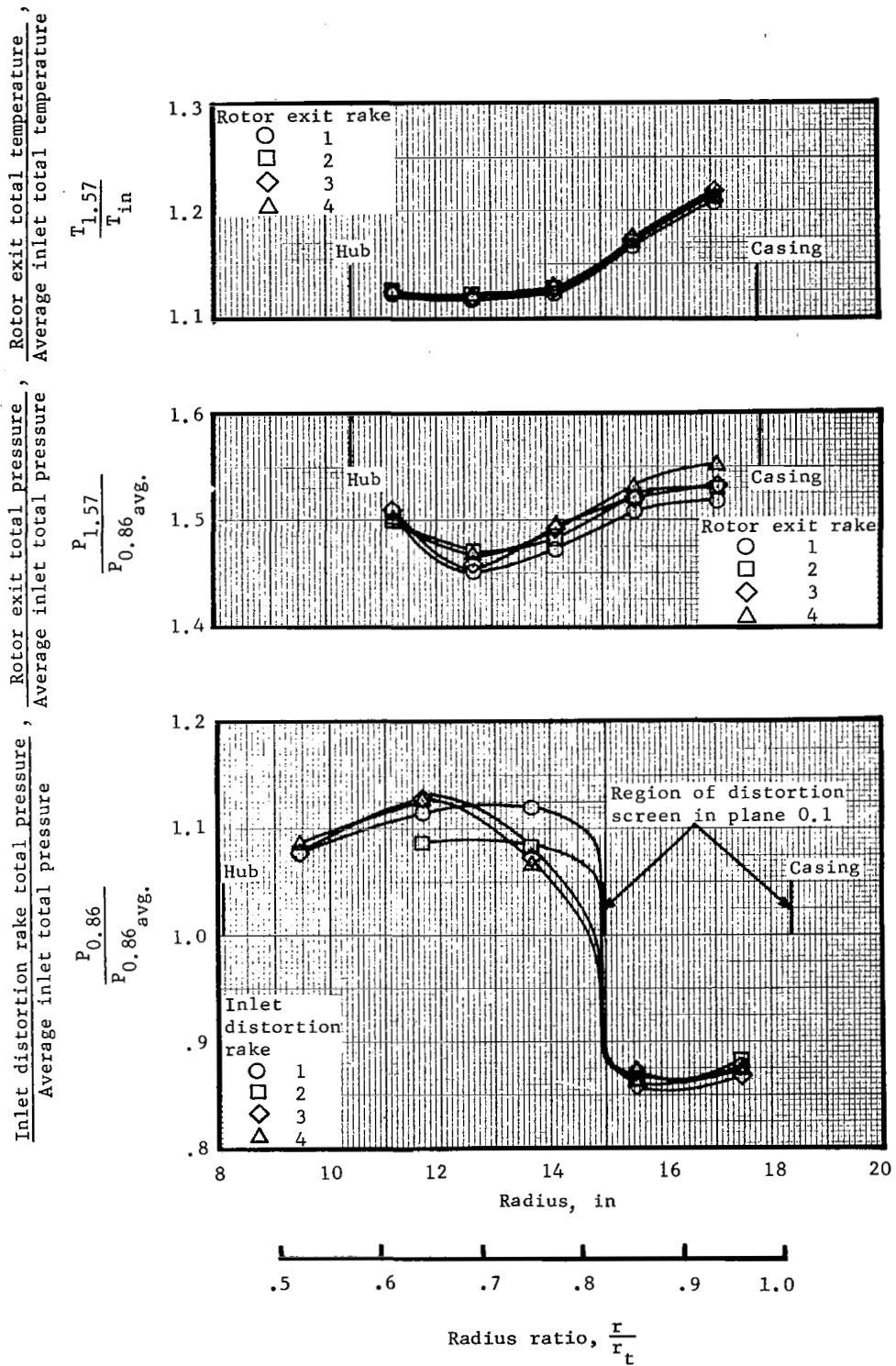
Figure 17(a). - Inlet total pressure, exit total pressure and exit total
temperature profiles obtained from the Rotor 1B radial
distortion testing, for reading 30 at 100% corrected speed.
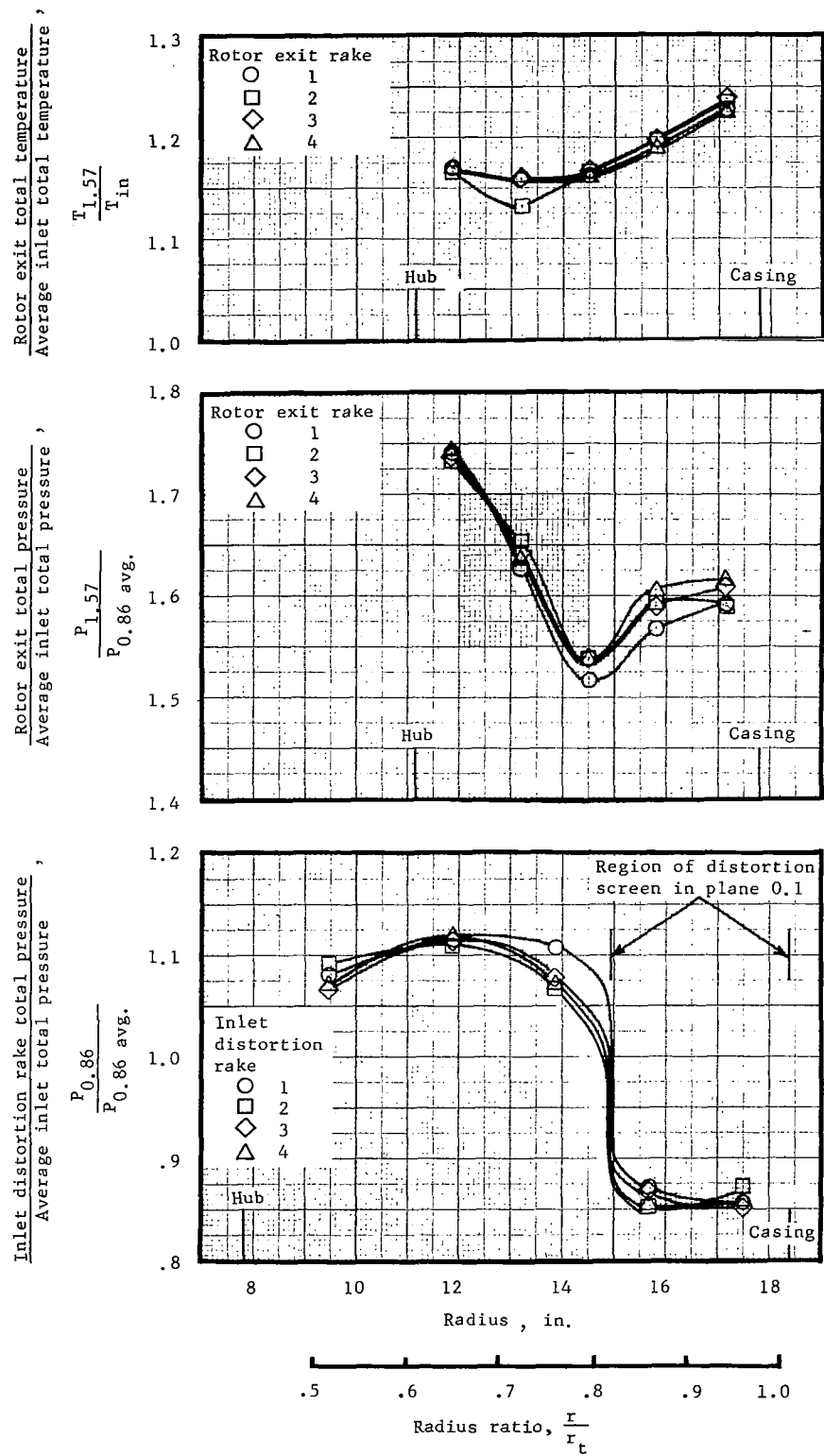
Figure 17(b). – Inlet total pressure, exit total pressure and exit total
temperature profiles obtained from the Rotor 2B radial
distortion testing, for reading 85 at 100% corrected speed.
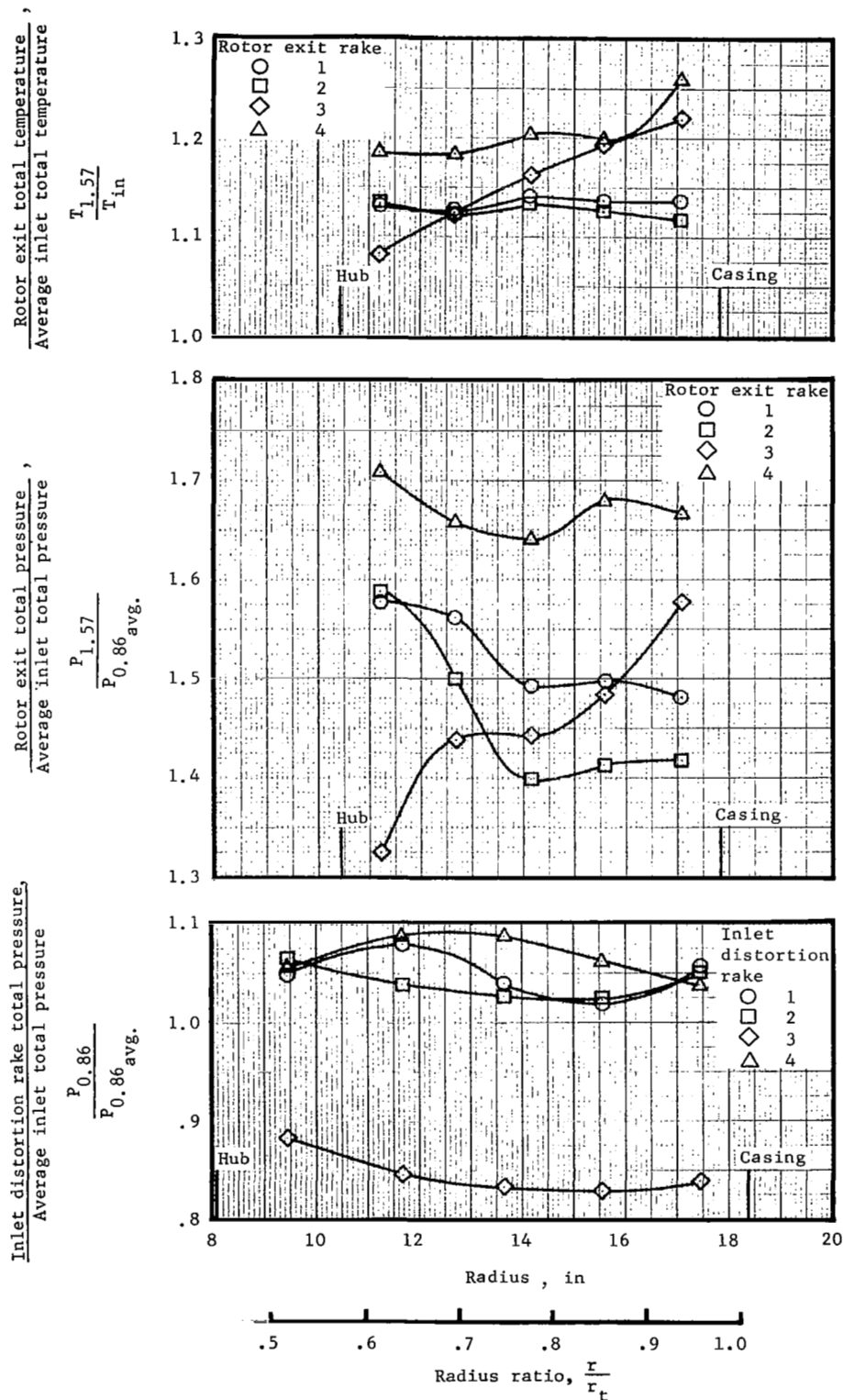
Figure 18(a). – Inlet total pressure, exit total pressure and exit total temperature profiles obtained from the Rotor 1B circumferential distortion testing, for reading 46 at 100% corrected speed.
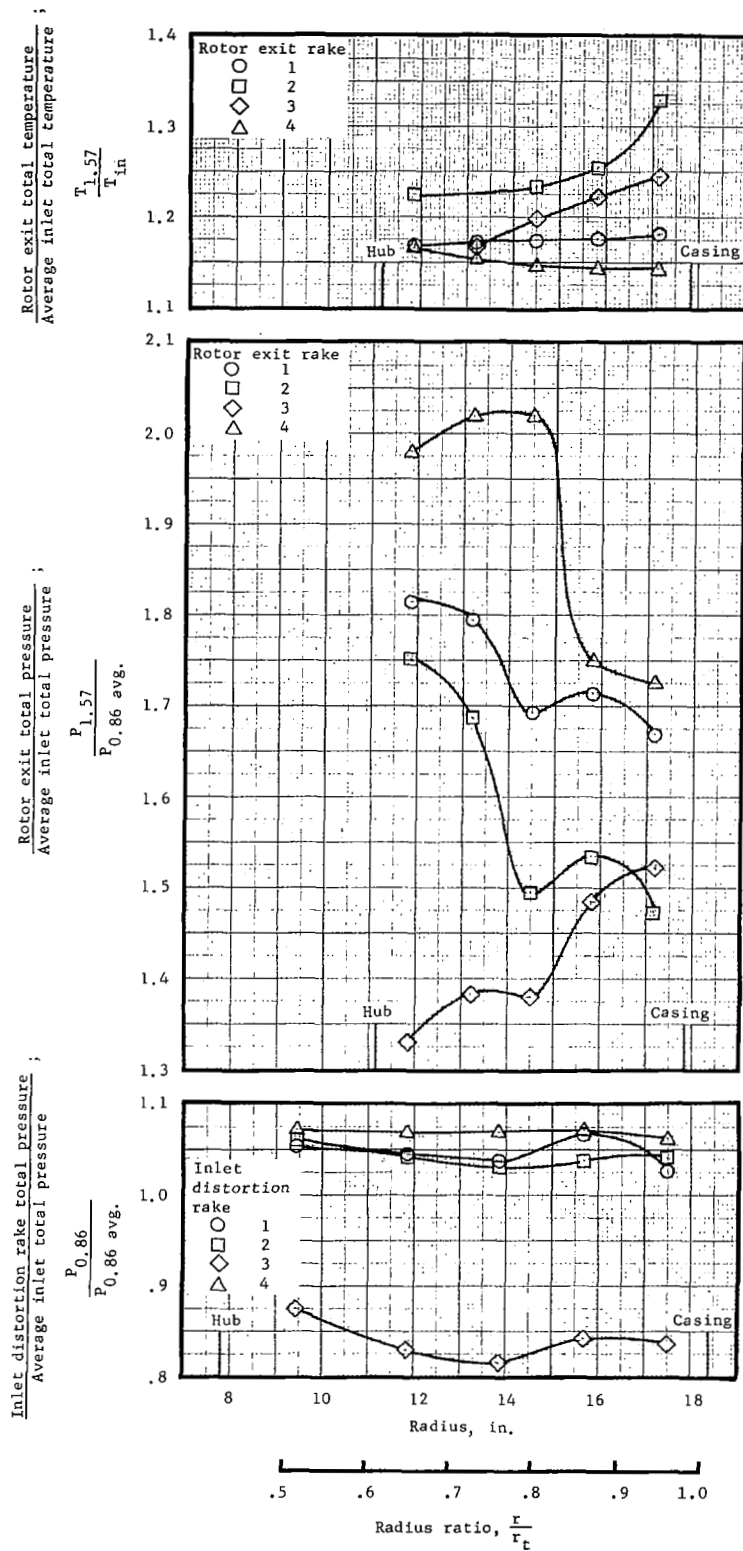
Figure 18(b). – Inlet total pressure, exit total pressure and exit total temperature profiles obtained from the Rotor 2B circumferential distortion testing, for reading 101 at 100% corrected speed.
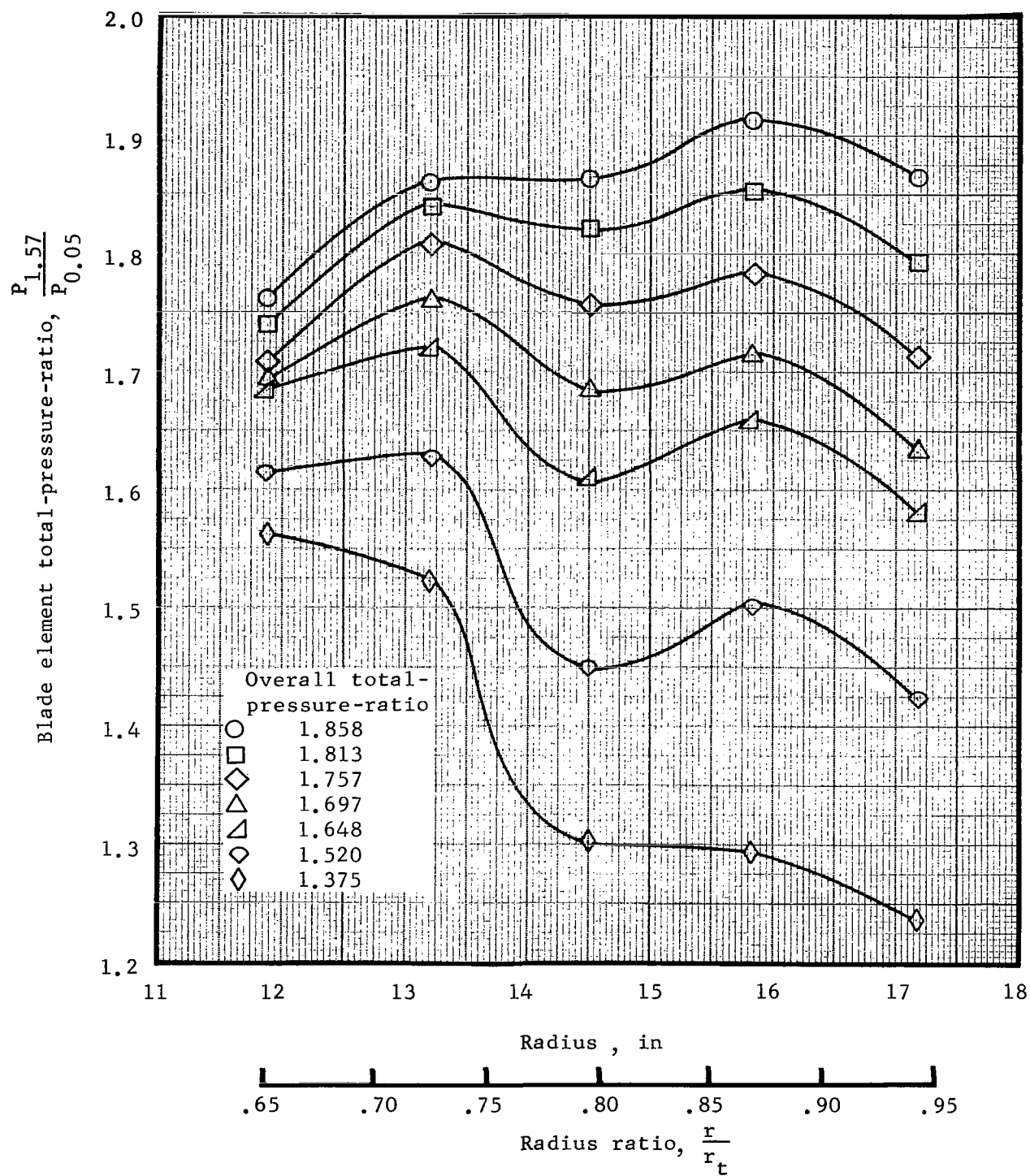
Figure 19. - Spanwise variation of element total-pressure-ratio for Rotor 2B along the design speed line.
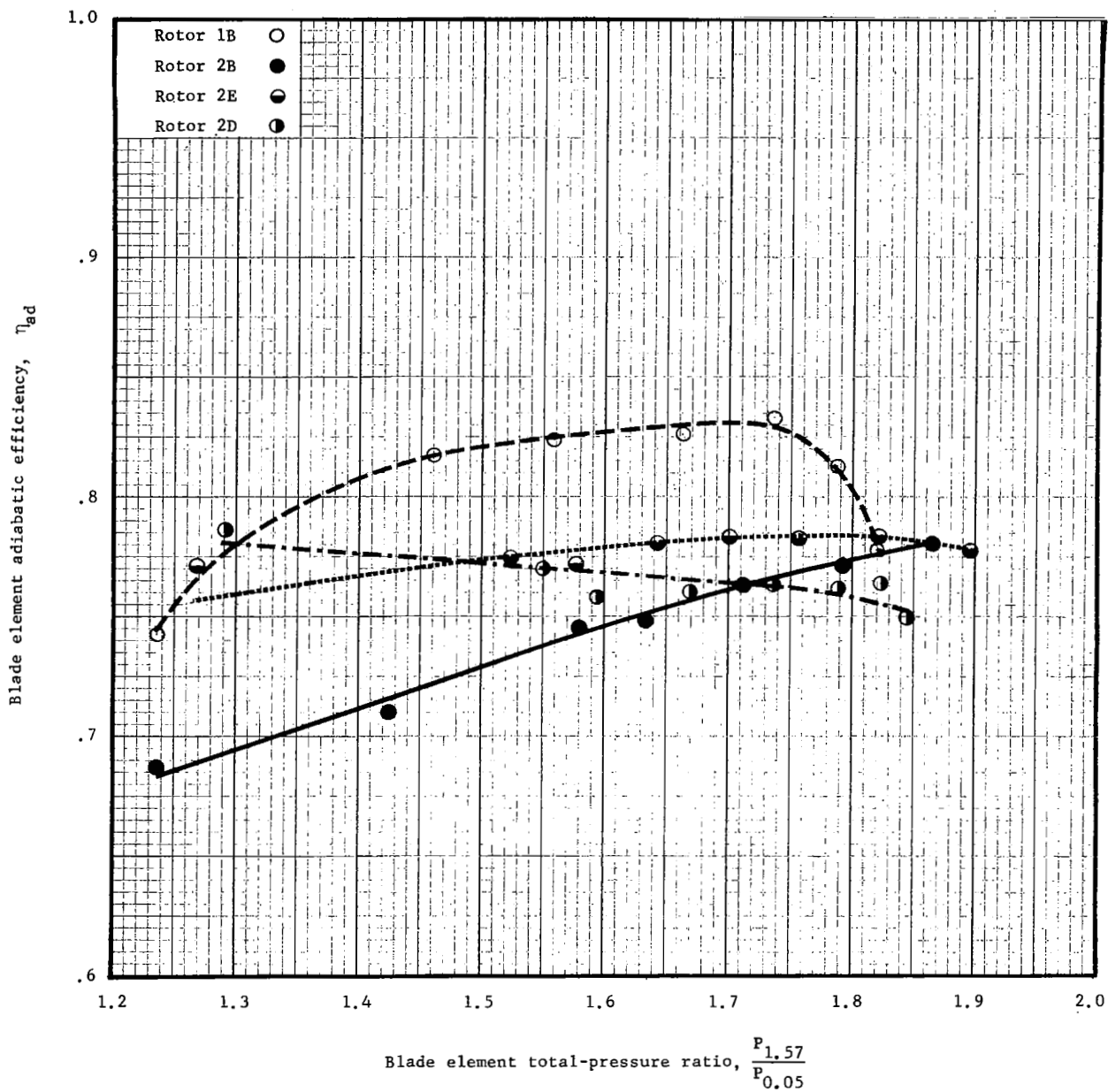
Figure 20(a). – Element efficiency as a function of total-pressure-ratio at 10% immersion from tip at design speed.
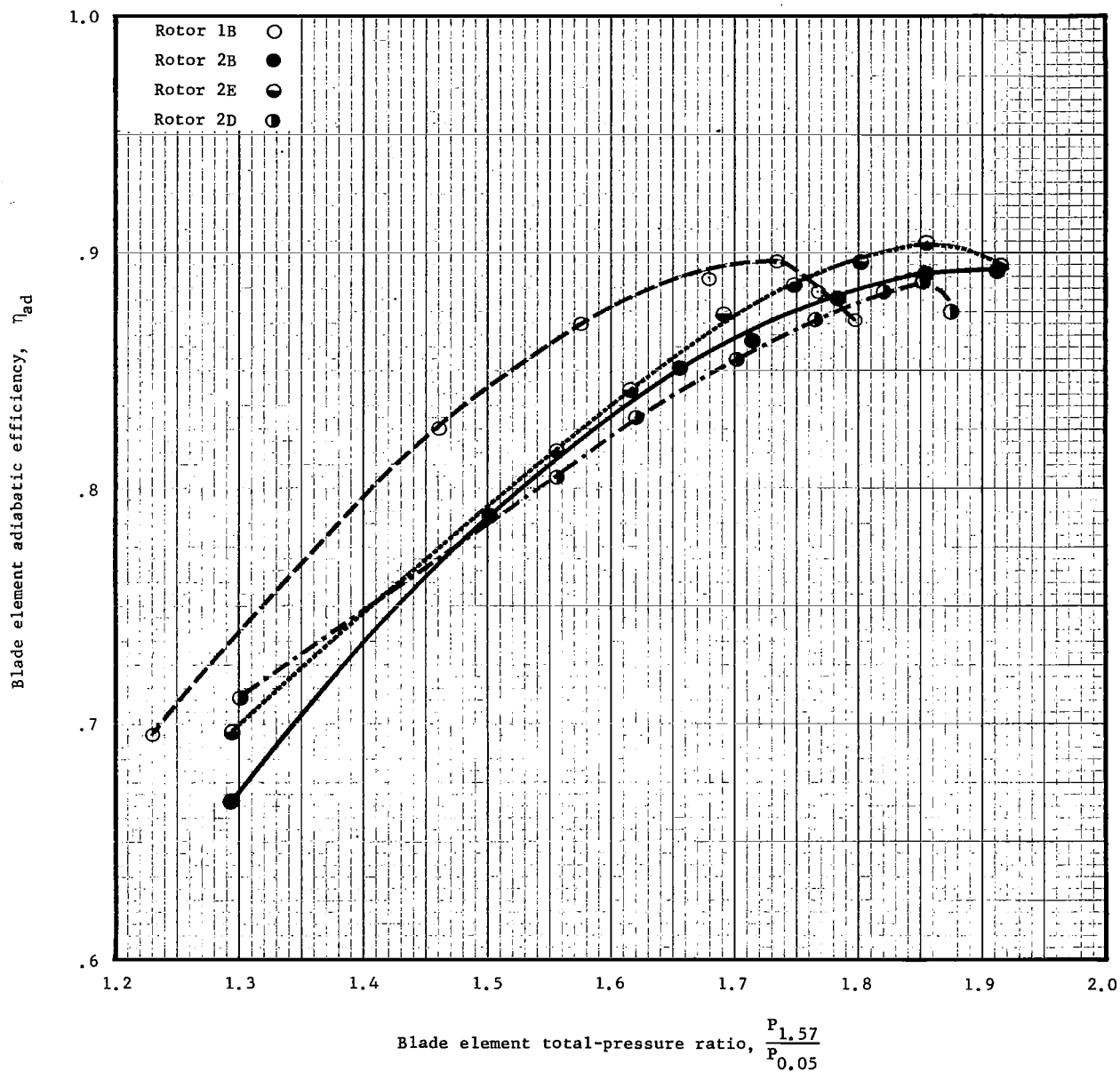
Figure 20(b). – Element efficiency as a function of total-pressure-ratio at 30% immersion from tip at design speed.
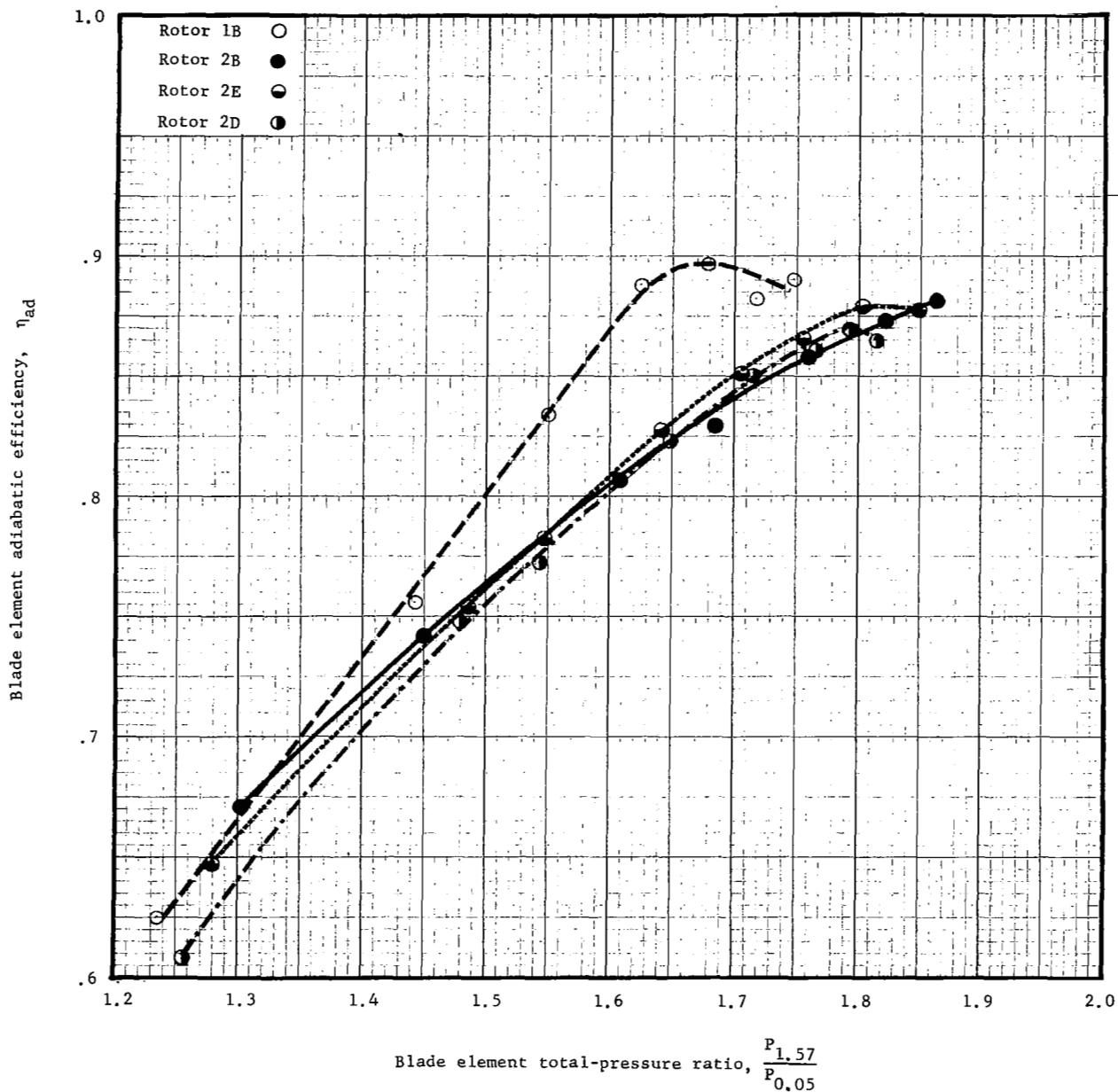
Figure 20(c). - Element efficiency as a function of total-pressure-ratio at 50% immersion from tip at design speed.
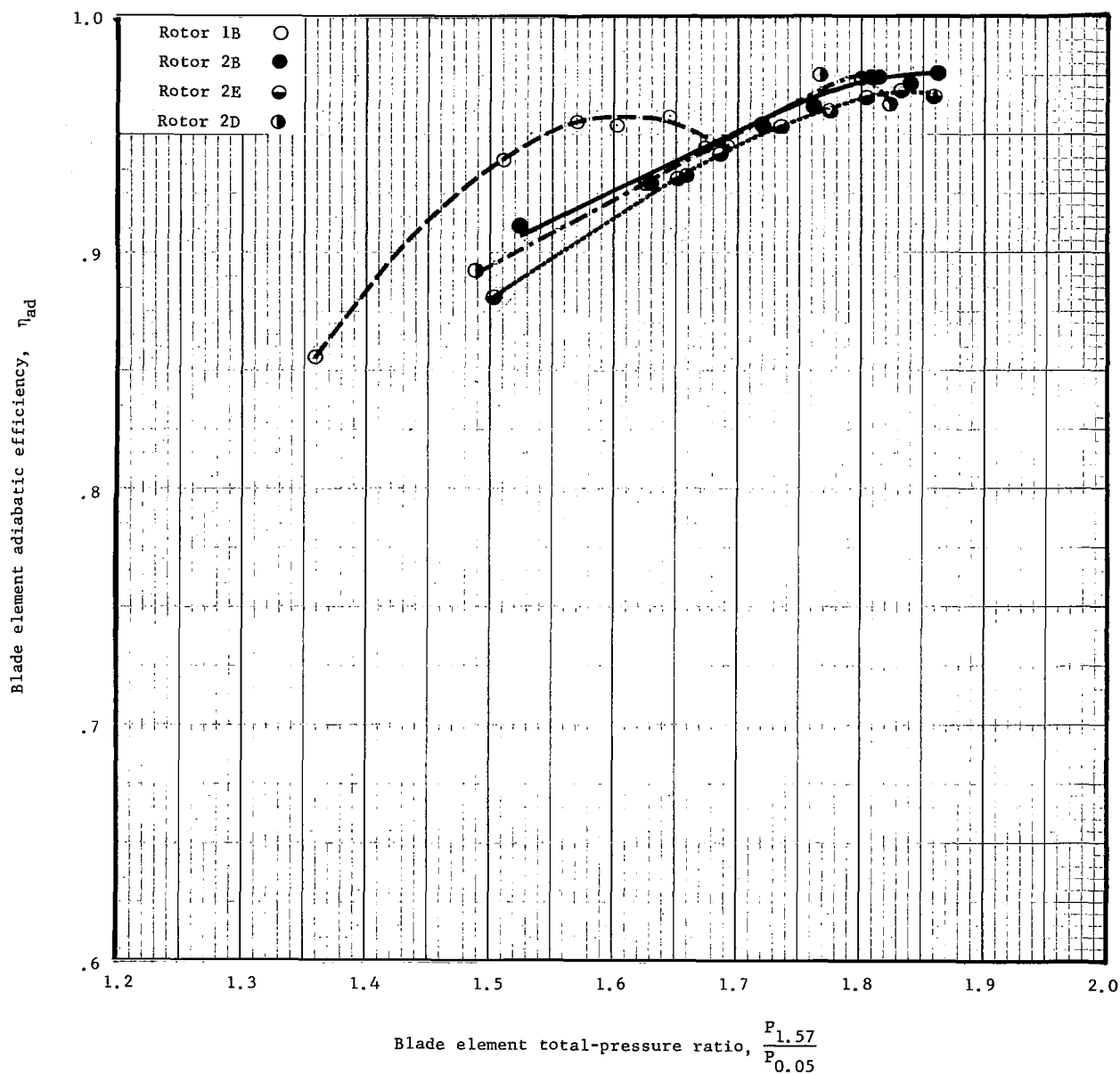
Figure 20(d). - Element efficiency as a function of total-pressure-ratio at 70% immersion from tip at design speed.
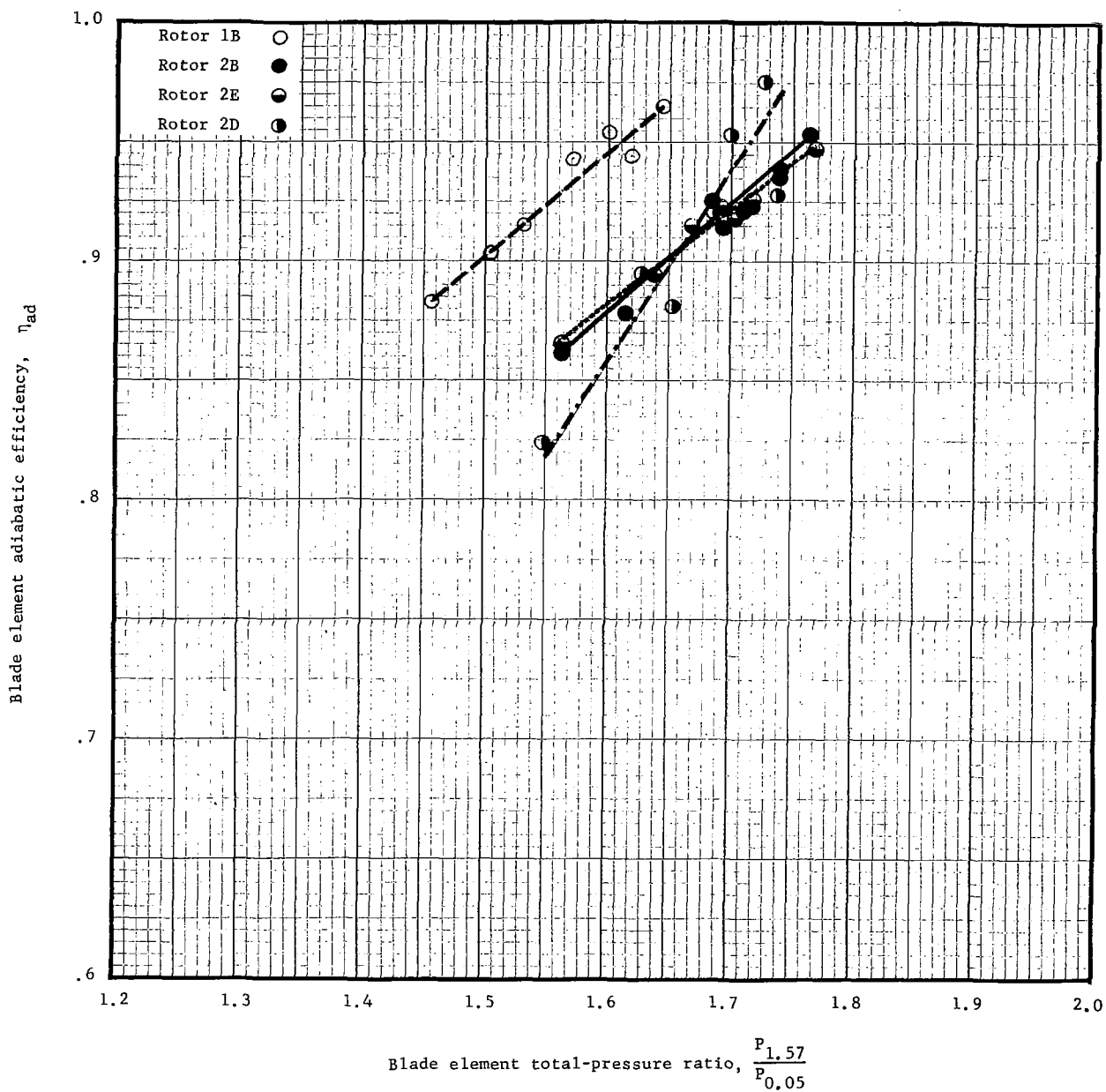
Figure 20(e). – Element efficiency as a function of total-pressure-ratio at 90% immersion from tip at design speed.
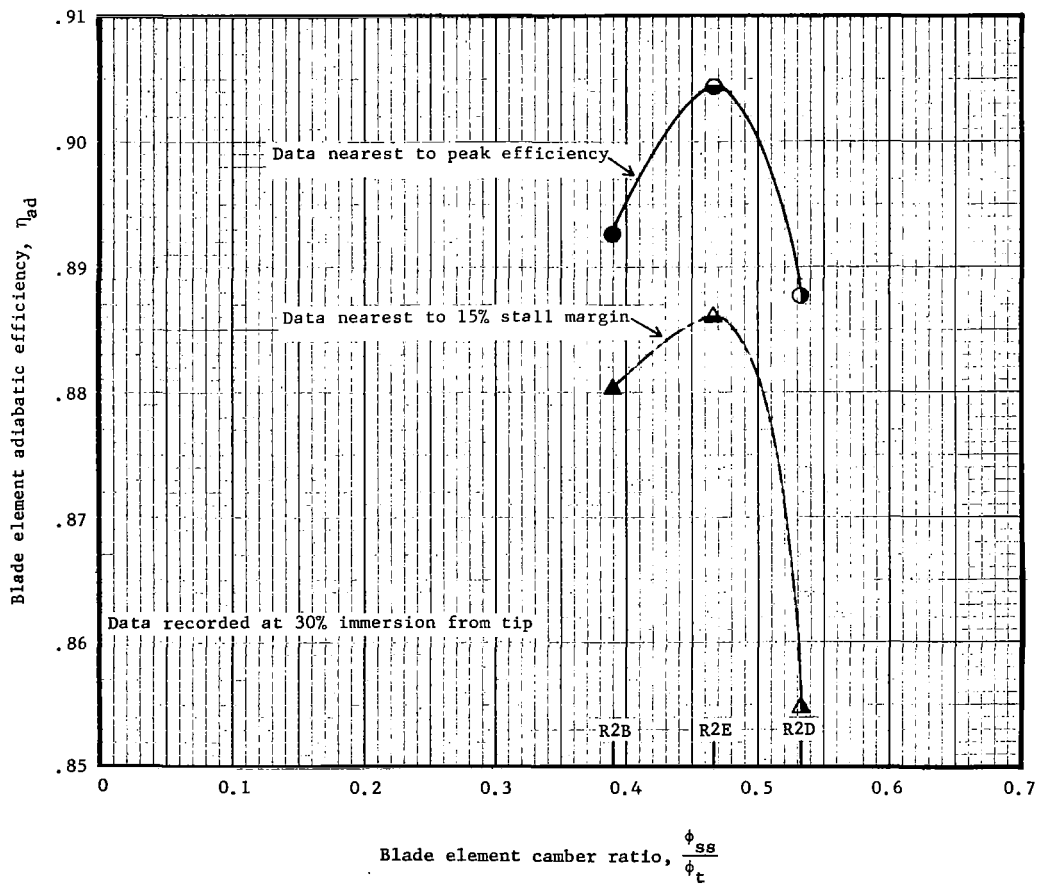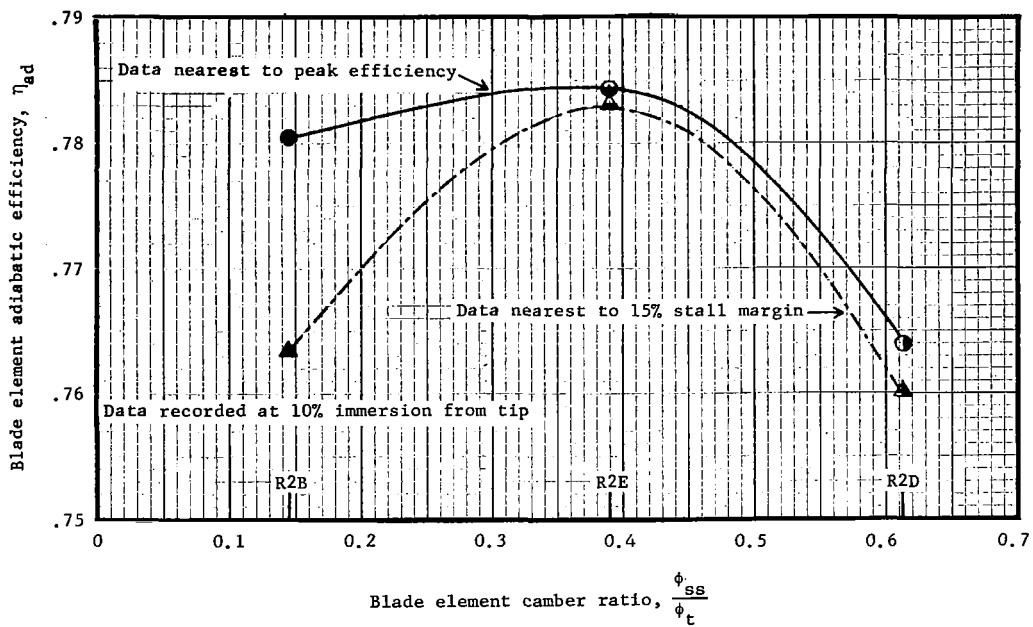
Figure 21. - Element efficiency as a function of local camber ratio at 10% and 30% immersions at design speed.
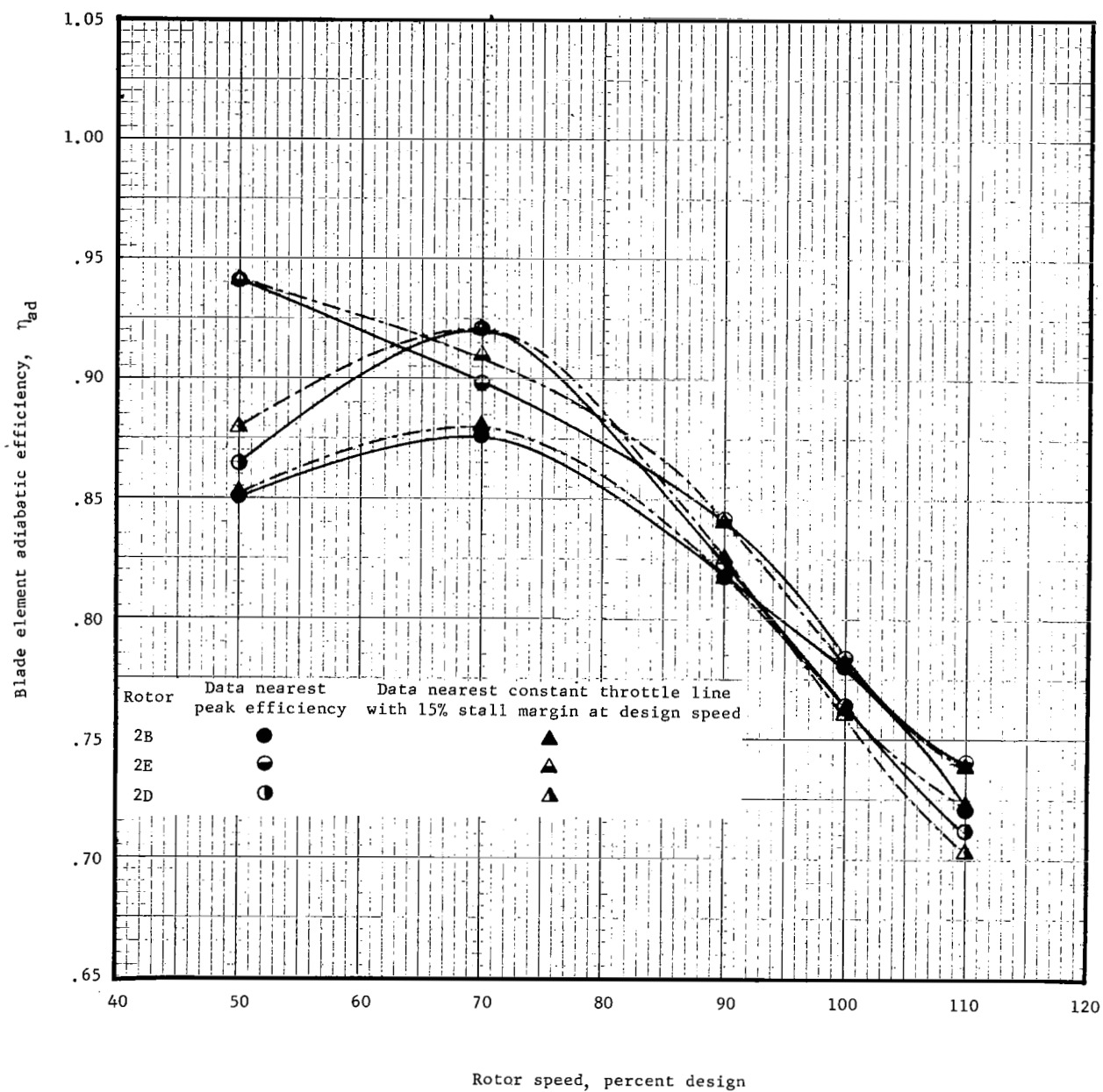
Figure 22(a). - Element efficiency as a function of percent speed at 10% immersion from tip.
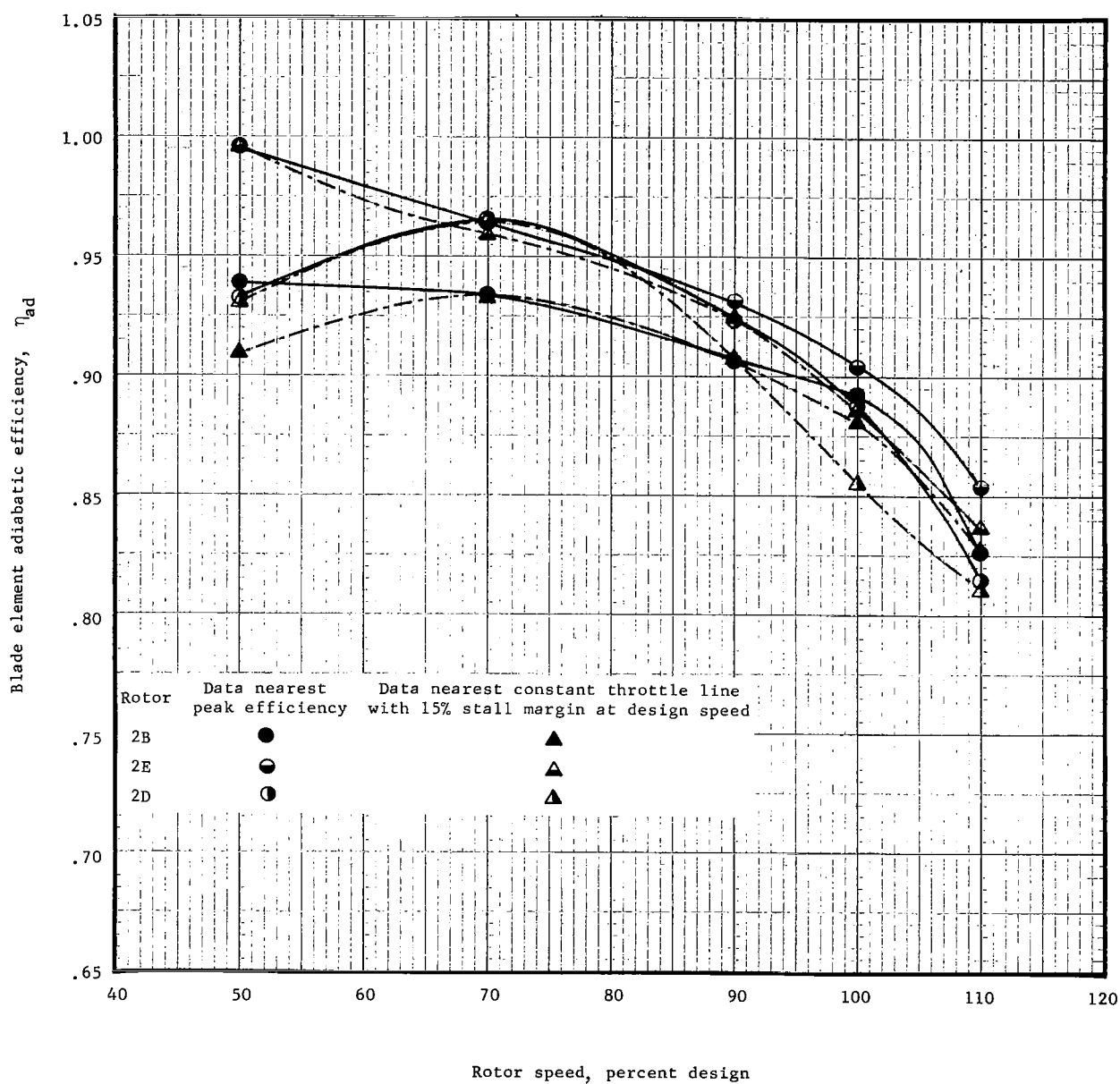
Figure 22(b). — Element efficiency as a function of percent speed at 30% immersion from tip.
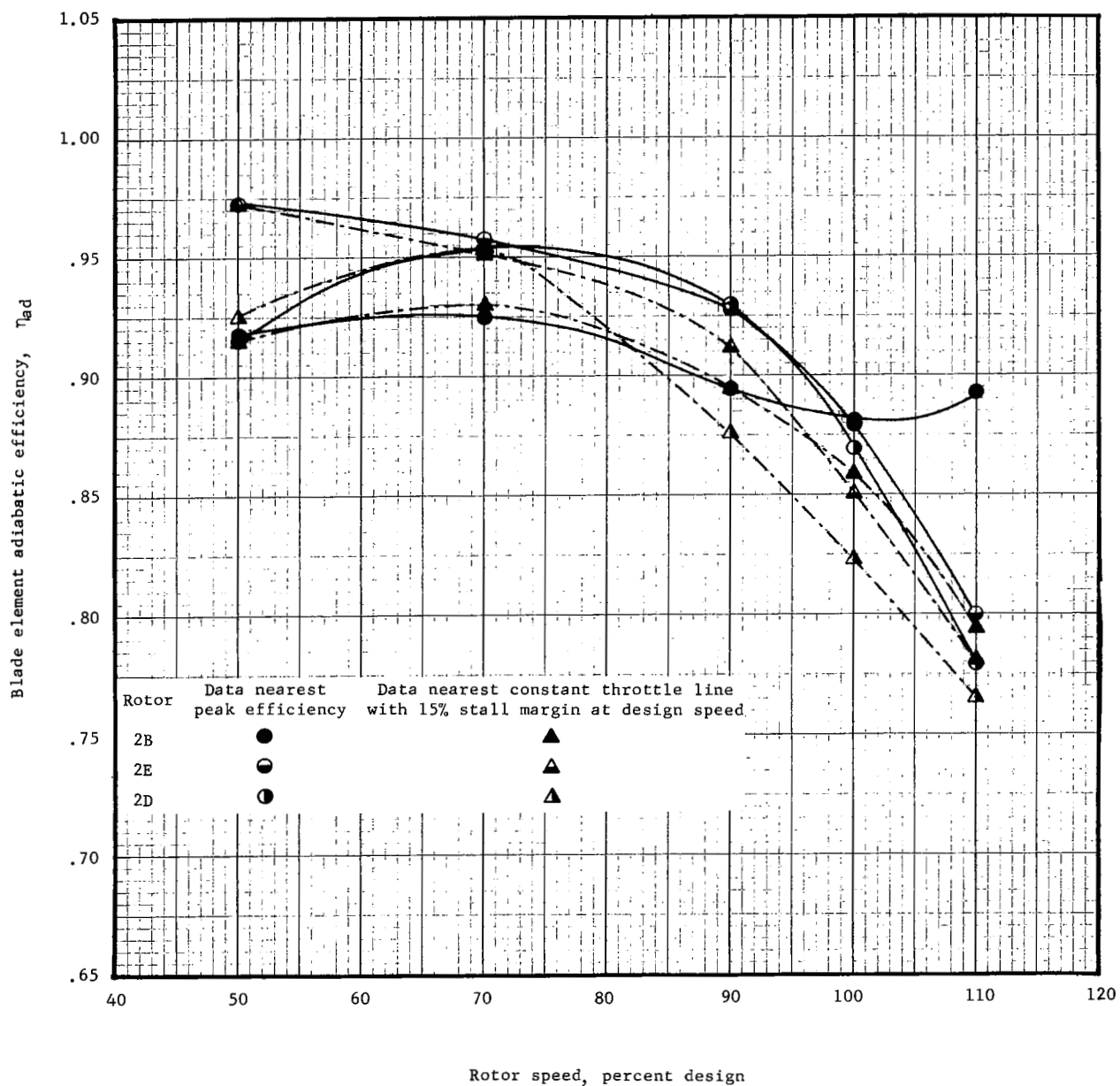
Figure 22(c). – Element efficiency as a function of percent speed at 50% immersion from tip.
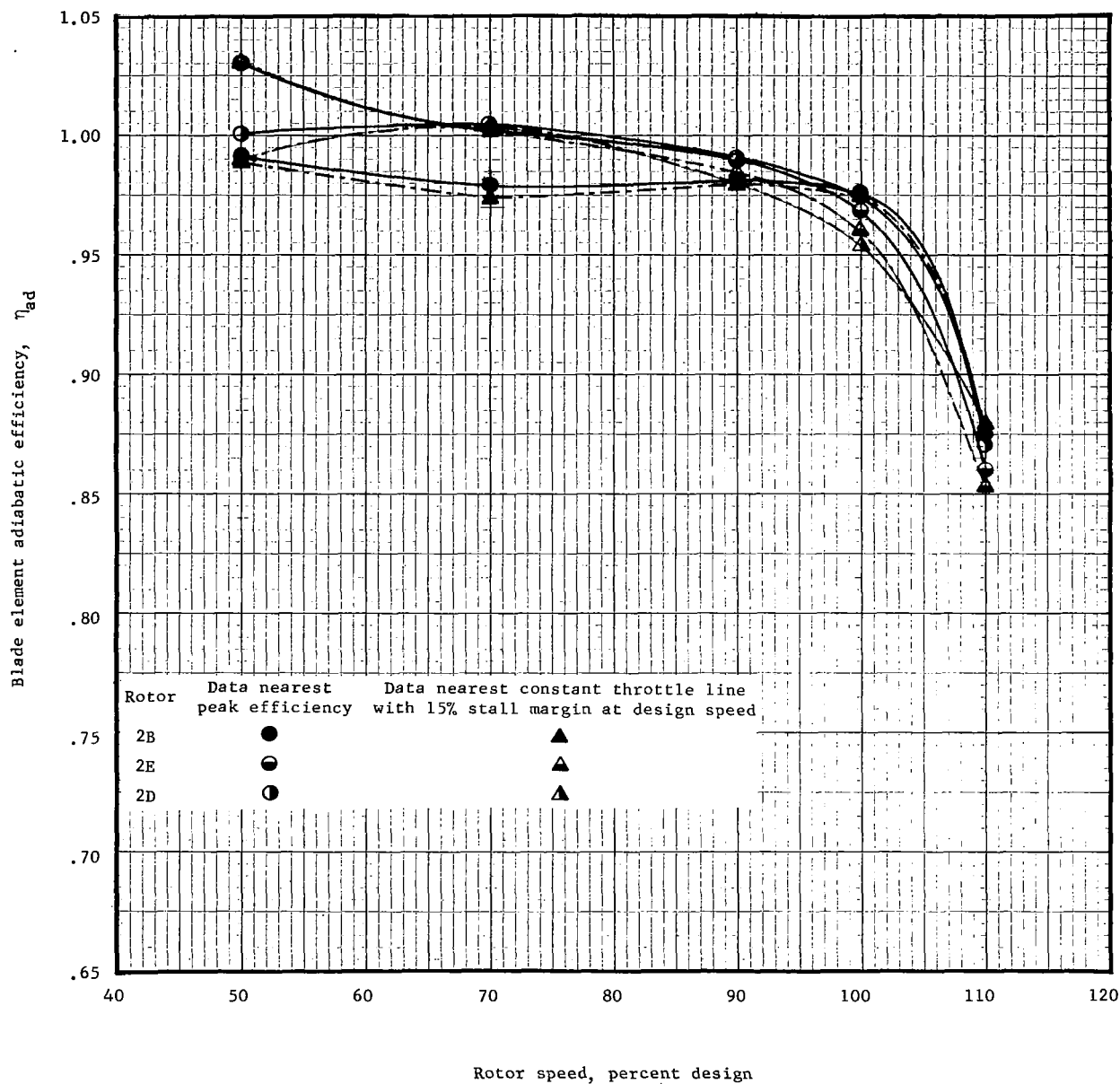
Figure 22(d). – Element efficiency as a function of percent speed at 70% immersion from tip.
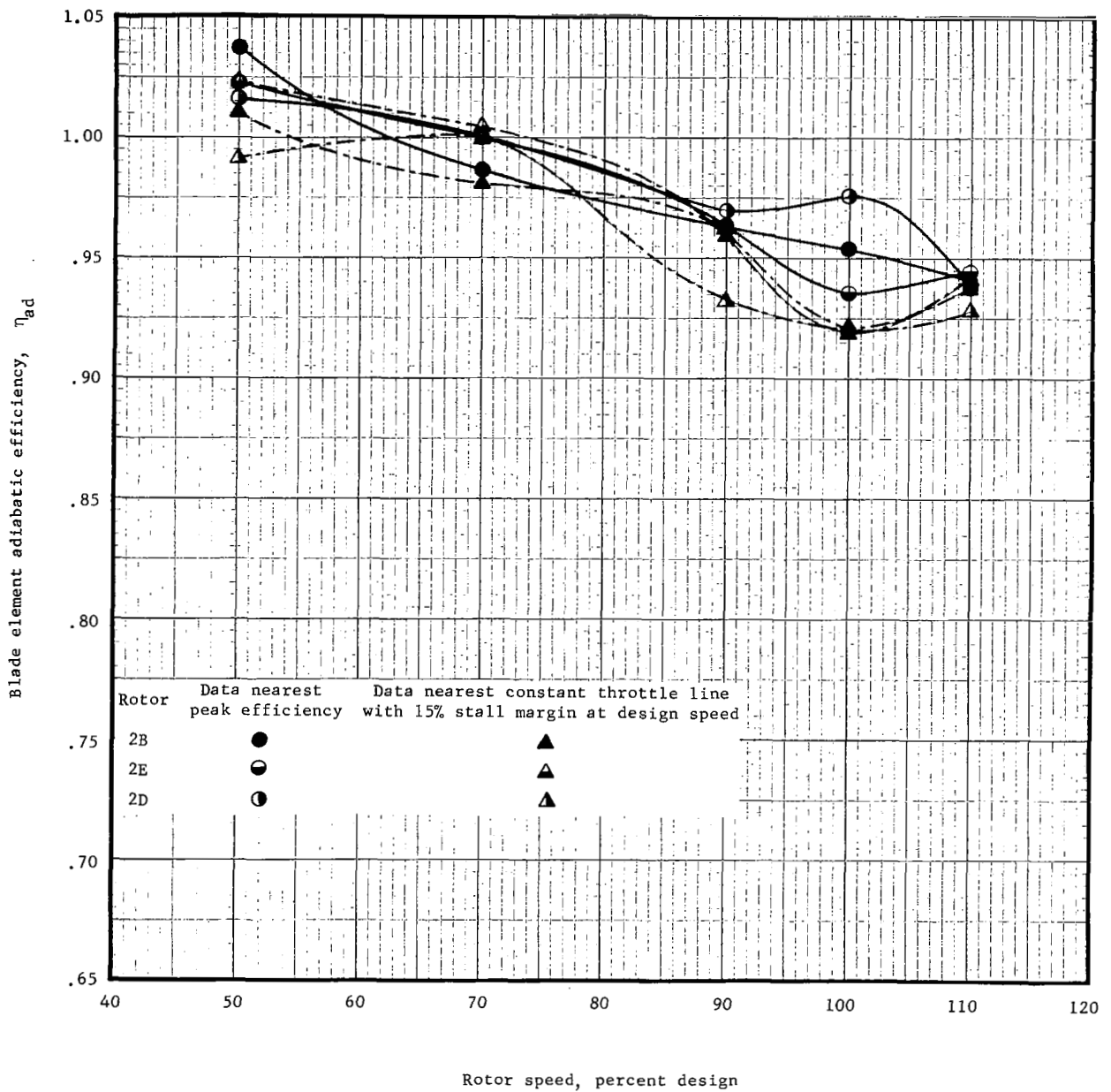
Figure 22(e). – Element efficiency as a function of percent speed at 90% immersion from tip.

Rotor speed, percent design
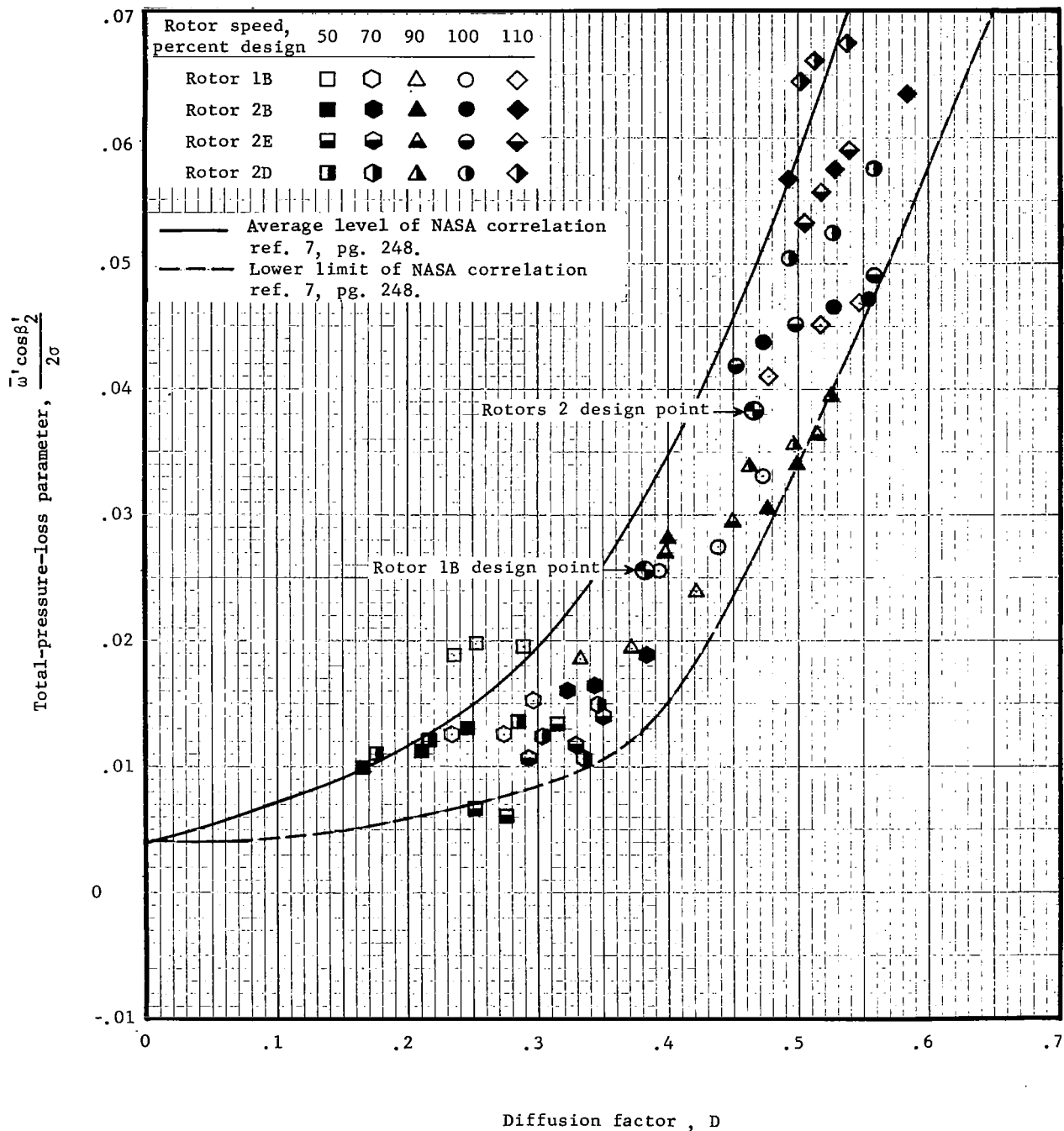
Figure 23(a). – Total-pressure-loss parameter as a function of diffusion factor at 10% immersion from tip.

67
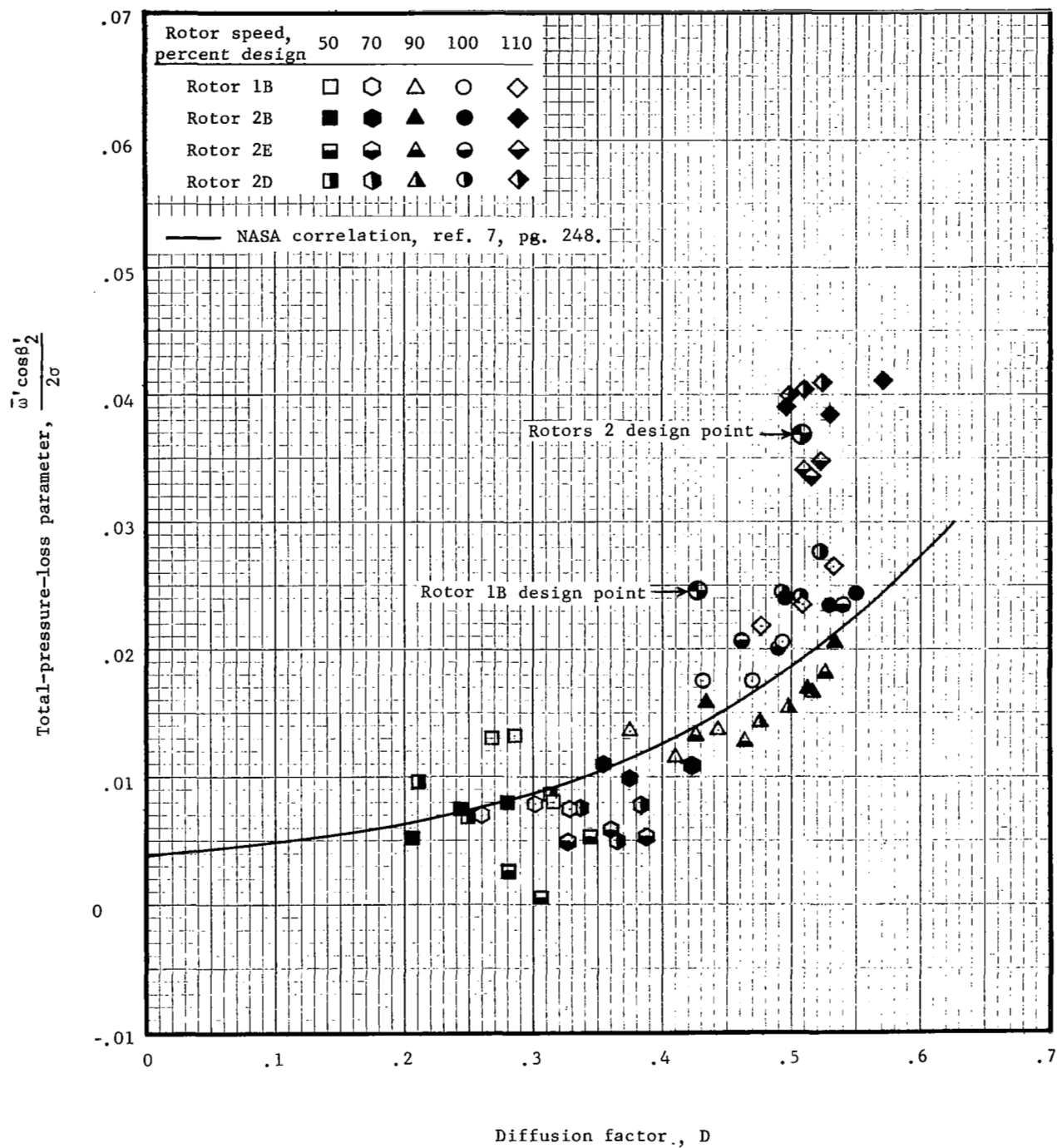
Figure 23(b). – Total-pressure-loss parameter as a function of diffusion factor at 30% immersion from tip.
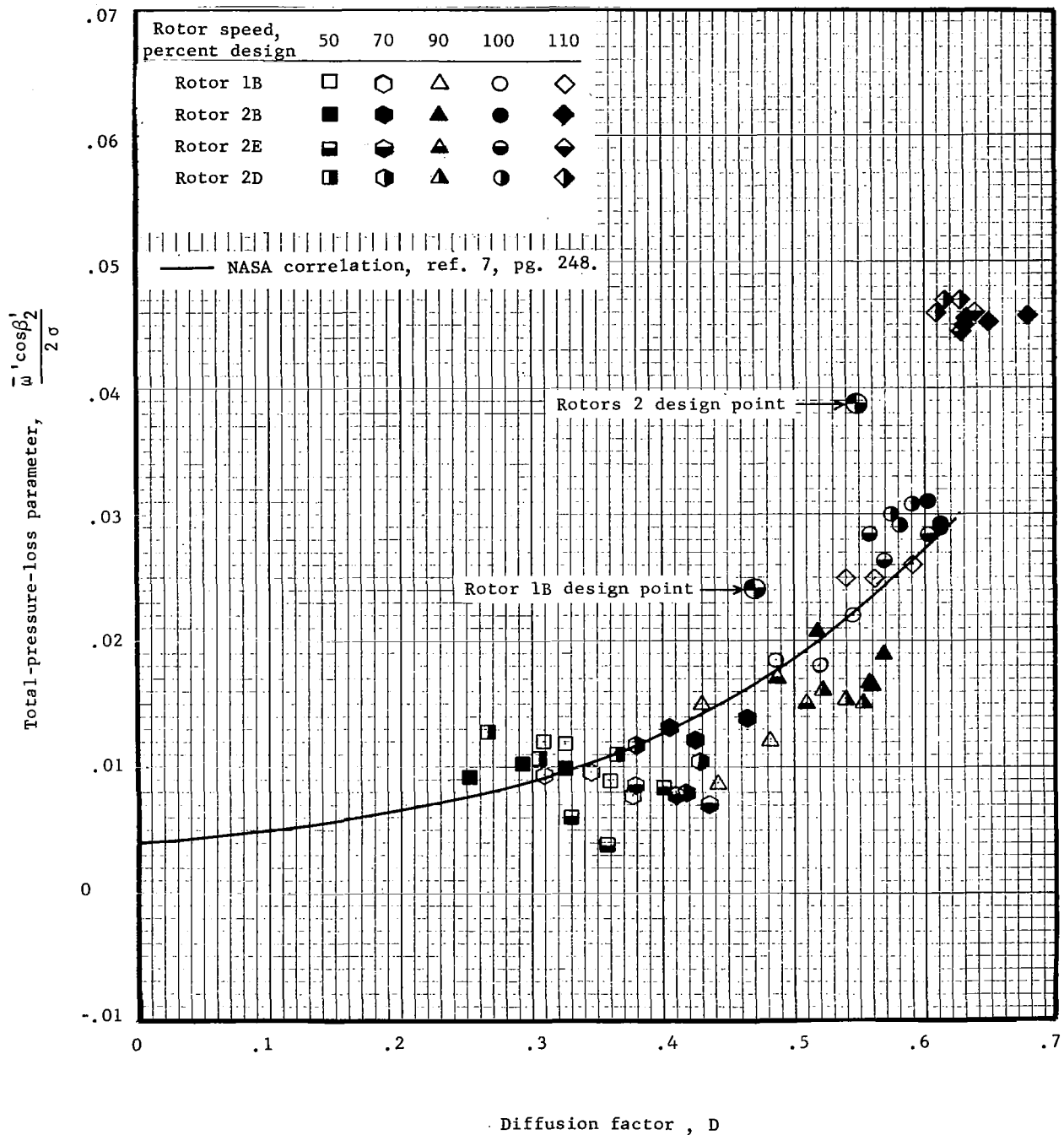
Figure 23(c). – Total-pressure-loss parameter as a function of diffusion factor at 50% immersion from tip.
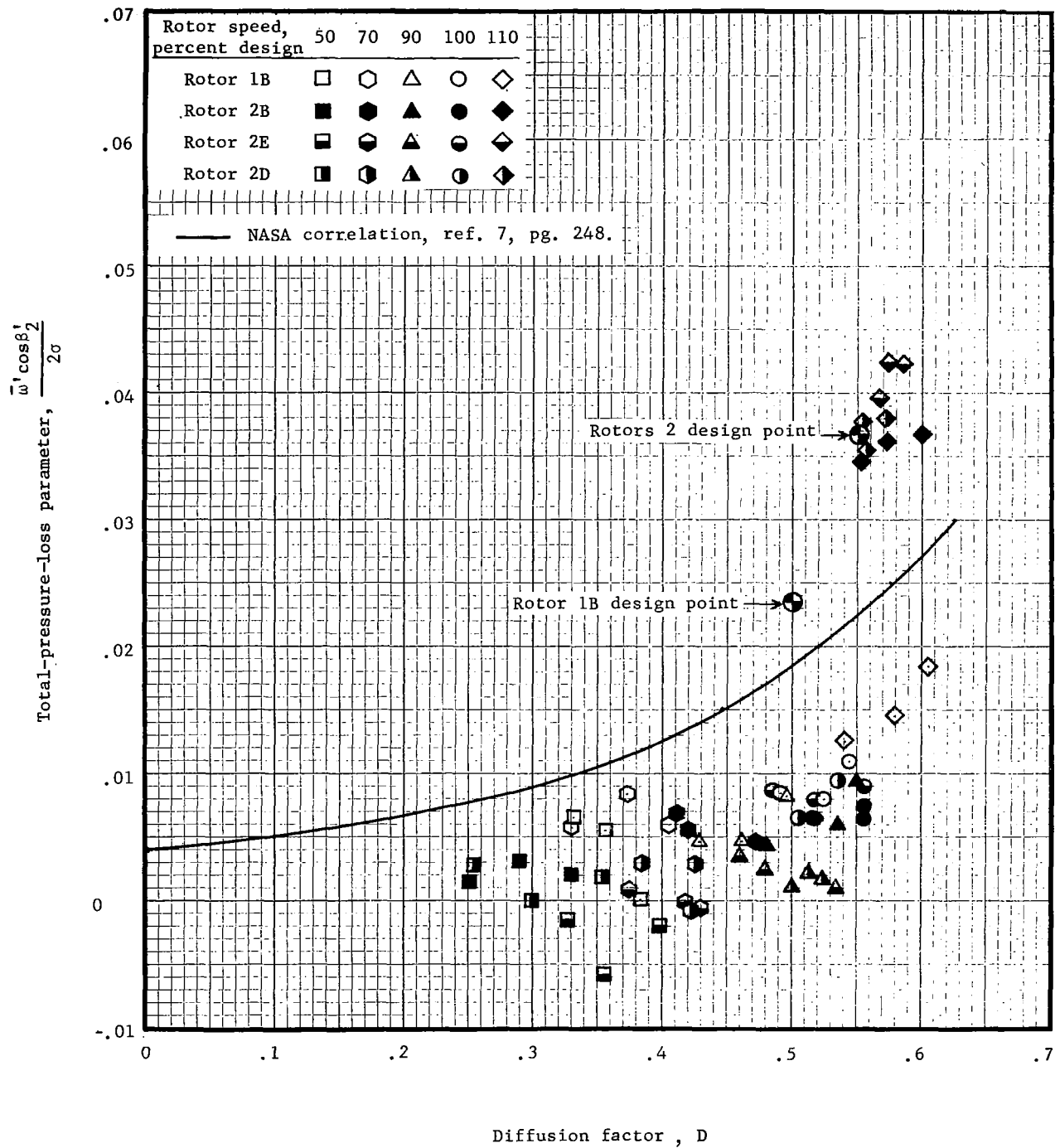
Figure 23(d). – Total-pressure-loss parameter as a function of diffusion factor at 70% immersion from tip.
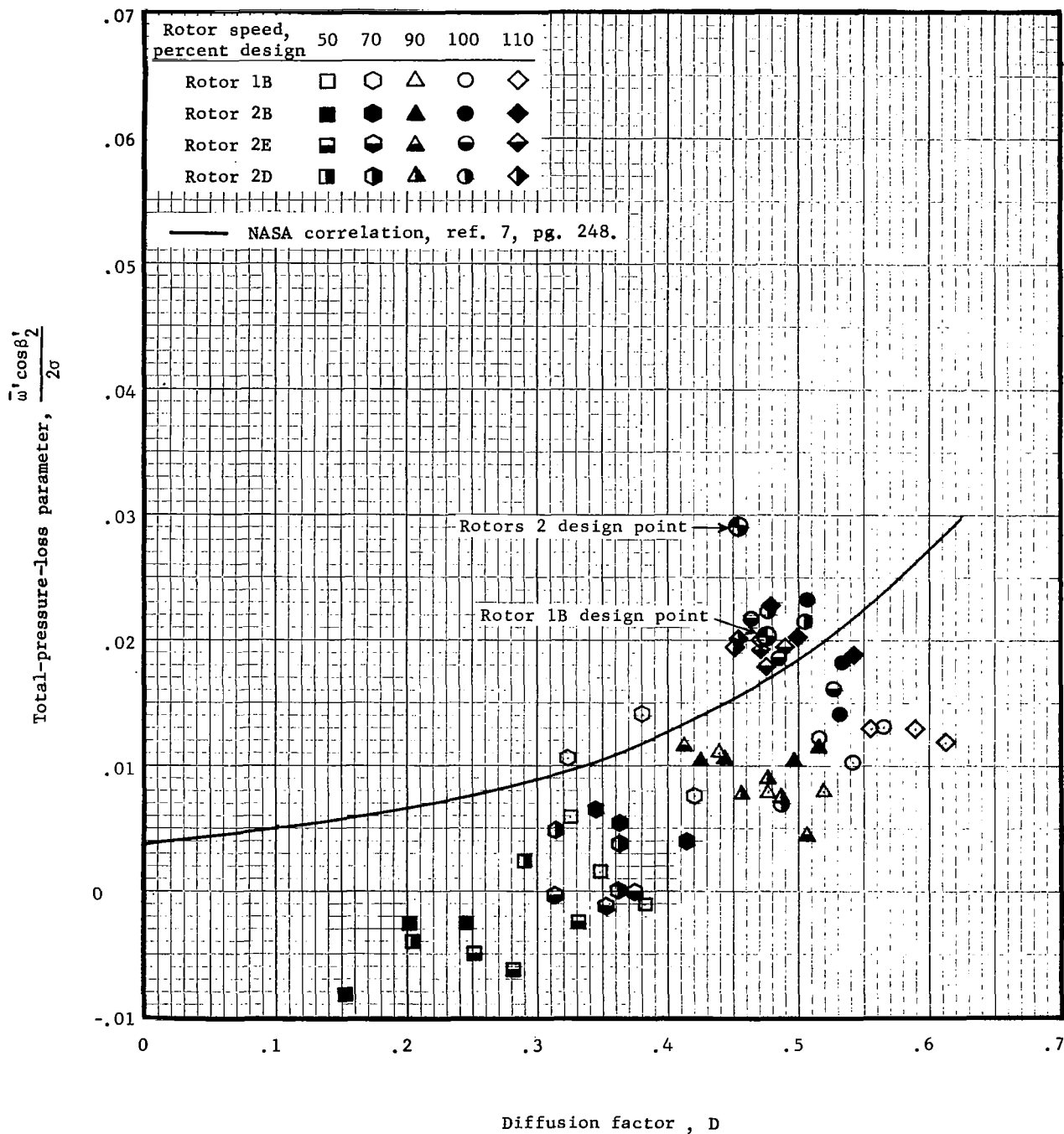
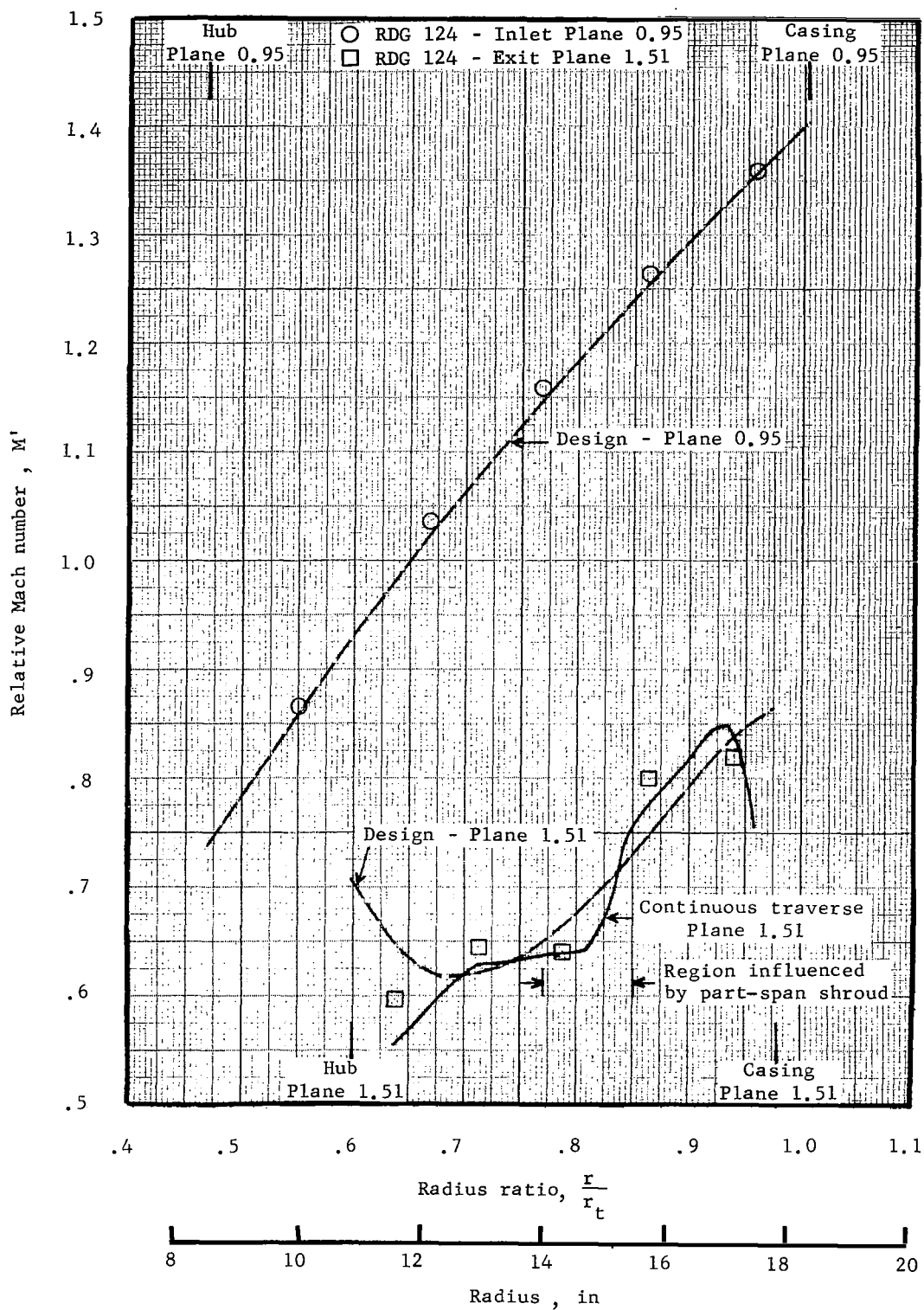Figure 23(e). – Total-pressure-loss parameter as a function of diffusion factor at 90% immersion from tip.
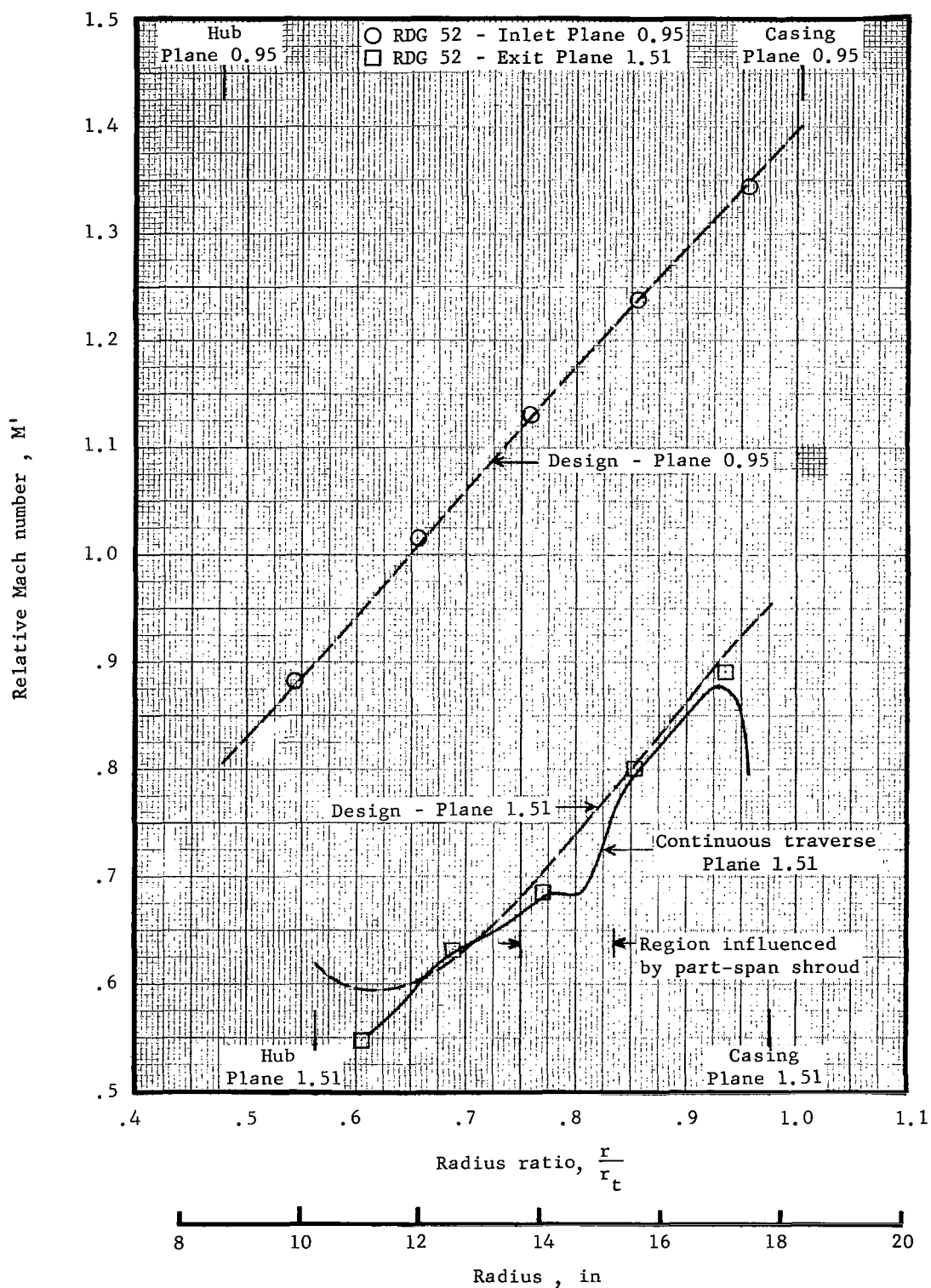
Figure 24. – Radial distributions of inlet and discharge relative Mach number for Rotor 1B at design speed.
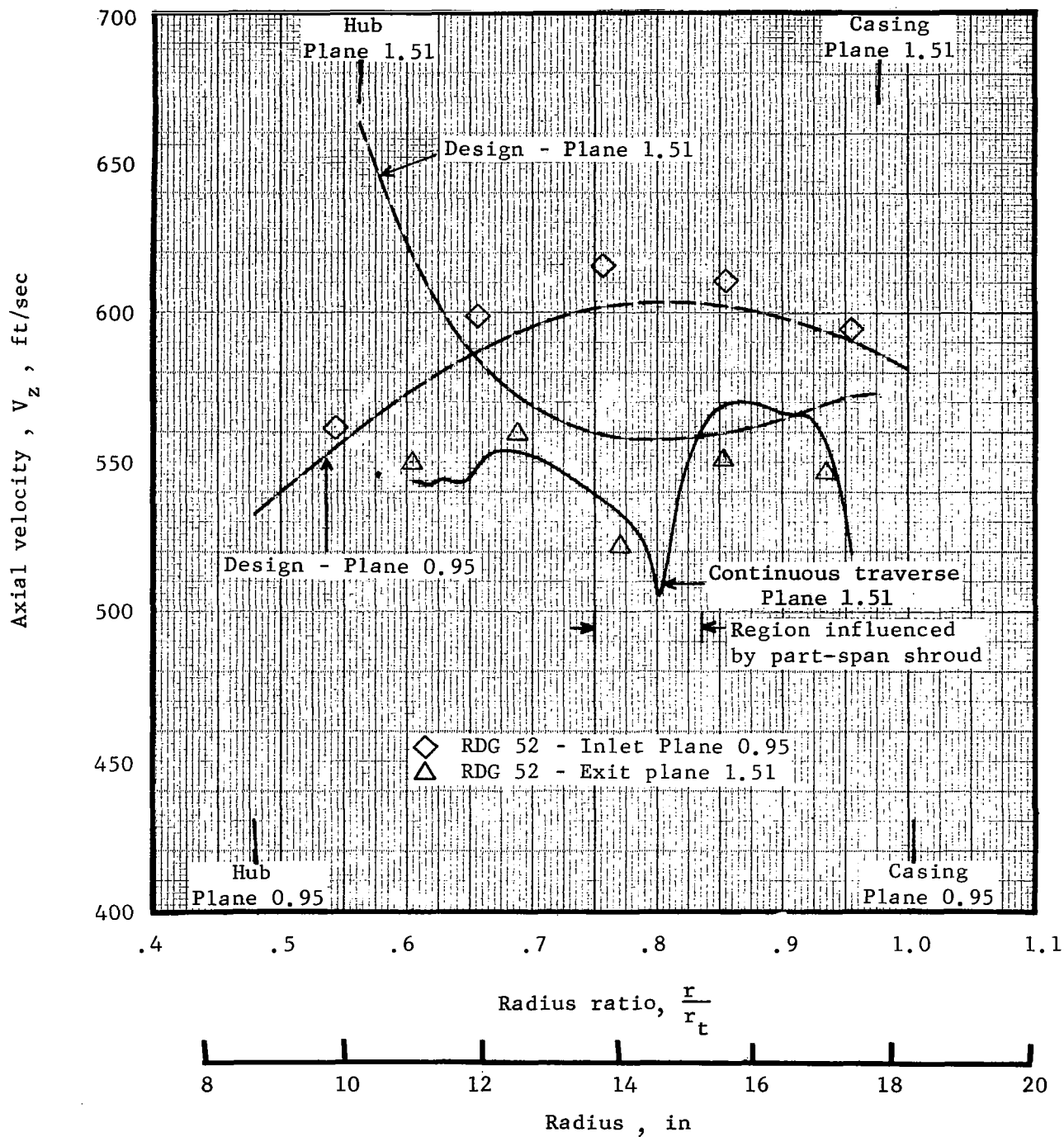
Figure 25. – Radial distributions of inlet and discharge axial velocity for Rotor 1B at design speed.

Figure 26. – Radial distributions of inlet and discharge relative Mach
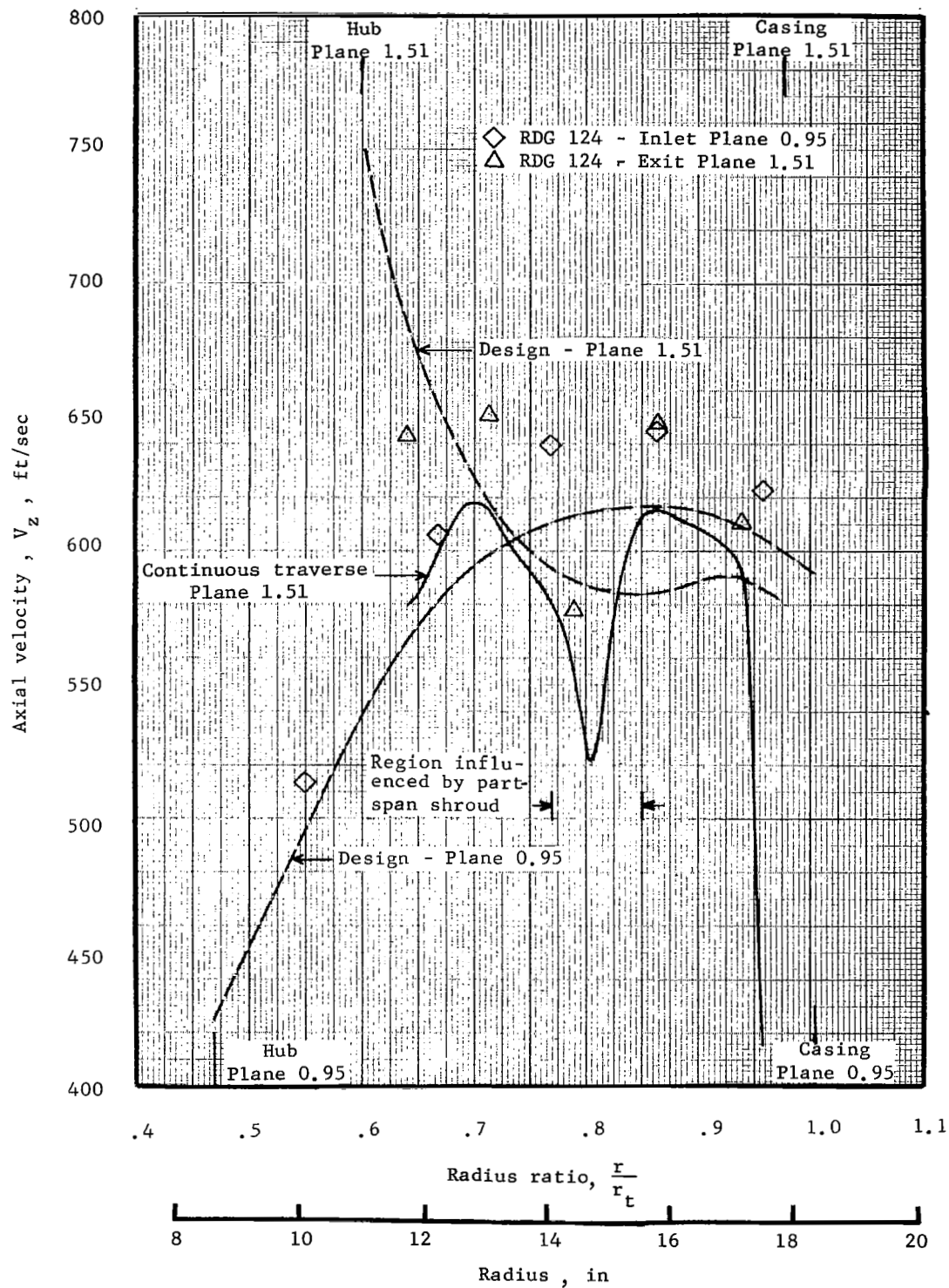number for Rotor 2B at design speed.

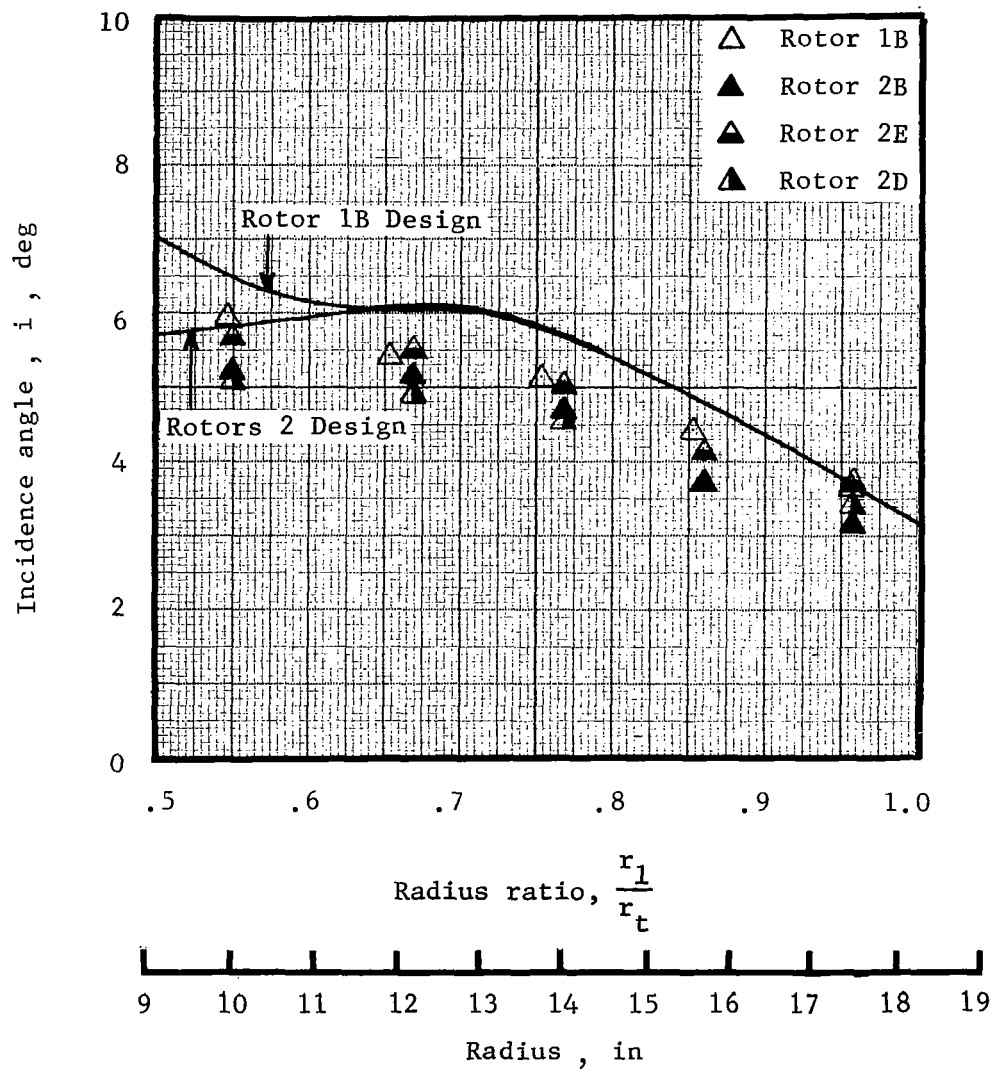Figure 27. - Radial distributions of inlet and discharge axial velocity for Rotor 2B at design speed.

Figure 28. - Radial distributions of measured and design
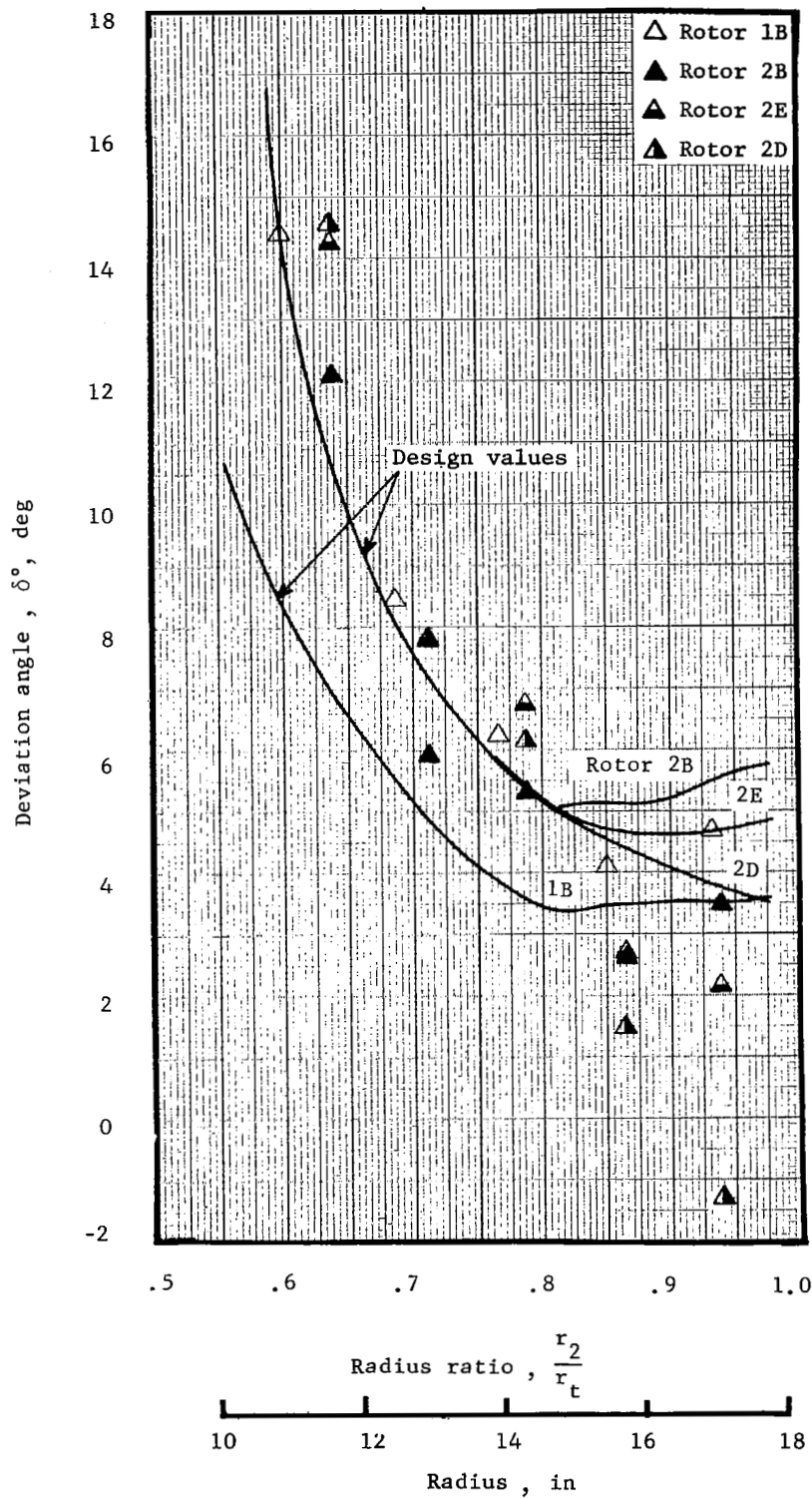incidence angle at design speed.

Figure 29. - Radial distributions of measured and design deviation angle at design speed.